Feasibility of elemental tissue decomposition using activation PET after proton irradiation of head and neck squamous cell carcinomas

Hanneke Pouw

MASTER THESIS TECHINCAL MEDICINE
MEDICAL IMAGING AND INTERVENTIONS

April 2020

UNIVERSITY OF TWENTE.

LUMC Leids Universitair Medisch Centrum

HollandPTC Protonen Therapie Centrum

Feasibility of elemental tissue decomposition using activation PET after proton irradiation of head and neck squamous cell carcinomas

Master thesis Technical Medicine

Author: J.E.E. Pouw (Hanneke)

University of Twente – Technical Medicine, Medical Imaging and Interventions
Leiden University Medical Centre (LUMC) - Department of Radiology, Section Nuclear Medicine
Holland Proton Therapy Center (HollandPTC)

Graduation committee

Prof. dr. L.F. de Geus-Oei, MD	LUMC & University of Twente
dr. D. Vriens, MD	LUMC & HollandPTC
dr. F.H.P. van Velden	LUMC
Ir. P. van der Tol	HollandPTC
Prof. dr. ir. C.H. Slump	University of Twente
drs. P.A. van Katwijk	University of Twente
T. Boers, MSc.	University of Twente

Defense: 15 April 2020 – Digital Conference

Cover design by Laura Aletrino

PREFACE

This master thesis is the result of my one-year clinical internship at the Leiden University Medical Center to fulfil the three year master programme Technical Medicine. The thesis encompasses the interdisciplinary research I performed towards clinical feasibility of activation PET elemental tissue decomposition. The experiments and part of the analysis have been performed in the Holland Proton Therapy Centre, located at the campus of the Technical University Delft.

In the first chapters, I describe the relevance of activation PET elemental tissue decomposition technique and the clinical and technical background. The third chapter enlightens the research objectives. In the following part, a model is specified to perform tissue decomposition. This model is subsequently applied to test several clinical parameters. In the last part, the possible applications and limitations of clinical implementation are discussed.

In the Verantwoording, written in Dutch, I reflect on my personal and clinical development in the process to become a Technical Physician.

The last part of this thesis includes the book chapter I wrote in collaboration with Prof. dr. L.F. de Geus-Oei, dr. D. Vriens and dr. F.H.P. van Velden, which will be published medio 2020 in the Springer Nature book "Image-Guided High-Precision Radiotherapy".

Hanneke Pouw - 5 April 2020

TABLE OF CONTENTS

GLOSSARY

Abbreviation	Explanation
(a)PET	(Activation) Positron Emission Tomography
AC0	estimated initial Mean Activity Concentration. Estimated by the model for t=0; end of proton irradiation.
AIC	Akaike Information Criterion
COV	Coefficient Of Variation
CI	Confidence Interval
CT	Computed Tomography
CTV	Clinical Target Volume
FBP	Filtered Back Projection
FDG	Fluoro-2-deoxy-D-Glucose
GTV	Gross Tumour Volume
GyE	Gray-Equivalent dose
HDPE	High-density Poly Ethylene
HNC	Head and Neck Cancer
HNSCC	Head and Neck Squamous Cell Carcinoma
MLE	Maximum Likelihood Estimation
MRI	Magnetic Resonance Imaging
MU	Monitor unit
NLS	Nonlinear Least Squares
NTCP	Normal Tissue Complication Probability
OSEM	Ordered Subsets Expectation Maximisation
PMMA	PolyMethyl MethaAcrylate
PRT	Proton Radiation Therapy
ICRU	International Commission on Radiation Units and measurements
RT	External Beam Radiotherapy
SD	Standard Deviation
SUV	Standardised Uptake Value
TAC	Time-Activity Curve
TMM	Tissue Mimicking Material
VOI	Volume Of Interest

ABSTRACT

Introduction: Activation positron emission tomography (aPET), i.e. measuring the generated positron emitters after proton beam irradiation, might be a measure for the relative amount of oxygen in irradiated head and neck squamous cell carcinomas. To identify whether offline aPET, i.e. when the PET is not positioned in the treatment gantry, is feasible in clinical practice, four parameters are investigated. 1) The maximal time delay between end of proton irradiation and start PET-acquisition. 2) The minimal amount of dose delivered. 3) The minimal irradiated target volume. 4) The minimal difference in element composition between the irradiated tissues that can be discerned. The limits of these parameters indicate the threshold for enough signal for elemental tissue decomposition.

Methods: To define the limits for clinical feasibility, a method with nonlinear least squares (NLS) estimation is specified to estimate the initial mean activity concentration (AC0) for the generated radionuclides ^{11}C, ^{15}O and ^{13}N. The model is selected based on the correct prediction of the presence of the radionuclides, the lowest Akaike information criterion (AIC) for comparable models and the lowest standard deviation for the parameter estimates. With these criteria, the PET-data reconstruction method, the number of estimated parameters, the frame duration and the volume of interest (VOI)-location and VOI-size are defined. Subsequently, experimental data of five plastic, of which three tissue mimicking, irradiated phantoms are analysed for the four described parameters. The phantoms are irradiated with a 70 – 200 MeV pencil beam scanning proton beam. The defined target volumes, based on HNSCC proton beam treatment plans are 16 mL, 34 mL and 298 mL. The 34 mL target volume is irradiated with 0.5 GyE, 2 GyE and 10 GyE.

Results: NLS model fitting with the three radionuclides in time frames of 60 seconds is selected based on the defined criteria. The ^{15}O:^{11}C-ratio is a more stable parameter for tissue decomposition analysis than the separate AC0s. To obtain a clinical dose (2GyE) ^{15}O:^{11}C-ratio standard deviation of less than 0.1, VOIs of at least 14 mL are required in target volumes of at least 16mL. Moreover, a maximal time delay of 6 minutes is allowed. Within the defined assumptions, the model seems able to differentiate tissue mimicking adipose tissue from muscle mimicking tissue.

Discussion: By the absence of a ground truth, tissues can only be compared inter treatment plan. The minimum time delay in offline PET makes application of aPET impossible in current treatment delivery of around 10 minutes, especially considered the presence of biological wash-out in living tissue. Since all investigated parameters are related to each other, optimising them independently will improve aPET quality.

Conclusion: aPET is under current clinical circumstances not feasible for determination of the relative oxygen amount in tissue. Upcoming proton therapy techniques, such as in-beam detection, hypofractionation and FLASH-irradiation may lead to higher aPET quality, which may overcome the time delay, creating options for future aPET application.

Keywords: *Activation PET, Head and neck squamous cell carcinoma, Proton radiation therapy, Elemental tissue decomposition, Time-activity curves, Treatment plan*

CHAPTER 1

General introduction

In 2018, almost 900,000 new cases of head and neck cancer are estimated worldwide by the World Health Organisation, with the highest incidence in lip- and oral cavity cancer. In the Netherlands, over 3000 new cases are estimated. [3] Most of the head and neck cancers are squamous cell carcinomas (HNSCC), originating from the squamous cells in the mucosal tissue between the anatomical structures of the head and neck region, which include the nasopharynx, nasal cavity, oropharynx, oral cavity, hypopharynx and larynx. [4] Approximately 80% of the HNSCC cases are associated with tobacco and alcohol exposure. Tobacco use mainly increases the risk of laryngeal cancer, while alcohol is especially correlated with hypopharyngeal- and oral cavity cancer [5]. The risk on developing HNSCC is multiplicative when alcohol and tobacco use is combined, presumably caused by the increased sensitivity of the cells to DNA–damage from the tobacco use by the aldehyde, metabolised from ethanol. Infection with human papillomavirus, especially subtype 16, has a strong correlation with the development of different types of HNSCC, including oropharynx, tonsil and base of tongue. Infection with the Epstein-Barr virus is strongly correlated with the development of nasopharyngeal squamous cell carcinoma. [6]

External beam radiotherapy (RT) is indicated as definitive treatment in early stage HNSCC. In patients with locally advanced disease, RT, optionally combined with chemotherapy, is recommended. [7] RT is applied postoperatively when a high risk of locoregional recurrence exists, optionally combined with concurrent chemotherapy or immunotherapy. [8, 9] Locoregional irradiation in metastatic HNSCC is associated with benefit on overall survival. Definitive RT in head and neck oncologic patients showed to provide good long-term outcomes, especially in the prevention of locoregional recurrence in high risk patients. [10]

RT, however, is associated with high symptom burden and increased risk for long term complications. Up to 48% of the head and neck cancer (HNC) survivors is limited in performing their work or is not able to work at all following treatment. [11] Complications like pain, acute mucositis, dysfunction of the salivary glands, dysphagia and impaired ability to sense taste might have an onset up to two weeks after end of irradiation. Many of these symptoms disappear within six months after irradiation. Long term complications are among others xerostomia, permanent dysphagia, hypothyroidism, osteoradionecrosis, fibrosis and soft tissue necrosis. [12, 13] High-dose cervical radiation, necessary to prevent locoregional recurrence, may result in vascular diseases in the carotid arteries. The inflammatory response after radiation accelerates atherosclerosis, resulting in increased risk on neurological events.

Additionally, since radiation causes deoxyribonucleic acid damage in the irradiated tissue, treatment with RT increases risk of secondary tumours. Of the first 2500 patients, irradiated at the Netherlands Cancer Institute for HNC, 0.70 percent developed a malignancy within a previously irradiated area within a mean time span of 36.5 years. The cumulative radiation dose was between 10 GyE and 70 Gy. This dose is

considered to be lower than currently delivered cumulative dose, since formerly benign pathologies used to be low dose irradiated. The developed tumours were soft tissue sarcomas, squamous cell carcinomas and salivary gland tumours. [14]

Application of proton radiation therapy (PRT) might improve overall survival and disease-free survival in comparison with intensity-modulated radiation therapy, the photon therapy state of the art. [15] Thanks to the physical properties of protons, a low entrance dose, a rapid falloff dose near the end of the proton range and an uniform lateral dose profile, with a sharp lateral penumbral width can be achieved. All leading to a better conformation of the dose to the target volume, reducing dose in healthy tissue. [16, 17] This effect is visualised in the depth-dose graph in Figure 1. A monoenergetic proton beam shows a small Bragg-peak, the region of maximal dose delivery. To cover the whole target volume in beam direction, multiple proton beam energies are combined, resulting in a so called spread-out Bragg peak. Moreover, Wang *et al.* showed that PRT seems to have larger potential of destructively damaging HNSCC cells than photon radiation therapy. [18] In general, the relative biological effectiveness of protons is with 1.1 higher than of photons, 1.0. The treatment plans are based on this relative biological effective dose, which is expressed as Gray-equivalent dose (GyE). The physical delivered dose (Gy) will therefore be a factor 1.1 lower than the planned doses. Although no definitive results on the effectiveness of PRT have been shown until now, results seem promising and the number of institutions applying PRT is constantly increasing, as are the indications for treatment. [9]

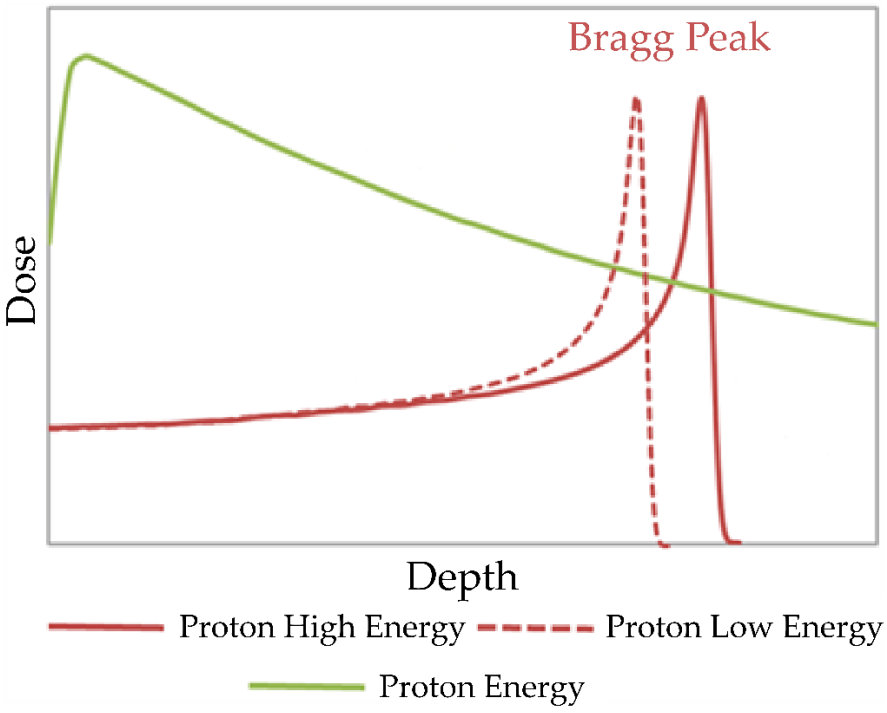

Figure 1; Depth-dose graph for the comparison between photon and proton dose delivery over depth. Retrieved from [19].

Since the costs of proton therapy are considerably higher than for photon therapy, substantial expected improvement in patient outcome is necessary to justify the application of PRT in the long term. The publication of an independent proton therapy rapport by the Dutch Ministry of Health in 2009, meant the beginning of proton therapy facilities in the Netherlands. [20] The 2011 health insurance board rapport stated HNC as a model-based indication. [21] Since then, PRT is stated as the treatment of choice in HNC, when the risk of post treatment side-effects is considerably lower than for photon radiation therapy. This risk is estimated by normal tissue complication probability (NTCP) models, assessing the occurrence of three debilitating long-term side effects. These common side effects, after irradiation in the head and neck region are moderate to severe xerostomia, dysphagia and nasogastric intubation. The indication threshold for proton therapy versus photon therapy is a NTCP difference for long term xerostomia, dysphagia, xerostomia and dysphagia combined and nasogastric intubation of 10%, 10%, 15% and 5%, respectively, see Figure 2. At least one threshold should be reached for proton therapy indication. Symptoms persistent six months after completion of the PRT are considered long term side effects. The criteria for PRT indication can be found in the Dutch guidelines, set up by the National Platform for Proton Therapy in the Netherlands. [12] An example of a treatment plan comparison between photon therapy and proton therapy is visualised in Figure 2. In this example, the threshold NTCP difference for proton therapy versus photon therapy of -10% for dysphagia is achieved, which makes this case indicated for proton therapy treatment.

Since there is no exit-dose in PRT, measuring the delivered dose in the irradiated tissue is difficult. One way to find the location where dose was delivered is by activation positron emission tomography (aPET). During PRT and heavy-ion beam irradiation, most commonly in the form of ^{11}C, radioactivity is generated in the form of positron emitting radionuclides. The resulting positrons can be detected in a PET-scanner, either in-beam, during proton irradiation, in-room, by a PET-scanner located in the treatment room or off-line, with an external PET-scanner. The amount of time delay increases for the distance between the proton gantry and the PET-detectors.

By recalculating the position of the generated radionuclides from the irradiated tissue, in a similar way the activity is reconstructed in a clinical PET-study with injected radiopharmaceuticals, a PET-image of the produced radioactivity *in vivo* can be created. This image with simulated predictions of the produced activity, based on the physical properties of the proton beam, can be used to verify the delivered dose and range of the proton beam, compared to the treatment plan. The dose deposition can be modelled with good agreement, although dependent on the input data, i.e., cross sections, based on computational extensive Monte-Carlo simulation, for example with toolkits like FLUKA, FLAIR, GATE and GEANT (4). Less computational intensive prediction algorithms are also developed, for example the analytical one-dimensional filtering approach of Parodi et al. [22] and the TPS_{PET} by Frey et al. [23]. This TSP_{PET} prediction algorithm is further developed in the software PET-RV. [24]

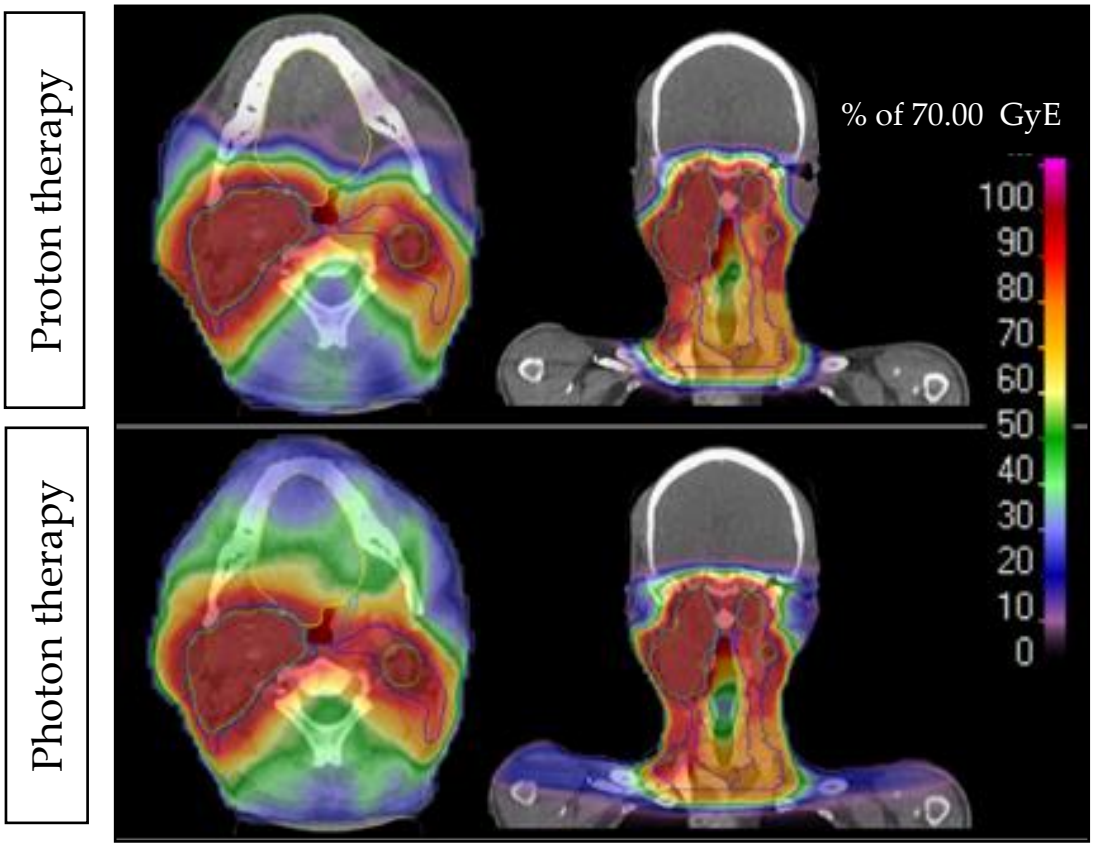

	Proton therapy	Photon therapy		
	Mean Dose (GyE)	Mean Dose (GyE)		
Contralateral glandula parotis	18.8	25.7		
Oral Cavity	16.0	37.0		
Superior PCM	60.9	65.3		
Inferior PCM	28.8	38.0		
m. Cricopharyngeus	24.0	27.8		
	NTCP (%)	NTCP (%)	ΔNTCP (%) (proton - photon)	ΔNTCP (%) threshold
Xerostomia	37.1	45.7	-8.6	-10
Dysphagia	18.9	30.0	-11.1	-10
∑ xersostomia and dysphagia			-19.7	-15
Nasogastric intubation	6.8	10.1	-3.3	-5

Figure 2; Treatment planning comparison between proton radiotherapy (upper image) and photon therapy (lower) image for a patient with a nasopharynx carcinoma (T2N2M0). Both plans contain a CTV7000, 70GyE, including the nasopharynx and the pathological lymphnodes (green contour) and a CTV5425, 54.25 GyE, including the elective volume, i.e. nonpathological, but high risk for metastasis lymph nodes (blue contour). The total dose is delivered in 35 fractions. Upper part visualises the target volumes, the organs at risk and the expected dose delivery. Lower part tabulates the estimated dose delivered per organ at risk and the NTCP for xerostomia, dysphagia and nasogastric intubation. In this case, the NTCP for proton therapy is lower for all three side–effects, but the threshold value is only reached for dysphagia. Image and data retrieved from Vriens et Van Vulpen. [2] CTV: clinical target volume. GyE: Gray-Equivalent. NTCP: normal tissue complication probability. PCM: pharyngeal constrictor muscle. m.: muscle. ∑: summation

aPET can also be applied for the purpose of elemental tissue decomposition. By analysing sub volumes of the irradiated tissue, information can be perceived about the tumour and its surrounding. An important predictor for the effect of PRT is the vascularisation of the tumour. Gray et al. showed in 1953 the increased radiosensitivity towards hypoxic regions. [25] By determining the relative amount of oxygen in the tumorous tissue, for example with aPET, treatment might be intensified for better tumour control. Treatment intensification can, within treatment planning, be realised in dose escalation of the tissues low in oxygen regions. This process, called dose painting, is further explained in **APPENDIX B.**

.

Comparison of multiple aPET tissue composition analyses during radiation treatment might indicate the effect of irradiation on the tissue, e.g. the development of necrotic tissue or the increase of oedematous tissue. In HNC patients, which radiation treatment generally encompasses 35 fractions, early information about the tissue response on treatment might be obtained.

Although multiple studies analyse the proton induced activation effect for dose and range verification, only three published studies were found for the purpose of elemental tissue decomposition purpose. [26-28]. These studies showed promising results for in-beam and in-room imaging. This research focusses on the feasibility of off line aPET elemental tissue decomposition, with multi energetic treatment plans, as used in clinical practice. Aim is to define the relative amount of oxygen (^{16}O) in irradiated tissue in HNSCC patients.

CHAPTER 2

Theoretical background

2.1 Interaction of protons with tissue

Protons lose energy by collision via (inelastic) Coulomb interaction with electrons, repulsive and thus elastic Coulomb interactions with the nuclei and non-elastic nuclear reactions. Energy loss, via bremsstrahlung also occurs, although this effect is neglectable in proton therapy. Non-elastic nuclear reactions cause particle ejection from the nucleus. These particles can be protons, neutrons, or a combination of these in the form of cations. Emission of gamma rays will also occur mainly due to excitation of the nucleus, which once returning to its resting state emits a characteristic prompt gamma spectrum.

To simulate dose delivery in the target volume in proton beam irradiation treatment planning, the proton range, dependent on these interactions, is modelled. The proton range is the distance the proton beam travels through the tissue, delivering dose. The range depends on the initial, kinetic energy of the proton and the specific characteristics of the material. The stopping power, i.e., how much energy a charged particle loses per unit of distance, $-\frac{dE}{dx}$, is a measure to express this range. The Bethe-Bloch equation, found frequently in literature and outlined for protons in radiotherapeutic energy range expresses this stopping power as follows: [29]

$$-\frac{dE}{dx} = \frac{(4\,\pi\rho_e z^2)}{m_e c^2 \beta^2}\left(\frac{e^2}{4\pi\epsilon_o}\right)^2\left(\ln\left(\frac{2m_e c^2\beta^2}{I(1-\beta^2)}\right)-\beta^2\right). \quad (1)$$

The stopping power of the particle depends on the material characteristics of the irradiated tissue, where ρ_e represents the target electron density, z the charge of the projectile, m_e and e the electron mass and charge, respectively and I the mean excitation energy of the absorbing material. β is defined as $\frac{v}{c}$, with v the kinetic speed of the proton and c the maximum speed of light (in vacuum), $2.998 \cdot 10^8$ m/s.

The absolute delivered absorbed dose by a proton beam can be measured by monitor chambers. The corresponding output measure, the monitor unit (MU), corresponds to a fixed amount of dose at a reference point in water. The number of MUs is defined in the treatment plan per fraction and per spot. The dose rate is provided by the number of MUs per time unit. [30]

2.2 Generation of positron emitters

All described nuclear interactions result in a certain amount of dose in the target material, i.e. the human body in PRT. The ejected secondary particles, due to inelastic nuclear reaction, after the projectile proton has entered the nucleus, deliver additional dose. The removal of particles out of the nucleus of the incident atom results into instable radionuclides. Removal of one or more neutrons from the nucleus may result in positron

emitters (e.g. ${}^{12}_{6}C + {}^{1}_{1}p^{+} \rightarrow {}^{11}_{6}C + {}^{1}_{1}p^{+} + {}^{1}_{0}n$). This instable positron emitter, with too many protons in its nucleus relative to the number of neutrons, decays while forming a positron (anti-electron), whereafter it reaches a new stable form (net change: a proton less, a neutron richer). E.g. ${}^{11}_{6}C \rightarrow {}^{11}_{5}B + {}^{0}_{1}\beta^{+} + \nu_e$). The emitted positron annihilates after a short travel with an electron, resulting in two photons (${}^{0}_{1}\beta^{+} + {}^{0}_{-1}\beta^{-} \rightarrow 2\gamma_{511keV}$). Due to the conservation of energy and momentum both photons will have an energy of around 511 keV and are emitted in near anti parallel direction. These gamma rays can be detected in a PET-scanner. [16] A more extensive explanation of this process is provided in **APPENDIX B.**

The total number (N) of positron emitter Y generated by the proton interaction with nucleus X with the energy dependent nuclear reaction cross section $\sigma_{X\rightarrow Y}(E)$ and proton fluence $\Phi(E)$, detected in a volume ΔV is expressed by Parodi et al. [31] by:

$$N_Y = \int \frac{d\Phi(E)}{dE} \frac{f_X \rho N_A}{A_X} \sigma_{X\rightarrow Y}(E) \Delta V dE. \quad (2)$$

The incident material specific properties are the fraction by weight (f_X), the atomic weight (A_X) and the density (ρ) of the material. N_A is the Avogadro constant.

The resulting activity (A) in disintegrations per second (Bq) depends on the radionuclide specific decay constant (λ), (see Table 3) according

$$A = -\frac{dN}{dt} = \lambda N \quad (3)$$

2.3 Tissue elemental composition

The number of nuclear interactions that occur, representing the produced radioactivity, depends on the cross section per element, and thus of the number of atoms, present in the tissue. In human tissues, oxygen, carbon and hydrogen are in percentage weight the largest contributors in element composition. Skeletal tissues are an exception to this statement, with a high amount of calcium and phosphor, see Table 1. [32, 33] In this table, the density, the electron density and the contribution per element in weight percentage is expressed. The elemental composition of squamous cell carcinomas, developed from the mucosal tissue, can be based on the element composition of soft tissue. Multiple studies find different relative contributions for soft tissue. In this thesis the recommended values by the International Commission on Radiation Units and Measurements (ICRU) are used as reference, see Table 1. [33]

The amount of activation depends on the number of elements in the irradiated tissue. To approach this produced activity, the relative weight of the elements should be kept in mind. The true values depend on the specific tissue type, the microenvironmental status, e.g. the vascularity, the amount of oedema, necrosis and calcification, and should be defined patient and time point specific, with for example spectral CT or DECT. [34] The scarce elements fluctuate relatively much in different regions, as investigated in different samples of oral squamous cell carcinoma by Pawlikowski *et al.* and will therefore not be taken into consideration in this thesis. [35] Interesting to mention is the

discovery of Pawlikowski *et al.* that the levels of these scarce elements, the biominerals, e.g. Ca, P, K, S, were elevated in cancerous tissue, compared to healthy tissue, indicating that they either play a role in oncogenesis, or are generated as side products due to the cancerous activity of the tissue. [35, 36] ^{1}H, ^{12}C, ^{16}O, and ^{14}N are considered the largest contributing elements in human tissue.

Table 1; Elemental composition of different human tissues, main contributing elements mentioned; W_i: the mass percentage of the tissue. ϱ: density. ϱ_e: electron density. [32, 33, 36]

Tissue	**ϱ (g cm^{-3})**	**ϱ_e**	**^{1}H**	**^{12}C**	**^{16}O**	**^{14}N**	**^{31}P**	**^{40}Ca**
			W_i (%)					
Adipose	0.95	0.951	11.4	59.8	27.8	0.7	-	-
Blood	1.06	1.050	10.2	11.0	74.5	3.3	0.1	-
Muscle	1.05	1.040	10.2	14.3	71.0	3.4	0.2	-
Cortical bone	1.92	1.781	3.4	15.5	43.5	4.2	10.3	22.5
Soft Tissue	1.06		10.2	14.3	70.8	3.4	0.0	
Water	1.00	1.000	11.2	-	88.8	-	-	-

2.4 Cross sections

Table 2 presents an overview of the most important nuclear interactions by proton irradiation of ^{12}C, ^{16}O and ^{14}N. The nuclear reactions that contribute substantially to the amount of activation produced are expressed in bold. Exclusion criteria were not enough experimental data, i.e. less than five data points within clinical beam energy range, or too short half-life values to be measured with offline PET. The threshold value for inclusion of the nuclear reaction is a half-live value of 22.5 seconds, corresponding with 8 half-life values in 3 minutes. This is based on the time delay in off-line aPET and the amount of signal needed for the creation of a time-activity curve (TAC). All threshold energies for the nuclear reaction that can occur, as described in Table 2, are below the minimal incident energy of the clinical proton beam of 70 MeV. Therefore, all nuclear reactions will occur. Only the nuclear reactions for the isotope per element which is most often naturally occurring, is taken into consideration. Based on these criteria, it can be stated that the only radionuclides expected to be evidently detectable after proton irradiating human tissue are ^{11}C, ^{15}O and ^{13}N.

The amount of generated positrons depends on the energy dependent cross sections. These cross section values, expressed in barns (b), which need to be determined experimentally were retrieved from the EXFOR database of the Hokkaido University Nuclear Reaction Data Centre and visualised in Figure 3. [1] These data are in agreement with the recent cross sectional data from Horst *et al.* [37] The experimental data, however, show a large variability, which causes a large uncertainty in further calculations.

Table 2; Generated positron emitters by proton irradiating tissue. Thresholds of the nuclear reactions are approximations. $T_{1/2}$: half-life value. p: proton. n: neutron. γ photon.

Target nucleus	Main nuclear reaction	Generated positron emitter	$T_{1/2}$ of positron emitter	Threshold (MeV)	Criterium for exclusion in our analysis
^{12}C					
	(p, pn)	^{11}C	**20.3 min**	**15**	**Included**
	(p, p2n)	^{10}C	19.2 sec	20	Too short $T_{1/2}$
^{16}O					
	(p, pn)	**^{15}O**	**122 sec**	**15**	**Included**
	(p, p2n)	^{14}O	70.6 sec	-	Not enough experimental data available
	(p, 2p2n)	**^{13}N**	**9.97 min**	**6**	**Included**
	(p, 3p3n)	**^{11}C**	**20.3 min**	**7**	**Included**
	(p, 3p4n)	^{10}C	19.2 sec	-	Too short $T_{1/2}$ Not enough experimental data available
^{14}N					
	(p, γ)	^{15}O	122 sec	-	Not enough experimental data available
	(p, n)	^{14}O	70.6 sec	6.5	Not enough experimental data available
	(p, pn)	**^{13}N**	**9.97 min**	**10**	**Included**
	(p, 2p2n)	**^{11}C**	**20.3 min**	**5**	**Included**
	(p, 2p3n)	^{10}C	19.2 sec	-	Too short $T_{1/2}$ Not enough experimental data available

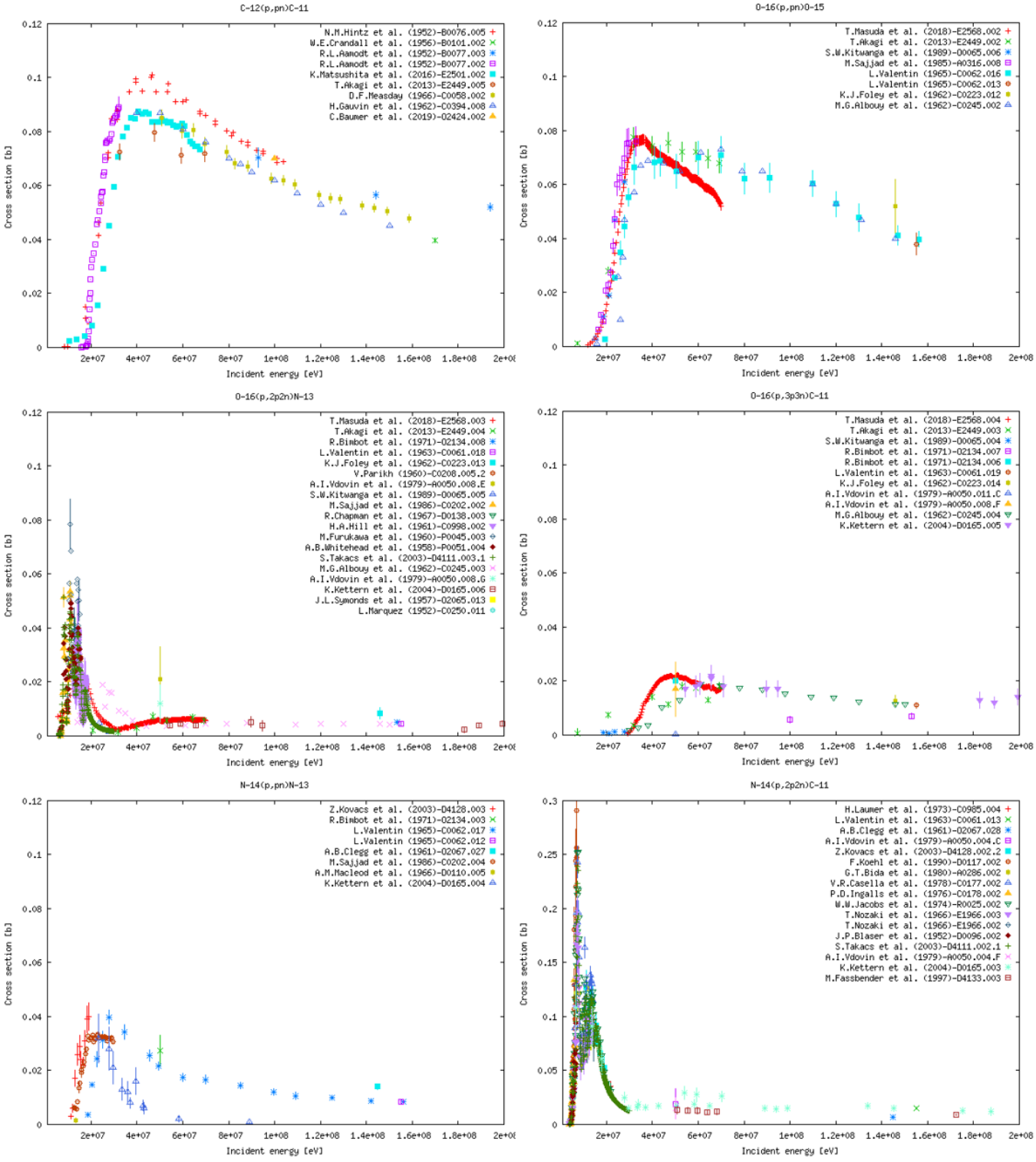

Figure 3; Cross sections for the nuclear reactions considered in this thesis, between 1 MeV and 200 MeV incident proton beam energy. Notice the rescaled y-axis for the $^{14}N(p2p2n)^{11}C$ reaction (right under). Data retrieved from the Hokkaido University Nuclear Reaction Data Centre, EXFOR. Sources of the data points are mentioned per graph. [1]

The cross sections of the nuclear reactions, considered relevant are visualised in Figure 3. The graphs are plotted between 1 MeV and 200 MeV kinetic proton energy, which corresponds with the beam energy applied in our experiments. All cross section show a similar trend. A cross section peak is visible between 5 and 45 MeV incident energy. At higher kinetic energies, the cross sections are steadily decreasing. In therapeutic energy range (70-250 MeV), lower proton energy, results in larger cross sections and therefore more nuclear interactions and generated activity.

Most of the protons pass through the tissue without causing nuclear reactions as atoms are largely empty space and there is recoiling energy from the positive nucleus to the approaching proton. By passing through the tissue, they, however, lose energy by ionisations. When their energy has decreased under the threshold value for nuclear reactions, the particle will move further, delivering dose by Compton scattering, without producing any activation. By comparing the dose and the activation profile of the beam, therefore, it is expected that the dose profile will reach further in depth than the activation signal. This effect is visualised by Horst *et al.* [37], with results of España *et al.* [38] in Figure 4.

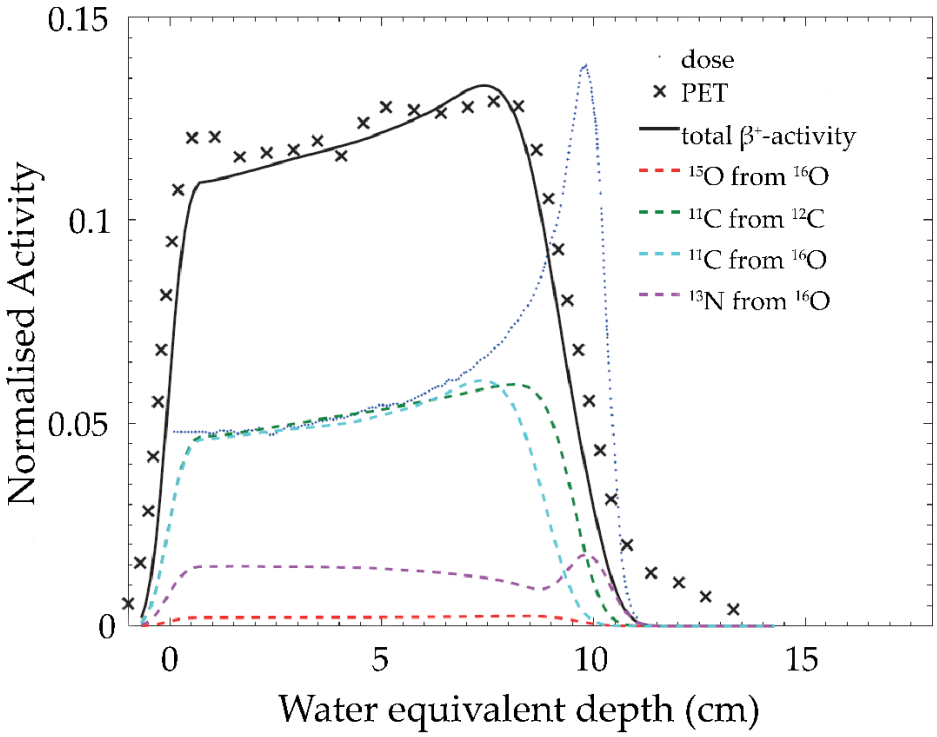

Figure 4; Dose profile (blue) and total activation signal, from positron emission (black) in 15 minute delay, 30 minute PET-acquisition after irradiation with a 116 MeV proton beam. Graph and activity from [37]. Activation profile from: [38]

2.5 Isotope-related factors influencing PET-acquisition signal

The required PET–acquisition data represent only the amount of radionuclides, detected by the scanner. To determine the amount of positron emitters, generated in the tissue, correction should take place for the decay and the branching factor of the radionuclides. The positron range is a quality degrading factor, also dependent per isotope.

2.5.1 Decay

To determine the initial radio activity, directly after proton irradiation, the decay of the radionuclides needs to be corrected for. In clinical software, decay correction is implemented in the reconstruction process. In this research, the decay correction of ^{22}Na is applied, since this radionuclide is the longest living isotope used in clinical setting. The decay constants, the isotope-specific probability of decay per unit time, for the relevant radionuclides in this research is expressed in Table 3. The half-life value, $t_{1/2}$ is correlated with the decay constant, λ according to

$$t_{\frac{1}{2}} = \frac{\ln(2)}{\lambda} \quad (4)$$

2.5.2 Branching fraction

The positron emitter radionuclides decay for a small fraction by different decay modes than positron emission. This positron or branching fraction is independent of the target material, but differs per radionuclide, see Table 3. The branching fraction is therefore a constant between the number of generated 511 keV photons and the amount of decayed radionuclide. To determine the total amount of radionuclides in the tissue generated by our proton irradiation, the number of PET-detections need to be corrected for with the branching fraction. Since every radionuclide has its own branching fraction, this branching fraction is corrected for the decoupling model of the TAC.

2.5.3 Positron range

After the positron producing nuclear reaction, this positron moves several millimetres through the tissue before annihilation takes place. With PET-reconstruction, the position of the annihilation is determined. Since the location of the positron production is not known, deterioration of the resolution occurs. The positron range, defined as this travelling distance between the production and the annihilation, depends on the positron and the material. A larger positron range leads to more blurring, due to a higher uncertainty of the nuclear interaction location. The mean and maximum distances in water for the relevant radionuclides in this thesis and for ^{18}F for comparison, are outlined in Table 3.

Table 3; Positron range and branching fraction for the relevant radionuclides in this thesis. Positron ranges are derived of: [39, 40]. Branching fraction and decay constant of: [41] and eq. (2).

Radionuclide	**Positron range in water (mm)**		**Branching fraction, γ**	**Decay constant, λ (s^{-1})**
	Mean	*Max*		
^{22}Na	0.53	2.28	0.9038	8.4e-09
^{11}C	4.2	1.2	0.9977	5.7e-04
^{15}O	3.0	8.4	0.9990	5.7e-03
^{13}N	1.8	5.5	0.9980	1.2e-03
^{18}F	0.6	2.4	0.9673	1.1e-04

CHAPTER 3

Research objectives

Aim of this pilot-research is to investigate to which extend aPET for tissue decomposition is feasible in clinical application in a proton therapy facility with the following three characteristics:

1) A clinical commissioned pencil beam scanning proton beam in a 360 degrees rotating gantry. Its proton beam energy range is between 70 MeV and 245 MeV and its sigma beam spot size around 6 mm at 70 MeV.
2) Availability of a PET-scanner which is not located in the proton beam treatment room, but is within 1-5 minutes walking distance (offline PET).
3) Availability of a high sensitivity (up to 30 cps/kBq) clinical PET-scanner, with a spatial resolution of around 4.2 mm in axial direction and around 3.4 in transversal direction.

To investigate whether aPET is feasible in these conditions, several parameters are analysed as described in section Clinical parameters. For performing tissue decomposition, a model and its parameters need to be selected to estimate the produced amount of positron emitters directly after proton irradiation, based on the PET-acquisition data. This estimated initial mean activity concentration is referred to as AC0. AC0 is defined as the sum of the estimated initial activity per radionuclide in a certain volume (VOI), divided by the volume of that VOI. This estimated initial mean activity concentrations is defined at t=0, end of proton irradiation. By dividing AC0 of ^{15}O by the corresponding AC0 of ^{11}C, the ^{15}O:^{11}C-ratio is perceived. Since ^{15}O is only generated in a substantial amount by proton irradiation of ^{16}O, can the ^{15}O AC0 be considered as a relative amount of ^{16}O in the tissue.

The first part of this thesis is focused on the selection of this model and its parameters to perform aPET tissue decomposition with the defined conditions. The reconstruction method of the PET-image can have large influence on the quantitative results. Therefore, first a comparison is made between the two reconstruction methods filtered backprojection (FBP) and ordered-subsets expectation-maximisation (OSEM). For accurate decoupling of the TAC, the optimum in the PET-acquisition frame duration is searched for. Long acquisition frame durations result in more coincidences and thus a better signal to noise ratio. Long time frames, however, can limit the accurate estimation of radionuclides with a short half-life. The performance of the model is also influenced by the number of parameters the model estimates. The estimation of two radionuclides, ^{11}C and ^{15}O, is required for the analysis. Addition of an additional nuclide is expected to improve the parameter estimation. The output of the nonlinear regression is compared with activity concentrations mentioned in literature.

To decrease the influence of variability within the measurements, multiple outcomes are compared. Since repeating measurements is not possible, due to cost, time and exposure constraints, data of multiple VOIs at different positions in the phantom in the same experiment are compared. Therefore, the spatial distribution of the activity

concentration over the phantom is investigated. The number of VOIs that can be analysed, depend on the minimum size of the VOI required for accurate decomposition and is investigated in the last part of

In the second part of the thesis, feasibility of aPET is tested with the specified model and criteria.

3.1 Tissue decoupling method

In this section, the conditions for tissue decoupling are defined. The following parameters are investigated:

a) Reconstruction method
b) Model selection
    a. Frame duration
    b. Number of estimated radionuclides
c) Generated activity
d) Spatial distribution
e) VOI - size

a) Reconstruction method

Reconstruction of the PET-acquisition data is performed with two methods, FBP or iterative reconstruction using OSEM. To find out which reconstruction method is best for further analysis, both resulting images are compared. In FBP, the lines of response are back projected to calculate the position of the annihilation. This back projection might lead to streak artefacts, especially in case of low count statistics. During iterative reconstruction, projections, based on an estimated image, are compared with the projections, based on the acquisition data. The estimated image is subsequently updated, where after the estimated projection is compared with the acquisition data projection again. With the OSEM-algorithm, only a subset of the projection angles is used for calculating the projection data. A more extensive explanation of the reconstruction methods is provided in APPENDIX B.

In general, FBP reconstructed images contain streak artefacts and a large amount of noise, which makes detection of small lesions difficult. This effect is, however, dependent of the delivered dose. OSEM reconstruction generates images of higher image quality, with less or no streak artefacts and are therefore most often applied in clinical setting. In aPET-measurements, the detected amount of proton induced activity is around a factor five lower compared to clinical setting. Irradiation of a volume with 2 GyE is expected to lead to a mean activity concentration of 1 kBq/mL, while ^{18}F-Fluoro-2-deoxy-D-Glucose (FDG) administration, the most common PET-radiopharmaceutical, provides a mean activity concentration of approximately 5 kBq/mL, considering a standardized uptake value of 3. [42] Since in aPET setting, compared to clinical setting, a lower signal-to-noise ratio is expected, OSEM reconstruction is expected to provide higher quality images than FBP reconstruction.

The risk of OSEM application is the unpredictability of the nonlinear method, especially in case of these low number of counts, which may result in artefacts. One artefact, influencing quantitative analysis, as in this thesis, is the occurring of positive bias by non-negativity constraints. [43] When non-negativity constraints occur during OSEM reconstruction, the mean AC0 will increase by shorter frame durations, when less signal is available. When these non-negativity constraints influence the measured data, OSEM is considered not suitable for aPET tissue decomposition and FBP is used as reconstruction method.

b) Model selection

To define AC0 for the separate radionuclides, a model is defined. After definition of this model, the most optimal time frame duration, number of radionuclides and reconstruction duration is defined.

Since the short decaying radionuclides decay faster than the long living ones, an increasing time frame might be optimal for distinguishing radionuclides. Which is also applied by Kraan et al. [28]. Cho et al. [44] and Grogg et al. [45] listed the PET-data in time frames of 60 seconds.

The statistical significant correct estimation of ^{15}O and ^{11}C is required to define the relative amount of oxygen in the tissue. The addition of an additional parameter is expected to increase the goodness of fit. However, the AIC will indicate whether it improves the model.

c) Activity concentration validation

Since the two main nuclear reactions are $^{12}C(p,pn)^{11}C$ and $^{16}O(p,pn)^{15}O$, these two nuclear reactions are used to hypothesise the ^{15}O:^{11}C –ratio in PMMA. The relative number of generated ^{11}C and ^{15}O nuclides, as expressed in eq. (2), is calculated for PMMA proton irradiation. The only variables in this equation that differ between two nuclear reactions in the same experiment are the cross sections, the weight fraction and the atomic mass. For the calculation of the expected ^{15}O:^{11}C -ratio, the multi energy layer treatment plan is simplified by using only the 150 MeV energy layer, which is the mean proton beam energy used in the PMMA experiments. The cross section at this energy for both reactions is 0.046 ± 0.006, see Figure 3. For the resulting number of nuclides is the activity, directly at the end of proton irradiation determined by eq. (3). The ratio of the activity generated by $^{16}O(p,pn)^{15}O$ and $^{12}C(p,pn)^{11}C$ of 4.0 is the hypothesised ^{15}O:^{11}C -ratio of the tissue. The ratio between ^{11}C HDPE and PMMA is calculated in the same way, although supplemented with the different material density. The hypothesised AC0 ^{11}C ratio between HDPE and HDPMMA is 1.2.

In HDPE, Parodi et al. [42] reported a ^{11}C activity concentration of approximately 3 kBq/mL/2.5GyE, which is comparable with previously reported results by Nishio et al. [46] In PMMA, generation of 1 kBq/mL/Gy ^{11}C is stated in both studies. Since the generated amount of the radionuclide ^{15}O is expected four times larger than the amount of ^{11}C, the expected total activity concentration is around 5 kBq/ml/Gy. [42]

In clinical data, the observed activity concentrations show a large variability between tissue types. Parodi et al. mentions an average ^{16}O activity concentration between 60 Bq/mL (brain) and 320 Bq/mL (soft bone) in cranial base and spine irradiation with 1.8 – 2 GyE. [47] No clinical data are available regarding the total amount of

generated activity concentration. These activity concentrations of human muscle, cortical bone and adipose fat are *in vivo* measurements with a time delay of 13–20 minutes. During this delay, biological decay occurs, resulting in an underestimation of the total generated activity concentration. Grogg et al. demonstrated a maximal activity concentration in tissue- and water like gel of maximal 10 kBq/mL for 2 GyE irradiation and in irradiated rat of 15 kBq/mL for 5 GyE. [45] The results of these studies might differ from our experiments minimally, since these studies used a passive scattering beam, while we use a scanning pencil beam technique in our experiments.

The predicted activity concentrations per ml per GyE for the different materials are given in Table 4. For simplicity, in this recalculation, the assumption is made that the beam energies in the treatment plan are not adjusted. In clinical practice the beam energies vary depending of target size and depth in beam direction.

Table 4; Predicted ^{11}C mean initial activity concentrations by proton irradiation of different materials and tissues. Data is based on experimental data and is recalculated per GyE assuming energy beams in clinical range (max 200 MeV). The *in vivo* rat PET-acquisition is in beam measured. The human tissues with 13 – 20 minute time delay after end of proton irradiation. [42, 45-47]

Material	**Predicted Activity concentration (kBq/mL/GyE)**
Phantom	
HDPE	1 – 1.3
PMMA (^{11}C)	1 - 5
Water gel	6 - 10
Tissue gel	10
In vivo	
Rat	15
Human muscle	0.06
Human cortical Bone – Cranial base irradiation	0.09
Human fat – Spine irradiation	0.08
Human fat – Cranial base irradiation	0.20

c) Spatial distribution

The spatial distribution of the generated positron emitters is studied in both longitudinal and radial direction of the beam. The generated positron emitters of each occurring nuclear reaction are expected to vary in beam direction, i.e. in phantom depth. Two effects are considered, the kinetic energy E and the proton beam fluence Φ, see eq. (2). The kinetic energy of the proton beam decreases over the depth of the phantom by elastic scattering, generating a higher amount of positron emitters in larger depth. Since the nuclear reaction cross sections depend on the beam energy, the ratio of the generated radionuclides is also depended of the phantom depth. As opposite effect, the occurrence of non-elastic nuclear reactions removes protons from the beam, resulting in a proton fluence decrease over depth, which causes a AC0 decrease. Earlier published studies of

Horst et al. [37] and España et al. [38] show a 20% AC0 increase over 8 cm depth, by 116 MeV proton irradiation, see Figure 4. Since, however, the experiments in this thesis are planned with multiple energy layers, these mono-energetic effects may be diminished.

In radial direction, a small decrease in AC0 near the borders of the target volume is expected, due to spill out of the activity, one-way lateral scattering and the lateral penumbra of the proton beam, which are for proton beam scanning dependent on in-air spot size, in-patient scattering and optimised fluence pattern. Based on the found spatial distribution, a decision is made for VOI positioning in section Spatial distribution.

d) VOI – size

The variability in AC0 estimation of the radionuclides and their resulting ^{15}O:^{11}C-value is expected to depend on the VOI-size. In a small VOI, where a small amount of voxels is included, a large standard deviation over the measured activity concentrations (i.e. lower statistical accuracy of the PET-measurement) is expected compared to a larger VOI. The AC0-value is not expected to be affected by the VOI-size, but a bias may occur in noisy voxels in case of very low count statistics. The increased standard deviation is expected in VOIs smaller than 100 mm^3, i.e. 5.8 mm diameter, approximating 3 times the voxel size (33.5mm^3). Since the mean target volume investigated in this analysis is a 40 mm diameter sphere, VOIs of 40 mm and larger are expected to decrease in mean activity concentration, due to partial volume effects and inclusion of (near) zero-activity voxels around the activation volume. The optimal VOI-diameter is therefore hypothesised between 5.8 mm and 40 mm.

3.2 Clinical parameters

To use aPET elemental tissue decomposition, the constraints for this technique should be within clinical achievable limits. In this research, the maximal time interval before start of PET-acquisition, the minimal dose delivered in the treatment plan, the minimal target volume and the minimal difference in element composition are analysed. The clinical limits within curative irradiation of HNSCCs are outlined here, just as the hypothesised boundaries.

1) Time interval between end of PRT and start PET-acquisition

Transferring the patient from the treatment room to the PET-scanner at our institution is expected to be possible within 8 minutes, 480 seconds. This time includes reaching the patient from the treatment control room, removal of the fixating devices, walking towards the PET-scanner, positioning on the PET-scanner, including fixating devices, and start acquisition.

Tissue decoupling is hypothesised realisable up to 17 minutes (1028 seconds) time delay. Since the half-life value of ^{15}O, the shortest living radionuclide expected, is 2.037 min, no detectable amount of ^{15}O is expected after 10 half-lives, i.e., 20.37 min (1222 seconds). Detection of the radionuclide in at least three time frames is required to decouple the TAC. Therefore, with time frames of 60 seconds, accurate decoupling is expected to be possible in ideal situation until a maximum time delay of 1042 seconds. Since a low amount of activity is detected, compared to a diagnostic PET-scan, the expected maximum time delay is probably smaller than 1042 seconds.

2) Dose planned in the treatment plan

The minimal delivered dose in an HNC treatment plan is 1.55 GyE. This value corresponds with the treatment plan's low dose field in which elective nodes are irradiated, see section "Volume delineation". This relative biological effective dose corresponds with 1.41 Gy physical dose. Therefore, aPET needs to be feasible in at least 1.55 GyE delivered dose. In line with previous study of Cho et al., [44] tissue decomposition is hypothesised feasible at least within 2 GyE.

The number of generated radionuclides depends linearly on the proton fluence, see eq.(2). Which nuclear reactions occur is determined by the energy dependent cross sections. Therefore, increasing delivered dose, without adjusting the energy layers is expected to lead to a linear correlation between delivered physical dose and generated activity. Since this linearity accounts for all present radionuclides and increasing the dose does not change the nuclear reaction specific cross sections, the ^{15}O:^{11}C-ratio is expected to be constant for increased dose.

3) Target volume

The smallest CTV irradiated in described clinical conditions, a single lymph node, is approximately 15.9 mL, see section "Volume delineation". This CTV contains the gross demonstrable extend of malignant tissue and a 5-10 mm boarder, respecting the anatomical borders. Aim of this additional boarder is to include microscopic disease when present. Additional information about the different clinical target volumes can be found in section **APPENDIX B**; Definition of target volumes.

Based on this minimal CTV, aPET needs to be feasible in a target volume of at least 15.9 mL. In the remainder of this study, when target volume is addressed, the CTV is meant. When a larger target volume is irradiated, an increased total amount of activation is produced. The mean AC0 in an equal size volume of interest (VOI), however, is considered to be independent of the target volume. This mean AC0 can be negatively influenced by partial volume effects and one way lateral scattering of the protons around the borders. Therefore, the irradiated target volume should be large enough to widely include a VOI for enough signal, without the occurrence of degrading factors around the VOI-border. The minimal target volume therefore depends on the minimal VOI-size, as defined in the model design analysis.

4) Difference in tissue composition

In this thesis, two comparisons are made, regarding the ^{15}O:^{11}C-ratio.

- In what amount the hypothesised value corresponds with the estimated value
- In what amount the estimated values of the different materials differ from each other.

Table 5 describes the expected ^{15}O:^{11}C -ratio for the irradiation of the different phantoms. This ratio is calculated from eq. (2), with atomic weight information of the phantoms, displayed in Table 6, the cross section values as derived from Figure 3. The mean proton beam energy used in the experiments is used to calculate the ratio.

Table 5; Hypothesised ^{15}O:^{11}C-ratio, based on material specifications, cross sections and equation. PMMA: polymethyl methacrylate.

Material	**Proton beam kinetic energy (MeV)**	**Hypothesised ^{15}O:^{11}C – ratio.**
PMMA	150	**4.0**
Muscle mimicking	**100**	**2.0**
Cortical Bone mimicking		9.67
Adipose Tissue mimicking		**1.52**

CHAPTER 4

Experimental setup

To investigate the parameters, as described in Chapter 3 – Research objectives, nine different treatment plans were created to irradiate five different homogenous synthetic materials of known composition in the Holland Proton Therapy Centre (HPTC) and analysed in the Leiden University Medical Centre (LUMC).

4.1 Materials

- CT- scanner Siemens SOMATOM Definition Edge.
- Proton irradiation beam: ProBeam 360° Rotating Gantry, Varian Medical Systems, Palo Alto, California.
    - Beam spot size @ 70 MeV: σ: 5.75 mm, FWHM: 13.5 mm.
    - Lateral penumbra: ~ 3 mm
- PET/CT–scanner: Siemens Biograph Horizon with TrueV-option, Siemens Healthineers, Erlangen, Germany.
    - Spatial resolution OSEM, FWHM @ 1cm – axial: 4.2 mm transversal: 3.4 mm
    - Effective sensitivity (with time-of-flight option): 29.3 cps/kBq
    - Voxel size: 2.896 x 2.896 mm. Slice thickness: 4 mm. Voxel volume: 33.47 mm^3
- Support for HDPE and PMMA phantom
- Trolley
- Tape and marker for marking
- Laser positioning system
- Stopwatch on mobile phone, Huawei P20 Lite.

Software

- RadiAnt DICOM Viewer 4.6.9, Medixant, Poznan, Poland
- Treatment planning software: RayStation v 6.99, as clinically implemented, RaySearch Laboratories, Stockholm, Sweden
- Vinci 4.96, Max Planck Institute for Metabolism Research, München, Germany
- Excel 2017, Microsoft, Redmond, Washington, United States of America
- MATLAB R2019b, Natick, Massachusetts, United States of America

4.1.1 Phantom specifications

Five different phantoms are irradiated and analysed. First, the aPET tissue decomposition technique is tested in a material where only ^{12}C can be activated. Thanks to its easiness of use, non-toxicity and durability of the material, the commonly used plastic polyethylene is used, with chemical formula $\{C_2H_4\}_n$. The high-density variant is chosen, since high-density polyethylene (HDPE) has multiple mechanical advantages over low density poly ethylene. It has a larger crystallinity and is better resistant against high temperatures. Moreover, it is more rigid and less sensitive to exposure of light and oxygen, compared to the low-density variant. [48, 49] The only radionuclide, expected to be detected after this irradiation is ^{11}C, see Table 2.

After HDPE, a material with one additional element which can be activated is irradiated. Polymethyl methacrylate (PMMA) ($\{C_5O_2H_8\}_n$ is a lightweight plastic with high impact strength, good ultra violet and thermal resistibility, with a chemical formula of $\{C_5O_2H_8\}_n$. [50] Proton irradiation of the additional nuclide ^{16}O generates the positron emitters ^{11}C, ^{15}O and 13N. Finally, three more complex materials are irradiated and analysed. These tissue mimicking materials (TMM) additionally include a small amount of ^{14}N and ^{40}Ca.

The HDPE- and the PMMA-phantom, including the HDPE standard, suitable for both phantoms, are produced by DEMO. DEMO is the Electronic and Mechanical Support Division of the Technical University Delft. Its aim is to facilitate experimental technical and scientific education and research. The TMM phantoms are produced by Gammex.

Table 6; Tissue element composition of used phantoms; Wi: the mass percentage of the tissue. ϱ the density. ϱ_e: relative electron density to water. Elements small in amount are not shown. Data retrieved from manufacturer.

Material	**ϱ (g/cm³)**	**$\varrho_e{}^w$**	**^1H**	**^{12}C**	**^{16}O**	**^{14}N**	**^{40}Ca**
			W_i (%)				
HDPE	0.97		14.4	85.63	-	-	-
PMMA	1.18		8.05	59.98	31.96	-	-
							-
Muscle	1.05	1.02	8.39	68.50	18.45	2.22	2.26
Cortical Bone	1.82	1.69	2.66	30.34	39.08	0.99	26.4
Adipose Tissue	0.95	0.94	9.44	73.50	14.86	2.07	-

4.2 Volume delineation

In total, ten different target volumes are irradiated in nine separate treatment plans, see Table 7. First, a pilot study is performed, irradiating a 5 by 5 cm square, resulting in an target volume of 33.5 cm^3. This treatment plan delivers all spots in one beam energy layer of 200 MeV. For all other treatment plans, the planned doses and volumes are based on ten clinical treatment plans, used for curative primary irradiation of patients treated for HNC in the HollandPTC. [51]

These treatment plans are based on 35 factions, with a total high dose volume of 70 GyE (referred to as CTV7000) and low dose of 54.25 GyE (CTV5425), resulting in respectively 2 GyE and 1.55 GyE per fraction. The dimensions of the smallest and largest CTV7000 per patient are measured in RayStation, just as the total CTVs. The CTVs measured varied from a length of 1.3 and maximal 14.1 cm. The former in a lymph node metastases and the latter in a large volume, containing multiple lymph node levels. The volume and the shapes of the experimental target volumes are based on these clinical data. Vmin is considered the CTV of a lymph node, Vmean of a tumour CTV with limited contributing lymph nodes and Vmax as a bundling of lymph node stations. The tissue equivalent materials are 1 cm thick slabs and therefore not able to be irradiated with a volume. Therefore, the dose in these phantoms is delivered in a 38.5 cm^2 square with 0.5cm depth, instead of a three-dimensional target volume, like in the other treatments plan. See

Table **8** for an overview of the target volume dimension.

Since the CTV7000 is planned to receive 2 GyE per fraction, this is used as experimental mean dose (Dmean). The CTV5425 receives 1.55 GyE per fraction. Since in the human body, the amount of generated radionuclides decreases rapidly, due to biological wash-out and physical decay, the expected generated activity is lower than the activity measured after phantom irradiation of 1.55 GyE. To compensate for these effects, a lower boundary of 0.5 GyE (Dmin) is used for the phantom experiments. A high dose plan is also carried out to optimise the experiment and to approach potential hypofractionated high dose proton irradiation. In these experiments, 10 GyE is irradiated (Dmax). The target volumes are delineated on CT-scans of the phantoms, acquired with a diagnostic neurological protocol, chosen for the high spatial resolution.

Table 7; Overview experiments. HDPE: high density polyethylene. PMMA: polymethyl methacrylate. For volume and dose specifications, see

Table 8 and **Table 9**.

Material	**Volume**	**Dose**	**Experiment Nr.**
HDPE	Vpilot	Dmean	Pilot
HDPE	Vmean	Dmax	1
PMMA	Vmean	Dmax	2
PMMA	Vmin	Dmean	3.1
PMMA	Vmax	Dmean	3.2
PMMA	Vmean	Dmean	4
PMMA	Vmean	Dmin	5
Cortical bone mimicking	Vcircle	Dmean	6
Muscle mimicking	Vcircle	Dmean	7
Adipose tissue mimicking	Vcircle	Dmean	8

Table 8; Experimental target volume definition as defined in treatment plan. All target volumes are positioned in beam direction, except for Vmax, which is positioned in radial direction.

Target Volume	**Shape**	**Length (cm)**	**Width (cm)**	**Volume (cm^3)**
Vpilot	Square	5	5	33.5
		Radius (cm)	**Height (cm)**	**Volume (cm^3)**
Vmin	Cylinder	1.3	3.0	15.9
Vmean	Sphere	2.0	2.0	33.5
Vmax	Cylinder	2.7	13	298
Vcircle	Circle	3.5	0.5	19.2

Table 9; Experimental dose definition as defined in treatment plan. GyE: Gray-Equivalent dose.

Planned dose	**Dose (GyE)**
Dmin	0.5
Dmean	2.0
Dmax	10

4.3 Treatment plan

The treatment plans are created separately in planning software RayStation by optimizing for multiple conditions and constraints set on the created target volume and assisting fictitious organs at risk volumes. The conditions include a minimal dose, a maximal dose, a minimal dose-volume histogram coverage and a uniformity constraint to the target volume. The three-dimensional spherical annular volume around the target volume is constrained on a maximum dose. The external volume, i.e. the phantom volume outside the target volume and the organs at risk, is planned on a maximum dose fall-off at 1.0 cm. The weights and values of these conditions are iteratively defined and differ per treatment plan.

The following criteria are aimed to achieve:

1) At least 98% of the clinical target volume has a minimal coverage of 95% of the planned dose. (D98)
2) The maximum dose is maximal 125% of the planned dose.
3) The maximum dose is positioned within in the defined clinical target volume.
4) In a margin of maximal 1 cm around the target volume, maximal 130% of the defined dose is delivered.

To ensure the first criterium, it was not possible to fulfil the second requirement in the low dose treatment plan (exp. 5), the muscle tissue treatment plan (exp. 7) and the adipose tissue treatment plan (exp. 8). In the low dose experiment, the maximum delivered dose is 0.98 GyE, instead of the intended 0.5 GyE, leading to a maximum dose of 196% of planned dose, instead of the aimed 125%. Since this dose is still less than half the dose of the normal dose experiment, this maximum dose is considered acceptable. In the adipose and the muscle mimicking tissue, the maximal delivered dose is 2.72 GyE, respectively 2.65 GyE, resulting in a fraction of 1.36, respectively 1.33 of the planned dose. When analysing the results of these two experiments, a slightly higher amount of delivered dose, compared to the planned dose, should be considered. In the other cases, the criteria are achieved.

In contrast to treatment planning in clinical HNC proton therapy, no robust treatment planning is applied. In robust planning, multiple irradiation scenarios are modelled, based on uncertainties in patient and organ motion, inaccurate patient positioning or geometric, beam and setup uncertainties. Based on these scenarios, definitive dose delivery on the CTV is planned, resulting in a more robust treatment plan. This increased robustness is, however, at the cost of a decreased therapeutic index. Since no internal or external motion occurs in the stationary phantom irradiation, robust planning causes an additional, undesired uncertainty, without the advantage of correction for motion.

The result is a heterogeneous treatment plan, see Figure 5, of multiple irradiation spots, between 173 and 2639 spots for the treatment plans. Excluding the pilot experiment, minimal 5 and maximal 28 energy layers were used with a beam energy of minimal 70 and maximal 153 MeV, see Table 3. All beam energies are above the activation threshold, as described in Table 2. The mean dose experiment with minimal and mean volume are planned in one treatment plan. The number of layers depend on the longitudinal length

of the target volume. Therefore, the Vmax experiment and the tissue equivalent two-dimensional slabs, which have a target volume, long in longitudinal direction, show a large range of energy layers.

The number of monitor units per fraction varied between 1987 (Vmean@Dmin) and 34577 (Vmean@Dmax) monitor units, with a predefined minimum number of monitor units per spot of 3 to ensure adequate dose delivery. The spot spacing was depended of the energy layer and varied in every experiment with a minimal spot spacing of 0.47 cm (muscle) and 0.66 cm (cortical bone).

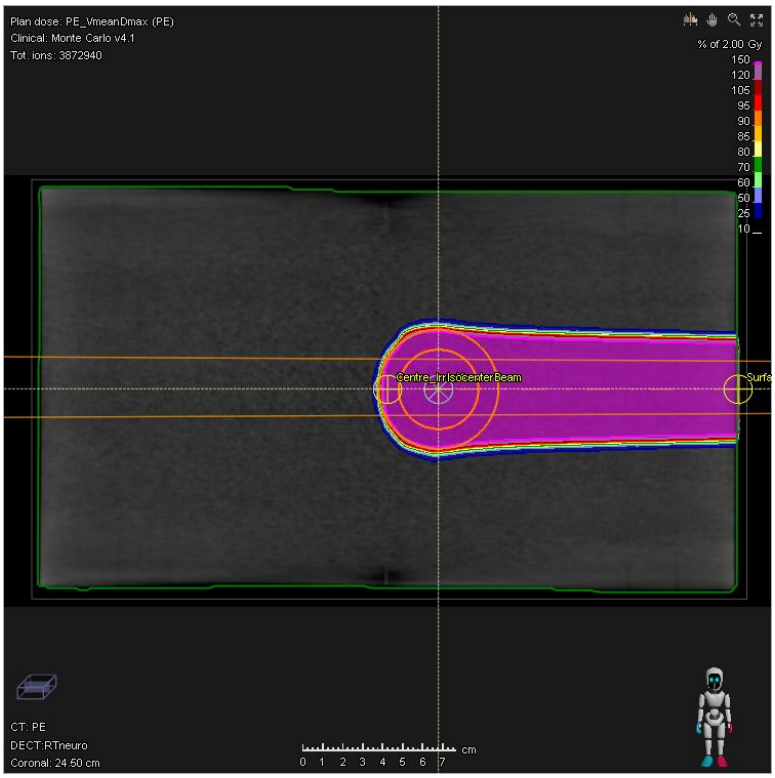

Figure 5; Treatment plan of the high dose experiment in high-density poly ethylene phantom. Performed in RayStation. Coronal view

Table 10; Characteristics of the treatment plans. Energy layers indicate number of layers in the treatment plan and in parentheses the minimal and maximal proton beam energy. Dose rate is proton fluence. MU: monitor units. fx: fraction. HDPE: high density polyethylene. PMMA: polymethyl methacrylate.

Material	Experiment	Nr. of spots	Energy layers (MeV)	Dose rate (·10³ MU/min)	Spot spacing range (mm)	Nr. of monitor units (·10³MU/fx)
PE	Pilot	676	1 (200, 200)		(2.0, 2.0)	5.0
PMMA	Vmean@Dmax	503	9 (134, 161)	82	(5.2, 5.6)	29
	Vmean@Dmax	645	9 (143, 172)	72	(5.2, 5.6	35
	Vmin@Dmean	871	9 (143, 172)	35	(5.2, 5.6	11
	Vmean@Dmean					
	Vmax@Dmean	2639	12 (172, 165)	47	(5.0, 5.5	31
	Vmean@Dmin	173	5 (153, 168)	15	(5.3, 5.6	20
Tissue mimicking material	Muscle	334	18 (70, 114)	16	(4.7, 5.7	5.0
	Cortical Bone	498	28 (70, 146)	13	(5.4, 6.6	5.8
	Adipose	361	17 (70, 109)	21	(5.8, 6.4	6.0

4.4 PET-scan preparation

The phantom is positioned on the PET/CT – scanner and its position is marked with tape and the extern laser positioning system. The activation PET protocol is started and a topogram is made, whereafter the bed position of the phantom is marked on the scanner.

4.5 Proton beam irradiation

The phantom is transported to gantry 2, the 'Citer'. The laser positioning system is aligned at the isocentre of the beam, as defined in the treatment plan. For the HDPE- and PMMA phantom, this isocentre is defined in the transversal centre of the phantom and 15 cm longitudinal from the surface for the HDPE- and PMMA phantom. The beam is delivered perpendicular on the flat surface of the phantom. The HDPE-phantom is positioned in transversal direction on the table and the PMMA-phantom in longitudinal direction. In the TMMs, which are positioned flat on the table on a rectangular stand to prevent partly irradiating the table, this isocentre is located at 5 cm depth of the flat side of the phantom. The table is then rotated as described in the treatment plan. Validation of the beam position in the TMMs is performed with radiochromic film. The radiation set-up for the three types of material are visualised in Figure 6. After accurate laser positioning of the table and the phantom, with an uncertainty of maximal 1 mm, the treatment plan is delivered. The duration of this irradiation is determined by the treatment plan and was maximal 28 seconds. The maximal time delay between end of

proton irradiation and start PET-acquisition is 237 seconds for the pilot experiment, following 146 seconds for the maximal dose experiment, see
Table **11**.

Table 11; Time delay between end of proton irradiation and start PET-acquisition. These durations are timed manually with a stopwatch. The Vmin@Dmean and Vmean@Dmean experiments are created in the same treatment plan. HDPE: high density polyethylene. PMMA: polymethyl methacrylate. PRT: Proton radio therapy. PET: Positron emission tomography.

Material	**Experiment**	**Duration of treatment plan (sec)**	**Time delay end PRT – start PET (sec)**
PE	Pilot	2	237
PMMA	Vmean@Dmax	21	129
	Vmean@Dmax	29	146
	Vmin@Dmean	19	128
	Vmean@Dmean		
	Vmax@Dmean	40	142
	Vmean@Dmin	8	114
Tissue mimicking	Muscle	20	84
	Cortical Bone	27	78
	Adipose	17	88

Figure 6; Experimental proton irradiation set-up of poly-ethylene phantom (HDPE) (left upper) , polymethylmethacrylate phantom (PMMA) (right upper) and tissue mimicking slabs (TMM), including radiographic film for beam positioning verification. (left down)

4.6 PET-acquisition

Directly after completion of the irradiation, the phantom is lifted on a trolley and moved towards the PET/CT–scanner in the room, directly on the other side of the hallway. This is done fast. The interval between end of irradiation and start of PET was measured with a stopwatch. After positioning the phantom on the PET-table, based on the pre-set tapes and lasers, the table is moved toward the start position, defined at the topogram and the PET-acquisition is started. The acquisition is performed in list mode in one bed position. In the high dose experiments, the acquisition is performed for 45 minutes, while for the other experiments this duration was 30 minutes. Since decay correction is automatically applied in the reconstructions, the isotope setting was set to the slowest decaying isotope available in the clinical system settings, i.e. ^{22}Na, with a half-life of 2.6 year and an injected dose of 0.1 MBq. A 110 kVp CT–scan of diagnostic quality is performed after finishing the PET–acquisition with a HD FOV of 70 cm. The CT-images are FBP reconstructed using a b31s kernel in 4 mm thick slices. The data are subsequently exported for further analysis. The phantom is transported to the storage and is considered negligible active after decay for 10 half–lives of the slowest decaying isotope with relevant contribution, which means for ^{11}C with a half-life of 20.4 minutes, after 3

hours and 24 minutes. The decay time, set for ^{22}Na, leads to a decrease in activity of 0.003% in the full time span of our experiment, 60 minutes. Since 99.997% of the activity is still left, the amount of decay is considered negligible and will thus not be corrected for.

4.7 Reconstruction method

The four-dimensional acquired list mode data are binned in multiple time frames, dependent of the parameter to be analysed. An integral reconstruction is also made, considering the full PET-acquisition in one time frame, like a conventional static PET-image. These multiple three-dimensional datasets are reconstructed using FBP and iterative reconstruction using OSEM with time of flight correction, but without resolution modelling. The OSEM reconstruction was performed with 4 iterations and 10 subsets. Both OSEM as FBP reconstruction were performed with a matrix size of 256 with zoom 1.00 and no offset. A Gaussian filter is applied with 3.0 mm full-width-at-half-maximum (FWHM). Matched attenuation correction and relative scatter correction was performed, based on the high dose CT performed directly after PET-acquisition. The data are corrected for random coincidences and dead time, according the clinical protocol. Due to the occurrence of multiple isotopes, all with their own positron range, no positron range correction has been performed.

4.8 Determination of activity concentration

In Vinci software, the mean activity concentration is quantified in the different time frames by defining spherical VOIs. The VOIs are placed in the same coordinates in all series, resulting in near-identical volumes that can differ in size from the original volume by the in- or exclusion of boundary voxels. The VOI is copied over the binned time frames and the mean activity concentrations and standard deviation per VOI is determined using Vinci and exported. This data is, together with its time stamps, imported in MATLAB. The result is a $N \times 1$ vector of mean activity concentrations and a $N \times 1$ vector of corresponding time frames, with N the number of time frames. These two vectors per reconstruction are used as the input for the model, defined in section Model definition.

CHAPTER 5

Model selection

5.1 Methods model design

The analysis methods described in this section are performed on the high dose HDPE and the high dose PMMA experiment.

5.1.1 Reconstruction technique

The FBP and OSEM integral reconstructed images of the high dose PMMA-experiment are compared visually and quantitively, by comparing the mean activity concentration and its standard deviation. The differences in spatial resolution are determined by drawing a 1.0 cm width cuboid shaped dose profile perpendicular to the beam path.

Since the potential positive bias due no non-negativity constraints in the OSEM algorithm is caused by an insufficient number of counts, the occurrence of this artefact is investigated by comparing the AC0s for different frame durations. In shorter time frames, less counts are present. The time frames, nine for each of eight different time frame, ranged between 5 to 60 seconds. The pilot data are corrected for ^{11}C decay during acquisition.

5.1.2 Model definition

Let the measured mean activity concentration in interval t be defined by $A(t)$, representing the TAC. Now, consider the following statistical model for $A(t)$:

$$A(t) = f(t, \boldsymbol{\beta}) + \epsilon \tag{5}$$

where the nonlinear function $f(t, \boldsymbol{\beta})$ is given by:

$$f(t, \boldsymbol{\beta}) = \sum_{j=1}^{K} (\gamma_j \beta_j e^{-\lambda_j t}) . \tag{6}$$

Here, K is the number of nuclides and $\boldsymbol{\beta} = (\beta_1, \dots, \beta_K)$ is a K x 1 vector of parameters to be estimated. γ_j and λ_j are constants, specific for each nuclide. γ_j represents the branching fraction and λ_j the decay constant as shown in **Table 3**. Furthermore, it is assumed that the residuals ϵ are independent and normally distributed, i.e. $\epsilon \sim i.i.d.N(0, \sigma^2)$. Under these assumptions eq. (5) is conventionally estimated using NLS. Other studies follow this approach to estimate the parameters of the TAC curve. [44, 47, 52]

Under the assumptions of eq. (5), it follows that $A(t) \sim N(f(t, \boldsymbol{\beta}), \sigma^2)$. Hence, $\boldsymbol{\beta}$ could also be estimated using maximum likelihood estimation (MLE) based on the normal distribution function. An advantage of this would be that the resulting Akaike information criterion (AIC) can be calculated for model selection.

Note that the distributional assumptions about the residuals of model (5) violates the non-negativity constraint that is typical in counting data. Alternatively, a different

model might be considered, where $A(t)$ follows a Poisson distribution with rate parameter $\Lambda(t) = f(t, \boldsymbol{\beta})$ However, the Poisson distribution has the additional constraint that both the variance and mean of the distribution of $A(t)$ are equal to $\Lambda(t)$. This assumption is likely to be violated due to added noise in the PET- detection and the reconstruction phase. In section Activity concentration validation the mean activity concentration is compared with its variance and shows these are different. Although not statistically tested, provides this observation evidence against the assumption that $A(t)$ follows a Poisson distribution.

Therefore, the conventional literature is followed and the parameters are estimated by NLS. Using this approach $\boldsymbol{\beta}$ can be estimated by solving the following minimisation problem:

$$\widehat{\boldsymbol{\beta}}_{NLS} = \arg \min_{\boldsymbol{\beta}} \left[\sum_{i=1}^{N} (A_i(t) - f_i(t, \boldsymbol{\beta}))^2 \right] \quad (7)$$

where N is the number of measurements. Moreover, $A_i(t)$ and $f_i(t, \boldsymbol{\beta})$ represent our measurements of $A(t)$ and $f(t, \boldsymbol{\beta})$, respectively, with $i = 1, 2, \ldots, N$.

Recall that $f(t, \boldsymbol{\beta})$ is a non-linear function and solving (7) requires an iterative process, such as the Gauss-Newton algorithm [53] or the Levenberg-Marquardt algorithm [50][51]. In this process, an initial value of $\boldsymbol{\beta}$ needs to be provided ($\boldsymbol{\beta}_{(0)}$), which is updated iteratively until the difference between two successive $\boldsymbol{\beta}_{(k)}$ (or the resulting sum of squared residuals) becomes sufficiently small. The Levenberg-Marquardt algorithm interpolates between the Gauss-Newton algorithm and the method of gradient descent, making it more robust for initial values $\boldsymbol{\beta}_{(0)}$ that are far from the minimum. To this end, the Levenberg-Marquardt algorithm in the NLS estimation of eq. (5) is used. The NLS estimation is performed in MATLAB by the nonlinear regression solving function 'fitnlm'. The stopping criteria is a relative change in the sum of squared residuals of $1 \cdot 10^{-8}$.

To avoid convergence to a local minimum, the initial parameter estimator should be chosen as close as possible to the global minimum. First of all, it is assumed that the sum of the elements of $\widehat{\boldsymbol{\beta}}$ reflects the total generated mean activity concentration. Therefore, this total amount of generated mean activity concentration is assumed to be higher than the measured mean activity concentration at the first time frame, $A(1)$. Moreover, an approximation of the sum of the elements of $\widehat{\boldsymbol{\beta}}$ can be achieved by performing an ordinary least squares regression of $A(t)$ on t. The resulting estimated constant of this regression would serve as the approximation of the sum of the activity concentration of the radionuclides. This, together with our hypothesised ratio of activity concentration for the separate nuclides (defined in section Cross sections), can be used to provide an initial value for $\widehat{\boldsymbol{\beta}}$. Finally, experimentation with different initial values show robust results.

Based on the estimated parameters, the initial mean activity concentration, AC0, directly after end of irradiation, is determined for the included radionuclides. The ^{15}O:^{11}C -ratio is defined as the ratio of the AC0 ^{15}O to AC0 ^{11}C.

Model selection

Different models are estimated, varying in time frame duration and number of included parameters. The dataset included reconstruction of time frames of 15, 30, 60 and 90 seconds and a reconstruction includes time frames of 30, 60 and 90 seconds. Models including two nuclides, ^{11}C and ^{15}O are compared with the models modelling three nuclides, ^{11}C, ^{15}O and ^{13}N.

The model is selected that:

1) Predicts the presence of the radionuclides correctly. This is determined by testing whether the parameters are statistically significant different from zero at a $\alpha = 0.05$ level of significance.
2) Has the lowest AIC-value or which shows substantial support to be used above the comparable model with the lowest AIC-value.
3) Has the lowest standard deviation of the parameter estimates

Estimation results

When the model predicts the presence of the radionuclides correctly, a statistically significant amount of ^{11}C is found. The other radionuclides are not present. For correct prediction of the generated radionuclides in the PMMA–phantom experiments, a statistically significant amount of ^{11}C, ^{15}O and ^{13}N is estimated. This is determined by calculating the 95% confidence interval of the parameter estimates.

In order to calculate the confidence interval, the $N \times K$ matrix $\boldsymbol{J}$ is determined as the Jacobian matrix evaluated at $\widehat{\boldsymbol{\beta}}$:

$$\boldsymbol{J} = \frac{\delta \boldsymbol{f}(t, \boldsymbol{\beta})}{\delta \boldsymbol{\beta}'} \Bigg|_{\widehat{\boldsymbol{\beta}}}. \tag{8}$$

Note that the $N \times 1$ vector $\boldsymbol{f}(t, \boldsymbol{\beta})$ is the representation of eq. (6) for the N observations.

Now, the $K \times K$ covariance matrix of $\widehat{\boldsymbol{\beta}}$ is estimated by

$$Var(\widehat{\boldsymbol{\beta}}) = (\boldsymbol{J}' \cdot \boldsymbol{J})^{-1} \cdot \sigma^2, \tag{9}$$

where σ^2 is estimated by the sample mean squared error:

$$\hat{\sigma}^2 = \frac{1}{N-K} \sum_{i=1}^{N} \left(A(t)_i - \hat{A}(t)_i\right)^2. \tag{10}$$

The standard error of our $\widehat{\boldsymbol{\beta}}$, given by the square root of the diagonal elements of $Var(\widehat{\boldsymbol{\beta}})$, is used to calculate the 95% confidence interval of our estimators $\widehat{\boldsymbol{\beta}}$.

The parameter estimates are statistically different from zero ($\alpha \leq 0.05$), when zero is included in the confidence interval.

AIC

The AIC is a relative measure to compare the quality of multiple equal approximation models with a different number of estimators. The AIC algorithm is based on the maximum likelihood, $L\left(\widehat{\beta}_{J_{MLE}}\right)$, penalised with the number of parameters estimated in the model, *K*:

$$AIC = -2ln(L\left(\widehat{\beta}_{J_{MLE}}\right) + 2K. \quad (11)$$

Note that under the assumption of model (5), NLS and MLE result in the same estimators, as maximising the likelihood function comes down to solving the same minimisation problem as (5). In fact, the 'fitnlm' function in MATLAB assumes normally distributed error terms when estimating using NLS and also generates an AIC value for the NLS regression. [54]

To maintain the parsimony of the model, the AIC should be minimised. According to Burnham *et al.* the difference between two AIC values can be used to say something about how much worse the model with the higher AIC value performs compared to the model with the lower AIC value (AIC_{min}). A difference of 2 is considered to have substantial evidence to still use the model with the higher AIC. A difference between 4 to 7 shows considerable support and models with an AIC difference larger than 10 are considered to have no support. [55]

Based on the results, the model is selected with the highest standard deviation, which predicts the presence of the radionuclides correctly. The AIC difference may not be more than 10 in favour of the alternative model.

5.1.3 Activity concentration validation

The comparison of the generated activity concentration of positron emitters and the ratio between them is performed with the HDPE and PMMA high dose experiment. These 10GyE experiments are expected to generate the highest amount of positron emitters and therefore, the best activation PET quality, compared with the other experiments.

In the integral PMMA high dose experiment, a spherical VOI of 14.3 ml (30 mm diameter) is drawn in the target volume to investigate the deviation within this volume.

5.1.4 Spatial distribution

The range of the proton induced activity production is visually compared with the range of the planned dose. The amount of generated activity concentration of the three nuclides and the corresponding ^{15}O:^{11}C -ratio are determined over the irradiated volume of the phantom in three dimensions. For this, a cuboid activation profile in longitudinal (25mm width), transversal (8mm width), and sagittal (10mm width) direction is placed in Vinci.

To quantify the spatial activity concentration distribution in beam direction, twenty ellipsoid VOIs are positioned in longitudinal direction, all partly overlapping. Every ellipsoid VOI has a diameter of 30 mm in radial direction and 15 mm in longitudinal direction. Half of the VOIs are used for analysis to approach spatial independent observations. The VOI-positioning is visualised in Figure 7. Since the number of included voxels per VOI varies between 200 to 220, the volume varies between 6.7 and 7.4 mL. For the range of the activated volume, i.e. between 1 cm and 17

cm, the AC0 is determined by the defined method in 'Model selection'. The average μ and the standard deviation σ of the analysed AC0 is determined for the different VOIs. The coefficient of variant (COV) between the variables is calculated by:

$$COV = \frac{\sigma}{|\mu|}. \quad (12)$$

The COV is a measure to compare the variability in data, independent of the data's unity.

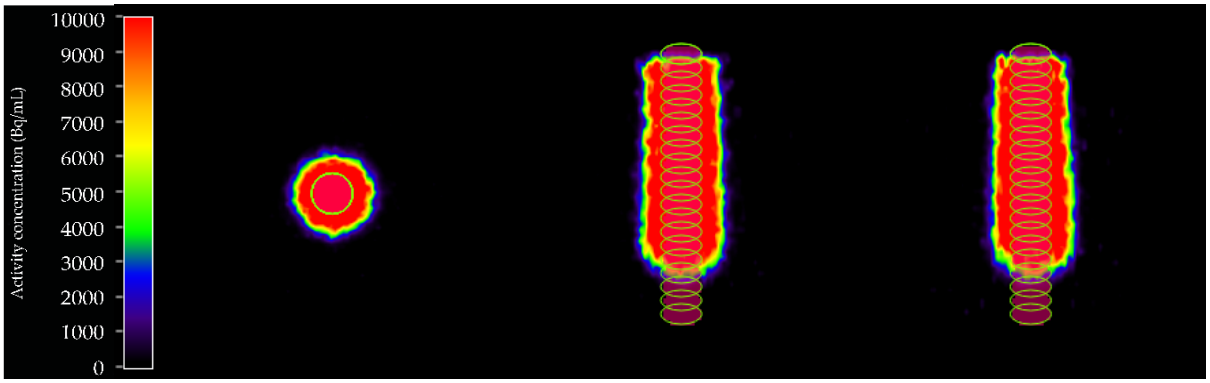

Figure 7; VOIs positioned for depth analysis in 10 GyE PMMA experiment, reconstructed iteratively. Scale is Activity concentration (Bq/ml). The target volume was a 4 cm diameter sphere. The VOI-sizes were 30 x 15 mm diameter. Beam entrance is from above. Left image is in transversal plan, the centre in coronal plane and the right image in sagittal plane. Note that for statistical analysis, only half of the VOIs is used to prevent overlapping. VOI: volume of interest. GyE: Gray-Equivalent. PMMA: polymethyl methacrylate.

5.1.5 VOI – size

The effect of the VOI–size on the estimated AC0 is, as part of the model selection procedure, first determined on the PMMA high dose experiment, representing ideal situation. Spherical VOIs in seven sizes, ranging from 5 to 50 mm diameter (0.134 mL-65 mL i.e. 4-1968 voxels) are analysed in Vinci software. To improve precision, five VOIs of each size were analysed. Since the AC0 in beam direction is considered constant, the VOIs are drawn over the depth of the phantom, leaving 1.5 cm space from the entrance- and exit boarders (see section discussion Spatial distribution). The centres of the VOIs were placed 2.1 cm from each other, resulting into independent measurements for VOI-size 5, 8, 10 and 20 mm. The resulting VOI-sizes 30, 40 and 50 mm were thus partly overlapping. To validate the results in more clinical representative situation, the VOI-size influence is subsequently tested in the mean dose experiments. For potential effects of the VOI-location on the AC0 as studied in the section 'Spatial distribution', is compensated for by equal centre positioning of the different VOI sizes. On the contrary, the boundaries of the activated volume, as defined in this section, are taken into account.

5.2 Results model design

5.2.1 Reconstruction technique

The differences in image quality between the two integral reconstruction methods are clearly visible in Figure 8. The FBP reconstruction shows many streak artefacts. These artefacts are not present in the OSEM image. The mean AC0 and its standard deviation is similar for FBP and OSEM-reconstruction, see **Table 12.** The 1 cm width radial dose profile shows an equal activity profile, see **Figure 9.**

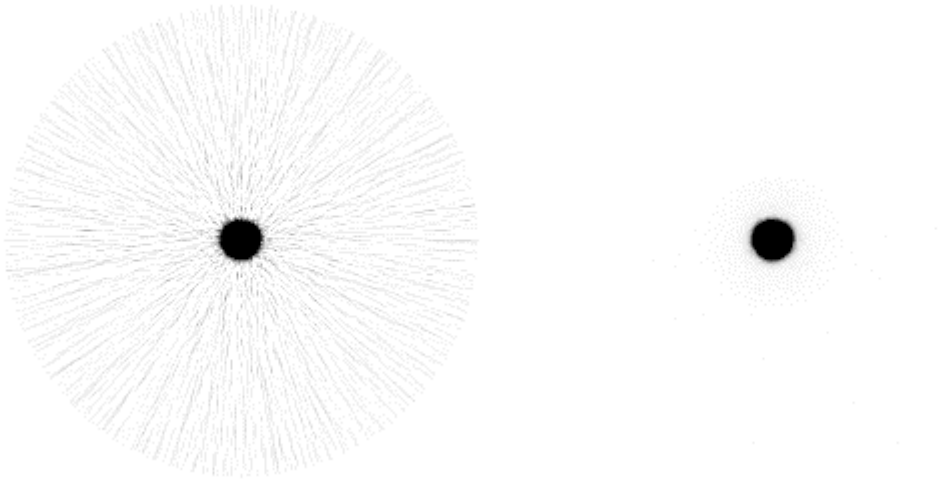

Figure 8; Integral reconstruction of the PMMA Vmean@Dmax (4 cm sphere, 10 Gy) experiment with Filtered Back Projection (left) and Ordered Subsets Expectation Maximisation (right)

Table 12; Activity concentration of a 3 cm diameter sphere in the integral high dose PMMA - experiment. AC0: Initial activity concentration. FBP: Filtered Back Projection OSEM: Ordered Subsets Expectation Maximisation. PMMA: polymethyl methacrylate.

	AC0 (kBq/mL)	**Standard Deviation (kBq/mL)**
FBP	3.86	0.34
OSEM	3.85	0.32

In Figure 10 the mean total ACs for the different frame durations, directly after end of proton irradiation are plotted. No correlation between the mean AC0 and the frame duration can be found. The standard deviation is decreased in larger time frames.

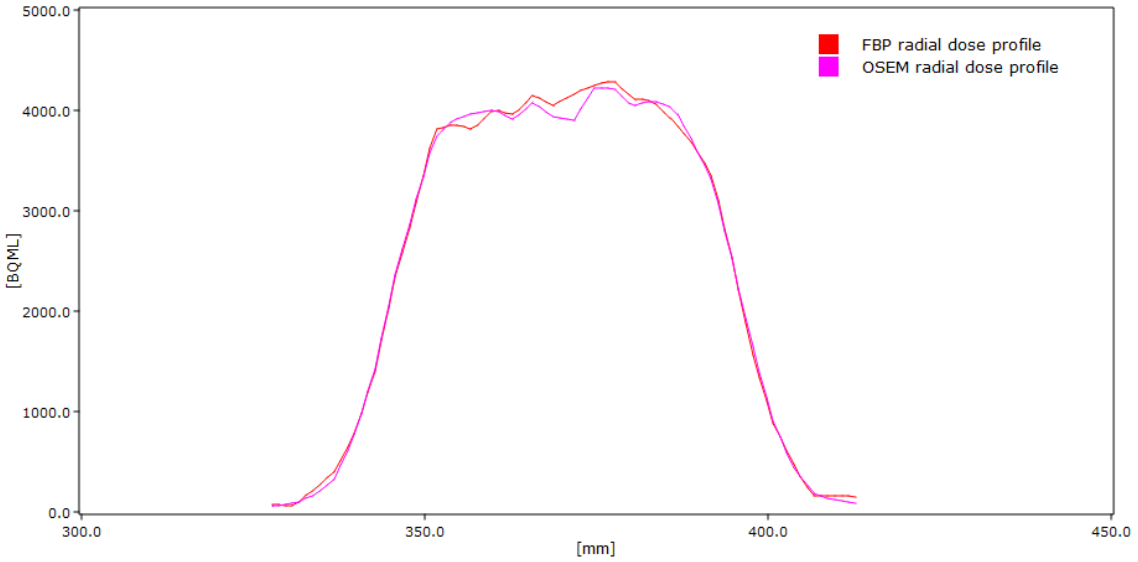

Figure 9; Radial cuboid one cm width dose profile of the integral reconstruction of the high dose PMMA-experiment for both filtered back projection (FBP, red) and ordered subset maximisation expectation (OSEM, purple) X-as: Radial width. Y-as: Activity concentration (Bq/ml)

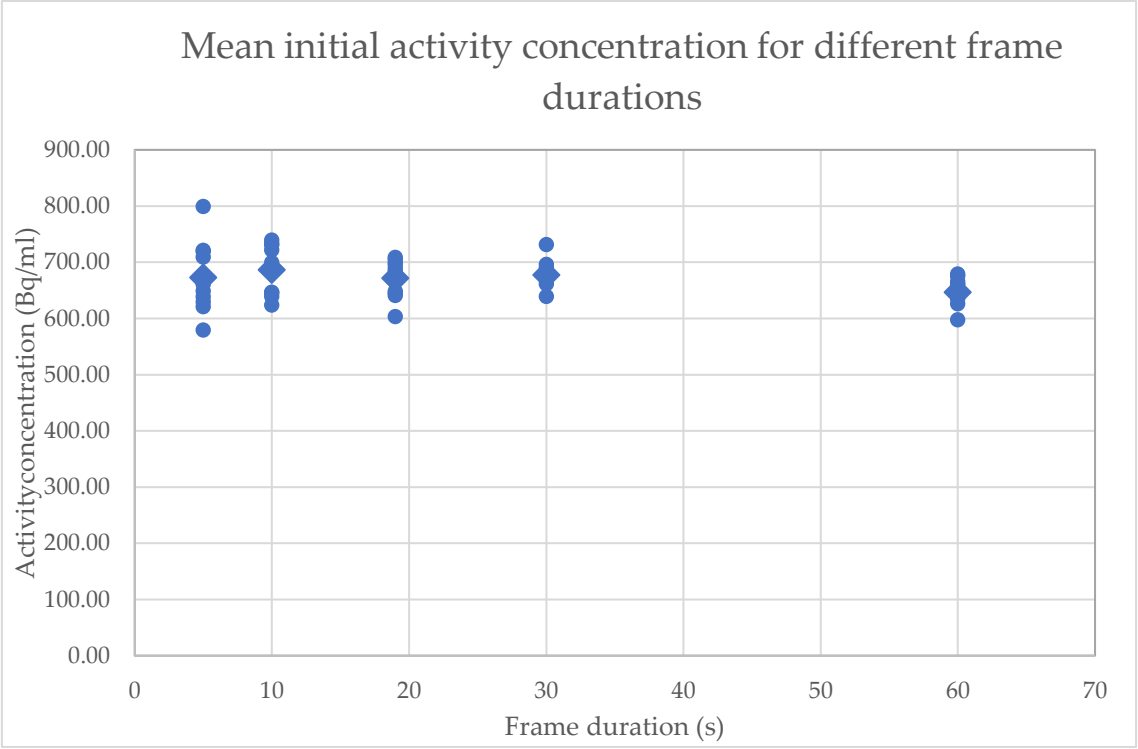

Figure 10; Mean initial activity concentrations at different frame durations, based on OSEM–reconstructed data from the HDPE–pilot experiment. In this experiment 2 GyE dose is delivered in a 25 cm^2 square. Diamond indicates the average. HDPE: high density polyethylene. OSEM: ordered subset maximisation expectation

5.2.2 Estimation results

In Table 13, the mean activity concentration with its standard deviation and p-value per nuclide is visualised for the different applied models. For the HDPE high dose experiment, only ^{11}C is expected to be present in the tissue after proton irradiation. For the two nuclide model, estimation with time frames of 60 seconds and larger predicted this ^{11}C presence correctly and significantly. The three nuclide model estimated the presence of the radionuclides significantly for all different time frames.

For the PMMA high dose experiment, all three nuclides are expected to be present in the tissue. The two nuclide model estimated the presence of all three radionuclides correctly in all cases. For the tree nuclide model, estimation with 90 second timeframes did not provide a significant amount of ^{13}N in the tissue.

Correct estimation of the presence of the nuclides was only able in the two and three nuclides model with time frames of 60 seconds and time frames of 30, 60 and 90 seconds, although the latter with a larger p-value than the first.

Table 13; Estimation results for several models in two different high dose experiments (HDPE and PMMA) for different time frames and number of estimated parameters (radionuclides). AC0: estimated initial mean activity concentration. ±: one standard deviation. 30,60,90 = 15x30 + 15x60 + 15x90 seconds. HDPE: high density polyethylene. PMMA: polymethyl methacrylate. *** p <0.001, ** p< 0.01, * p <0.05.

	Time frames (sec)	**Two radionuclide model**		**Three radionuclide model**		
		^{11}C AC0 (Bq/mL)	^{15}O AC0 (Bq/mL)	^{11}C AC0 (Bq/mL)	^{15}O AC0 (Bq/mL)	^{13}N AC0 (Bq/mL)
HDPE	15	7047*** ±25	333* ±129	6942*** ±89	134 ±206	198 ±161
	30	7088*** ±33	406** ±161	7024*** ±115	289 ±259	120 ±208
	60	7059*** ±26	231 ±122	6912*** ±91	-20 ±191	273 ±163
	90	7024*** ±32	37 ±140	6893*** ±113	-175 ±225	243 ±202
	30,60,90	6750*** ±42	478 ±174	6624*** ±170	301 ±289	215 ±282
PMMA	15	6959*** ±30	22819*** ±191	6258*** ±103	21821*** ±292	833*** ±191
	30	6952*** ±32	21857*** ±195	6516*** ±104	20881*** ±286	841*** ±193
	60	6923*** ±41	19685*** ±231	6416*** ±122	18622*** ±313	969*** ±225
	90	6775*** ±41	18396*** ±216	6778*** ±148	18403*** ±358	-7 ±271
	30,60,90	6970*** ±51	21790*** ±254	1233*** ±172	20585*** ±357	1233** ±292

In all analysed experiments an increase in standard deviation occurs by longer time frames, with the highest standard deviation for the 30,60,90 time frames. In both experiments, the modelling of three nuclides provided a larger standard deviation than the modelling of two nuclides, see Table 13.

The AIC–values of the models are visualised in Table 14 for the HDPE and PMMA high dose experiments. The difference between the AIC of one model compared to the AIC_{min} model is given. For HDPE, with a maximum difference of 1 between the two models, all models show substantial support to be used instead of the minimal model. For PMMA, however, the differences between the 15 seconds, the 30 seconds, the 60 seconds and the combined 30,60,90 seconds time frames are large. The model with the largest AIC in these time frames have no support to be used instead of the AIC_{min} model.

Table 14; AIC - values of the two models. AIC: Akaike information criterion. HDPE: high density polyethylene. PMMA: polymethylmethacrylate.

Material	**Frame time (sec)**	**2 radionuclide model**	**3 radionuclide model**	**$\Delta(AIC_{model} - AIC_{min})$**	**AIC_{min}**
HDPE	**15**	2296	2296	0	-
	30	1133	1133	0	-
	60	516	515	1	3 radionuclides
	90	345	344	1	3 radionuclides
	30,60,90	563	563	0	-
PMMA	**15**	2359	3242	883	2 radionuclides
	30	1129	1112	17	3 radionuclides
	60	555	540	17	3 radionuclides
	90	358	359	1	2 radionuclides
	30,60,90	578	563	15	3 radionuclides

5.2.3 Activity concentration validation

Table 15 shows the mean AC0s for the high dose HDPE and PMMA experiments with their ^{15}O:^{11}C -ratio. The summed AC0 of HDPE and PMMA is with 0.7 and 2.6 kBq/mL/Gy smaller than predicted. The ^{15}O:^{11}C -ratio of 2.9 is also lower than the expected 4.0.

In the 14.3 mL spherical VOI drawn in the integral reconstruction, the minimal, mean and maximal AC0 are 2.2, 4.0, 4.4 kBq/mL, respectively, with a standard deviation of 0.2 kBq/mL. These measurements strengthen the presumption that the data are not Poisson distributed, since the mean does not correspond the variance.

Table 15; Estimated initial mean activity concentrations (AC0) for the high dose HDPE and PMMA experiments in 60 seconds time frames. ±: one standard deviation. HDPE: high density polyethylene. PMMA: polymethylmethacrylate

	∑(^{11}C,^{15}O,^{13}N)	**^{11}C**	**^{15}O**	**^{13}N**	**^{15}O:^{11}C, Hypothesised**	**^{15}O:^{11}C, Estimated**
	AC0 (kBq/mL)					
HDPE	7.2 ±0.2	6.9 ±0.1	0.0 ±0.2	0.3 ±0.2	0.0	0.0
PMMA	26.0 ±0.2	6.4 ±0.1	18.6 ±0.3	1.0 ±0.2	4.0	2.9

5.2.4 Spatial distribution

In Figure 11, the planned dose and the total detected activity by the generated positron emitters of the PMMA high dose experiment are visualised. The depth-dose graph and the depth-activity graphs are additionally visualised. The depth-dose graph shows a spread-out Bragg peak between 13 and 17 cm distal from the entrance point. This high dose delivery corresponds with the position of the target volume. In the activity signal a steep increase of the measured activity at the phantom entrance leads to a plateau AC0 after 3 cm, which continues until the begin of the target volume (14 cm). Directly behind the target volume (17 cm), the produced activity is zero. As expected, reaches the planned dose further (≈1cm) than the activation signal.

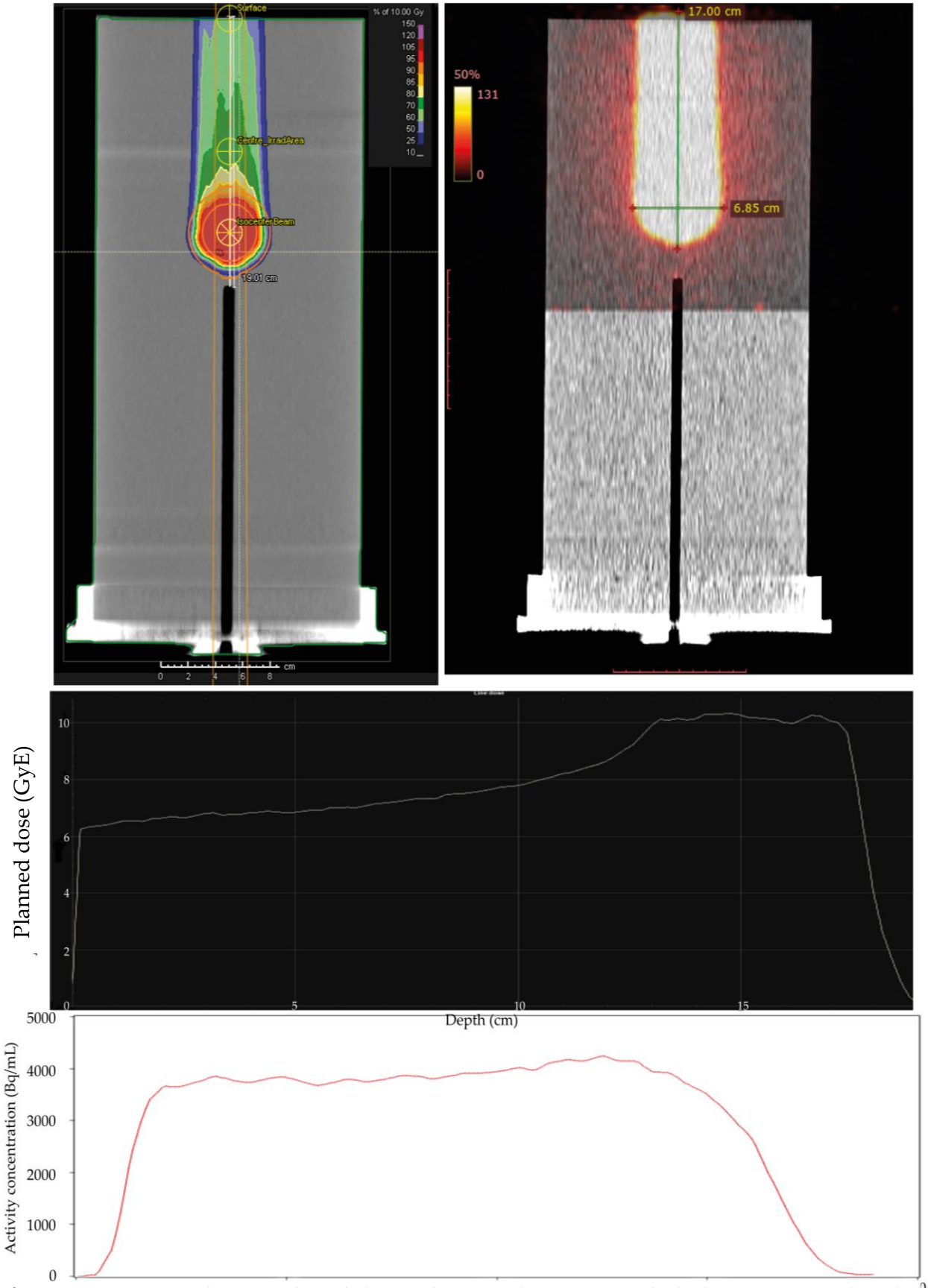

Figure 11; Comparison between planned dose and measured activation in high dose (10 GyE) polymethyl methacrylate (PMMA) experiment, coronal view. Upper left: treatment plan with planned dose (RaySearch). Upper right: non- attenuation and scatter corrected CT-scan, fused with the integral iterative PET-acquisition in default settings (Radiant). Middle: Planned dose delivery over phantom depth (RaySearch). Lower: Activation profile over dept (Vinci)

In Figure 12, the integral, iterative PET-reconstructions of the high dose PMMA experiment are visualised in all three dimensions. In beam direction, (upper image) a steep entrance activation is visible, with an approximate FWHM of 15 mm. The exit activation of approximately 30 mm FWHM shows a longer fall-off. The activation signal is slightly increasing over the length of the phantom. In the transversal and sagittal plane, similar activation fall-off is visible on the left- and the right side of the phantom, with an approximately FWHM of 15 mm.

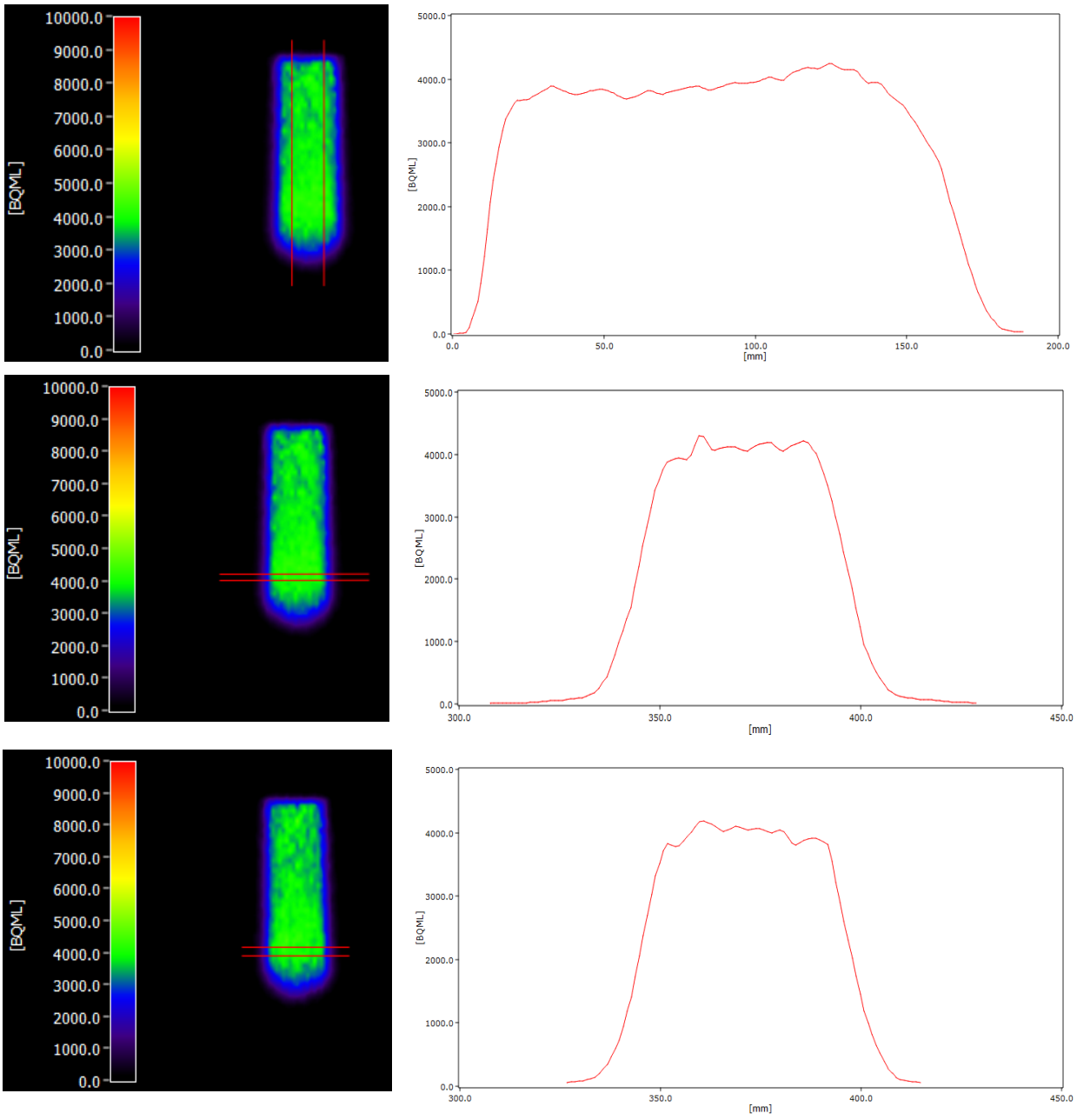

Figure 13; Activation profile (left) and graph (right) in integral iterative reconstruction of high dose PMMA experiment. Coronal dose profile (upper) transversal dose profile (middle) sagittal dose profile (down). Beam entrance is above. At the end of the activation signal, the sphere-shaped planned target volume can be seen. Scale shows activity concentration (Bq/mL) PMMA: polymethyl methacrylate.

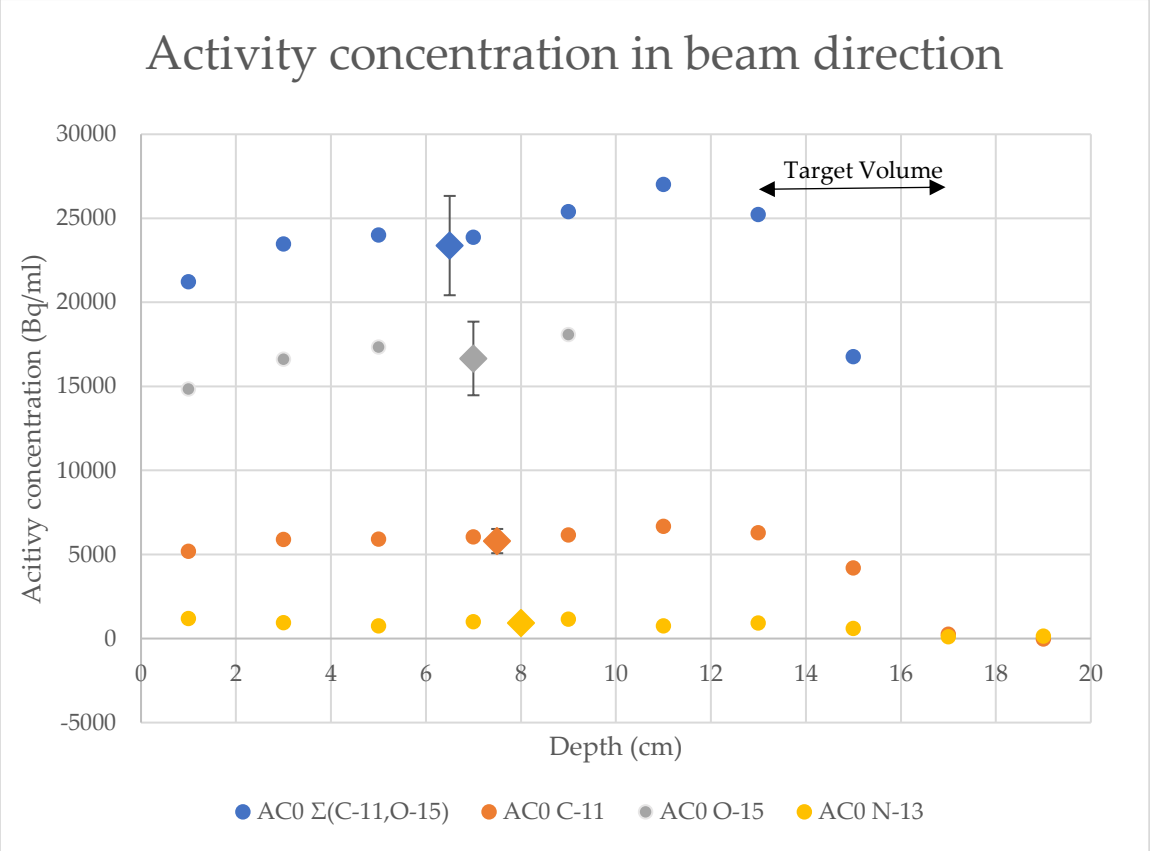

Figure 14; Estimated mean initial activity concentration in longitudinal direction of the PMMA phantom, retrieved in the high dose (10 GyE) experiment. Depth of 0 cm is the entrance of the beam in the phantom. Treatment plan was a 4 cm diameter sphere from 13 cm depth. The diamond point indicates the average value out of four similar VOIs. Error bars indicate one standard deviation. Average AC0 and the standard deviation are calculated from VOIs between 2 cm and 16 cm depth. Half of the data points are included to ensure independent data points. AC0: estimated initial mean activity concentration at t=0, at end of proton irradiation.

Figure 14 shows the AC0-profile of ^{11}C, ^{15}O and the sum of both in the direction of the beam. They show the same trend. The decrease in AC0 from the front of the target volume is visible. The ACs, measured at 18 and 19 cm depth, behind the target volume, are nearly zero, following the proton characteristics. At the phantom entrance, decreased AC0-values are visible, which is caused by partial positioning of the VOI outside the phantom, since no activation in air is detectable. The range from 1 cm till 17 cm, until the end of the target volume is analysed, see Table 16

An average summed AC0 of 22.9 kBq/mL is found with a standard deviation of 4.6 kBq/mL, resulting in a COV of 0.2. Although the standard deviation in the AC0 of O-15 is increased over the AC0 of C-11, is the COV similar. The largest contributor of the AC0, ^{15}O, shows a larger standard deviation, but no larger COV, compared to ^{11}C.

The ^{15}O: ^{11}C-ratio, visualised in Figure 15

Figure 15; ^{15O}: ^{11C} – ratio in longitudinal direction of the PMMA phantom in the high dose experiment. The diamond indicates the average value.

is minimal fluctuating over the depth of the phantom until the end of the target volume, at 17 cm depth. The standard deviation is 0.1 at a mean value of 2.9, resulting in the lowest COV of all measurements, 1.9 & 10^{-2}, see Table 16.

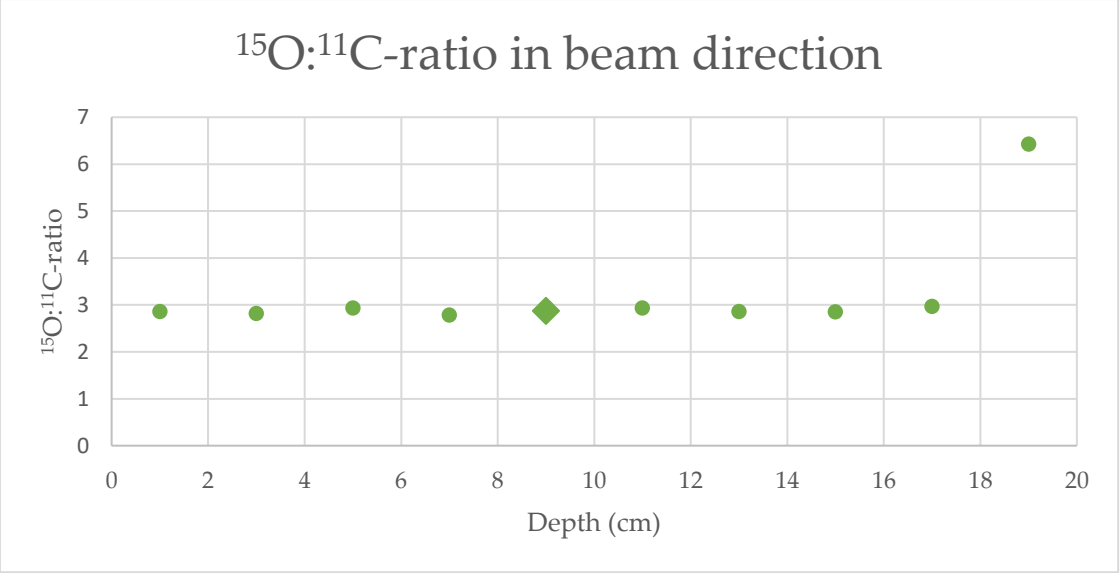

Figure 15; ^{15}O:^{11}C – ratio in longitudinal direction of the PMMA phantom in the high dose experiment. The diamond indicates the average value.

Table 16; Average, standard deviation and coefficient of variation values for activity concentration for mean activities measured in different depths of the phantom, one cm of the entrance and exit border of the phantom. AC0: estimated initial mean activity concentration. SD: standard deviation. COV: coefficient of variation.

	Average AC0 (kBq/mL)	**SD (kBq/mL)**	**COV (·10^{-1})**
∑(C-11, O-15)	23.4	3.0	1.26
^{11}C	5.8	0.7	1.24
^{15}O	16.7	2.2	1.31
^{13}N	0.9	0.2	2.09
^{15}O:^{11}C-ratio	2.9	0.1	0.19

5.2.5 VOI – size

Figure 16 and Figure 17 show the ^{15}O:^{11}C-ratio and the AC0-value for different VOI-sizes for the PMMA high dose experiments. The AC0 is decreased in small VOI-diameters up to 10 mm. The ^{15}O: ^{11}C-ratio is stable over the VOI-diameter with a mean and standard deviation of 2.9 ± 0.07. For the ^{15}O:^{11}C -ratio and the AC0, the standard deviation decreases for larger VOI-sizes. For VOI-diameters of at least 20 mm, the ^{15}O: ^{11}C standard deviation is smaller than 0.1

In the mean dose experiment, a similar trend is visible in ^{15}O:^{11}C -ratio and AC0-values, see Figure 18 and Figure 19. The standard deviation is increased over almost all observations, compared to the high dose experiment. The ^{15}O: ^{11}C-ratio saturates at larger VOI-size, namely between 20 and 30 mm diameter and shows a larger mean ± standard deviation of 3.5 ± 0.3

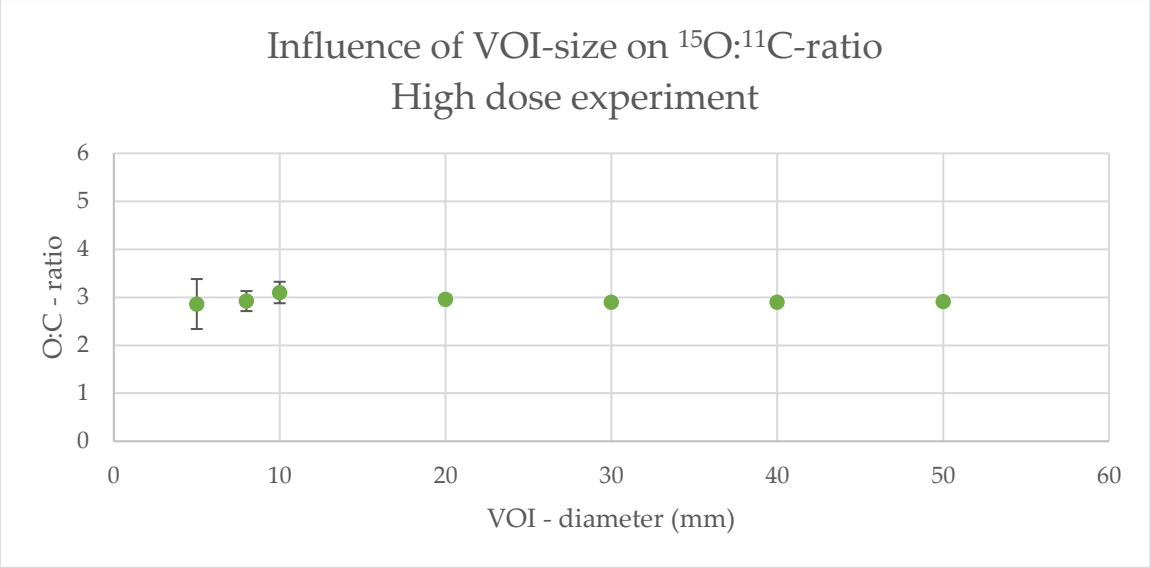

Figure 16; Influence of VOI-size on ^{15}O:^{11}C – ratio in high dose PMMA experiment. Every data point is an average of five VOI's on different depths in the phantom of which 30, 40 and 50 mm are partly overlapping. The diameter of the target volume was 30 mm.

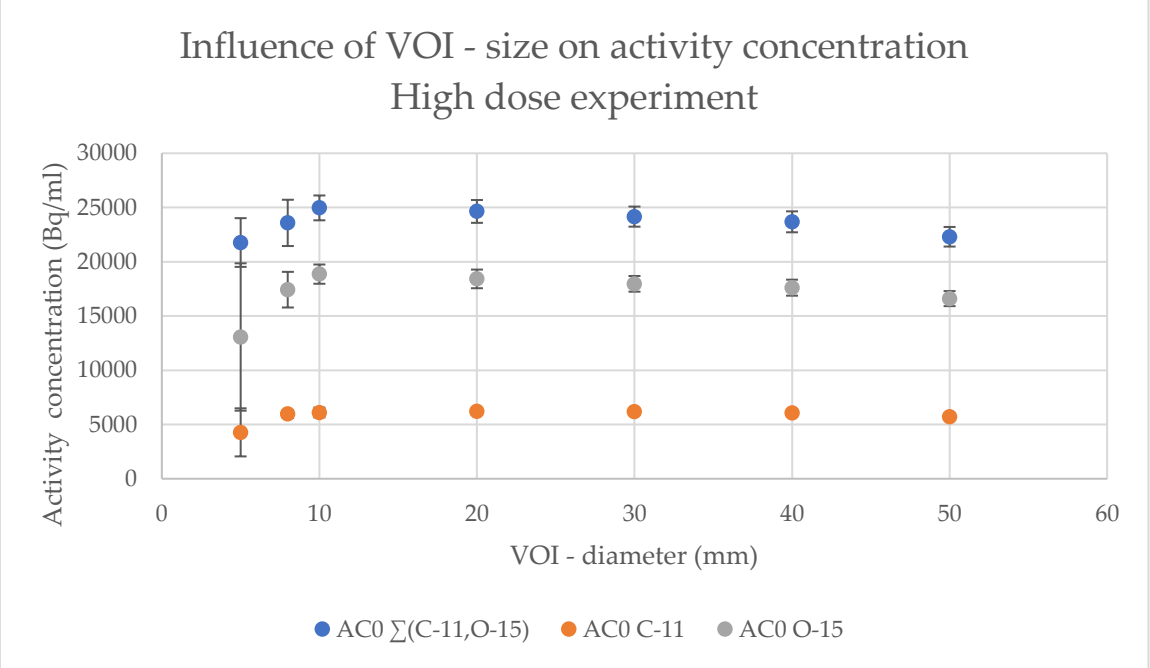

Figure 17; Influence of VOI-size on mean activity concentration in high dose PMMA experiment. Error bars indicate the standard deviation of the five repetitive VOIs. Every data point is an average of five VOI's on different depths in the phantom of which 30, 40 and 50 mm are partly overlapping. AC0: mean activity concentration at t=0, at end of proton irradiation.

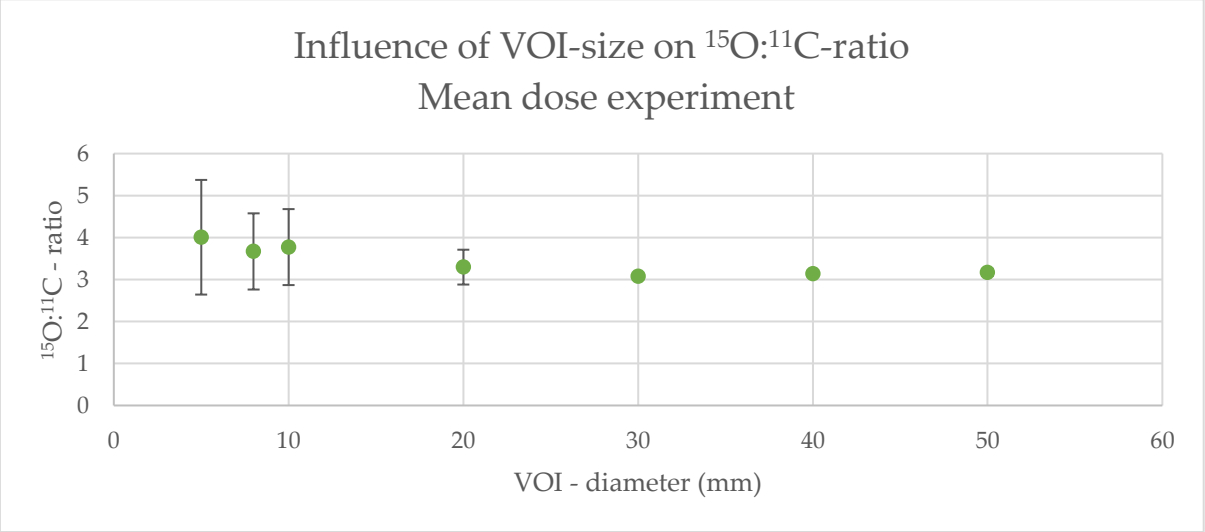

Figure 18; Influence of VOI-size on ^{15}O:^{11}C – ratio in mean dose PMMA experiment. Every data point is an average of the ^{15}O:^{11}C-ratio of five separate VOI's on different depths in the phantom. The VOIs of 30, 40 and 50 mm are partly overlapping. The diameter of the target volume was 30 mm.

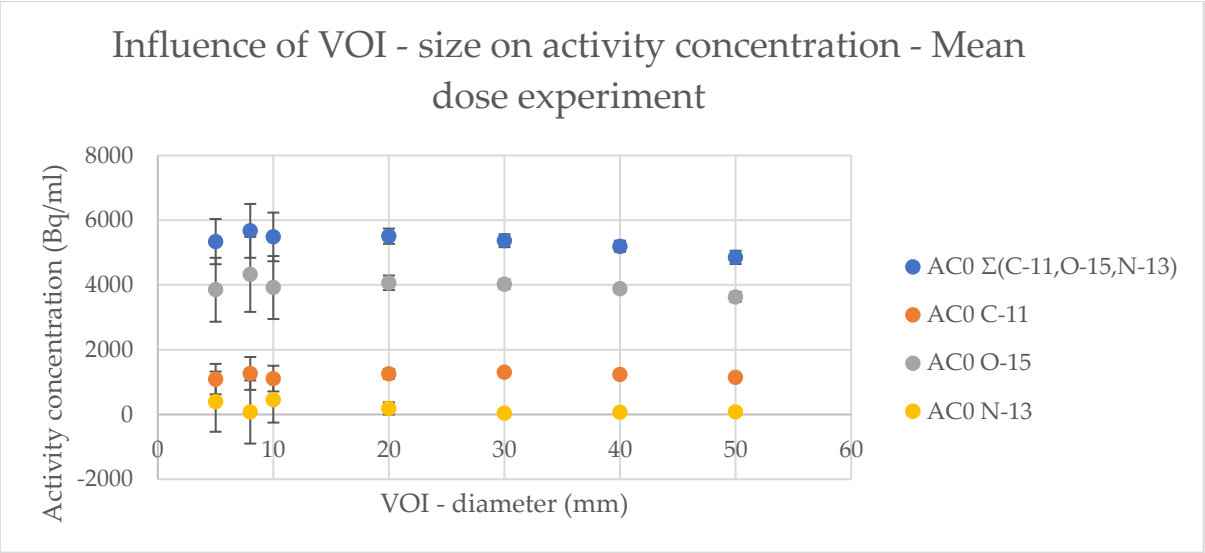

Figure 19; Influence of VOI-size on mean activity concentration in mean dose PMMA experiment. Error bars demonstrate the standard deviation of the five repetitive VOIs. Every data point is an average of five VOI's on different depths in the phantom of which 30, 40 and 50 mm are partly overlapping. The diameter of the target volume was 40 mm. The AC0 N-13 is neglectable. AC0: mean activity concentration at t=0, at end of proton irradiation.

5.3 Discussion model design

5.3.1 Reconstruction technique

Visually, the OSEM-image outperformed the FBP-image, due to the large amount of streak artefacts in the FBP-reconstructed image, caused by the low number of counts. These streak artefacts can be corrected for by using a low-pass filter, instead of the high pass Ramp filter, mostly applied in FBP. This low filter in the frequency domain, is applied to the Fourier transformed projection data to correct for and eliminate 1/r blurring, caused by the simple back projection. Examples of filters are the Hann-filter or the Shepp-Logan filter. [56, 57] Applying these signal-to-noise increasing filters means compromising on lower spatial resolution, since it diminishes higher frequencies in the images. This decrease in spatial resolution is not desired in this experimental setting, aiming to quantify the produced activity concentration.

The spatial resolution of the FBP reconstructed and the OSEM reconstructed image is similar. The spatial resolution of the OSEM reconstructed image can be improved by resolution modelling, as implemented in the used Siemens Biograph Horizon PET-scanner. Resolution modelling, also known as point spread function (PSF)-modelling, corrects for the degradation of the resolution, further away from the centre of the transaxial field of view (parallax effect), with the scanner-specific PSF. PSF-modelling decreases and improves heterogeneity of the spatial resolution in the transaxial field of view. Moreover, it improves the contrast to noise ratio. Therefore, the image quality of the image is increased, with higher detectability of small lesions. [58] It may, however, contribute to other undesired effects, since its correction is based on measured data with a $^{68}Ge/^{68}Ge$ point source. It is not known what the positron range correction effects is and moreover, the possible occurrence of Gibbs artefacts can influence both visual as quantitative analysis. [59] Although PSF-modelling has positive effect on the spatial resolution, is it not applied in our experiments, due to the described potentially undesirable effects.

Quantitatively, the FBP and the OSEM reconstructed images show similar activity concentration distribution. Moreover, no trend (i.e. no bias) is visible in the average activity concentrations for low-count time frames, which suggests that no truncation takes place for negative values, during the OSEM reconstruction process. The standard deviation is smaller for larger frame times, suggesting more accurate AC0 measurements in larger time frames.

Since the pilot-experiment encompasses irradiation of a two-dimensional circle, the measured AC0 in the spherical VOI is assumed lower than in the following experiments, irradiating a three-dimensional volume. All frame durations in the following experiments are considered longer than 5 seconds. Since all analyses will contain more data, it can be stated that no positive bias due to nonnegativity constraints will occur at the following reconstructions. Based on similar quantitative performance, but largely decreased image quality by the introduction of streak artefact in the FBP reconstructed images, OSEM reconstruction with time-of-flight modelling and without resolution modelling was used as the reconstruction method for future experiments.

5.3.2 Estimator selection

The 60 seconds time frame model showed the smallest standard deviation of the models which predicted the presence of the nuclides significantly correct. Since the two-nuclide model determines the significance presence of the nuclides correctly from time frames of 60 seconds, a time frame of at least 60 seconds is recommended. The time frame of 60 seconds is in accordance with other activation PET – studies. [42, 44]. The AIC-value of the three nuclide model is lower, without support to use the two nuclide model. Therefore, application of this model is indicated, despite the larger standard deviation for the three nuclide model. This model does not correct for other radionuclides as the three described. When large contributions of other radionuclides are expected, it should be tested whether adjustment of the model is required.

5.3.3 Activity concentration validation

Although the ^{11}C PE:PMMA-ratio of 1.1 is according expectation, the total produced activity is less than expected. A difference between our method and the method of Parodi et al. [42, 47] and Nishio et al. [46] is the used irradiation technique. Our experiments are performed by pencil beam scanning with a varying beam energy in 9 layers between 134 and 172 MeV, with a small increased beam energy for the high dose HDPE experiment, see **Table 10.** The experiments as described by Parodi et al. and Nishio et al. make use of a passive scattering beam with a constant initial energy of 191 MeV. Although pencil beam scanning is not associated with clinically meaningful reduced tissue dose by a comparing study in unresectable pancreatic cancer of Choung et al., the observed lower median dose and the described lower beam energy may explain the decreased amount of activation in our experiment. [60] This effect is, however, expected to be within the uncertainty in the treatment planning and therefore, not assumed the cause for the lower produced activity. The different energy range can also not explain the decreased amount of generated activity, since it would cause a inverse effect. A lower proton beam energy causes higher cross sections and therefore, more generated activity. The time delay can also not explain the decreased amount of activity, since the described studies of Parodi et al. and Nishio et al. are affected by similar decay, due to offline PET-acquisition, with an approximate time delay of respectively 20 and 2 minutes.

The amount of ^{15}O produced in the high dose PMMA experiment, which is three times larger than the amount of ^{11}C, deviates from the hypothesised ratio of 4.0. This ratio is two times larger than the found ^{15}O:^{11}C-ratio by in-beam PET-detection by Kraan et al., who uniformly irradiated a combined HDPE and PMMA-phantom with 130 MeV. [28].

5.3.4 Spatial distribution

Since the dose distribution follows the Bethe–Bloch equation (1) and the activation profile follows eq.(2) and (3), the observed differences are according expectation. No

ground truth of both variables is available. The planned dose, which is based on simulation, can be verified by measuring the dose with an ionisation chamber during irradiation. The measured activation signal can be verified by comparison with the simulated activation signal. The increased dose range, compared to the range of activation is characteristic are due to the reduced kinetic proton energy for elastic scattering, delivering dose, compared to the minima binding energy of the nuclei a target proton should overcome to cause nuclear fragmentation. When the incident proton energy is lower than this threshold energy, no positron emitting nuclei will be generated. The protons will, however, continue their movement through the tissue and will transpose the rest of their energy mainly by elastic and inelastic Coulomb scattering, without causing nuclear interactions.

The AC0-values show a large variability in beam direction (Figure 14), even when the entrance of the beam and the end of the target volume is excluded from analysis. This variability is not found in the ^{15}O:^{11}C -ratio (Figure 15), which is remarkable stable.

The deviation in AC-values might be caused by a measurement dependent noise, which contributes equally to ^{11}C and ^{15}O and is, therefore, cancelled out by calculating the ratio of the two. The presence of random noise, however, is, more likely. This noise, contributes to ^{11}C and ^{15}O independently and will therefore lead to an even larger variability. The variability might be caused by phantom heterogeneity, which is not expected, since the phantom is designed for the purpose of these experiments. It was not possible to find out the uncertainty in the phantom density.

A slow increase might be visible in the AC0 over the depth of the phantom, see Figure 14. This trend corresponds with results reported in literature. España et al., [38] and Horst et al. [37] reported an activation peak around 8 cm depth, which is, probably due to the lower proton beam energy (116 MeV), closer to the phantom entrance than in our experiments, where the peak is positioned around 12 cm. Cambraia Lopes et al. [61] and Kraan et al. [28] also showed a small increase in activity profile along the beam–axis in PMMA and PE with a 127 MeV and 130 MeV proton beam, respectively. The trend visible in the AC0 corresponds to both C11 and O15 and is thus not detectable in the ^{15}O:^{11}C -ratio. Therefore, for analysis of the ^{15}O:^{11}C-ratio, the VOI can be located in the activated volume till the end of the target volume. For AC0 interpretation purpose, exclusion of 1.5 cm from the entrance of the beam, 2 cm from the end of the target volume and 1.5 cm from the axial activity borders is advised. Moreover, a gradual increase of AC0 over the depth of the phantom should be considered.

5.3.5 VOI – size

The decreased AC0 values for small VOIs in the high dose experiment (Figure 17) is not observed in the mean dose experiment (Figure 19) and is therefore attributed to a negative bias by randomly inclusion of low AC0 voxels. The slight decrease in AC0-values for VOI-sizes of 40 mm diameter due to partial volume effects and inclusion of (near) zero-activity voxels can be noticed in both experiments.

The increased standard deviation in AC0 and ^{15}O:^{11}C-ratio for small VOI-sizes, compared to larger VOI-sizes is according expectations, due to a large influence of noise in the low count statistic data. To achieve an ^{15}O:^{11}C–ratio standard deviation below .1, VOIs of minimal 20 mm diameter are applied in the high dose experiment for VOIs of minimal 30 mm in the mean dose experiment for VOIs.

The ^{15}O:^{11}C-ratio is considered a more robust measure than the AC0-values for ^{15}O and ^{11}C, see Figure 16, corresponding with the results of the spatial distribution analysis. To obtain an accurate ^{15}O:^{11}C -ratio, with a standard deviation below 0.01 in clinical dose per fraction of 2GyE, a minimal VOI-diameter of 30 mm is required, corresponding to a volume of 14 mL.

5.4 Conclusion model selection

The model that predicted the presence of the three nuclides significantly, showed the smallest standard deviation in parameter estimation and had the lowest AIC-value, compared to the alternative model is the three nuclide model with time frames of 60 seconds. The AC0s for further analysis are estimated by NLS, based on the radionuclides, ^{11}C, ^{15}O and ^{13}N. Since the ^{15}O:^{11}C-ratio seems to be the most stable parameter for tissue composition, both in spatial analysis as in VOI-size, this ratio is used as leading parameter for the further analysis. The AC-values are analysed for additional information. The mean ^{15}O:^{11}C -ratio in the high dose PMMA – experiment is 2.9 with a standard deviation of 0.07.

The chosen reconstruction method is OSEM, due to its high signal-to-noise ratio and the absence of streak artefacts, compared to FBP. Time-of-flight reconstruction is applied for additional signal-to-noise increase. PSF-modelling is not applied to prevent additional artefacts, like Gibbs artefacts or incorrect positron range correction.

To analyse the AC0-values, the data is acquired from the reconstructed images from the 2GyE experiment, with spherical VOIs of 30 mm diameter, 14 mL. These VOIs should be positioned at least 15 mm of the entrance and 20 mm of the exit border of the target volume. To determine the ^{15}O:^{11}C -ratio, the VOI can be positioned in the activated volume between the entrance point and the end of target volume. Since no activation occurs behind the target volume, no aPET measurement should be performed behind this target volume. Exact localisation of the target volume in PET-acquisition may be difficult to obtain in clinical setting.

CHAPTER 6

Clinical parameters

6.1 Methods clinical parameters

The expected thresholds for the parameters are defined in CHAPTER 3.
All analyses are performed with the investigated model parameters as summarised in section Conclusion model selection. Based on the boundary restrictions of the phantom (minimal 15 mm distance from the entrance- and exit of the target volume).
and the recommended VOI-size of 30 mm diameter, in every analysis, four adjacent repetitive VOIs are drawn in beam direction in every dose and target volume experiment

6.1.1 Time delay

To determine the maximal time interval between end of PRT and start PET-acquisition where tissue decoupling is still possible multiple tissue decoupling analyses are performed with an increased amount of time delay before start of the PET-acquisition. Four non-overlapping VOIs of 30 mm diameter are drawn over de beam direction of the phantom in the mean dose PMMA experiment data. The ^{15}O: ^{11}C-ratio from earlier analysis in this dataset was 3.1 ±0 .07.
In every successive analysis, the consecutive time frame of 60 seconds is excluded from the analysis. The maximum time delay for aPET tissue decomposition is defined as the maximal delay time, before the standard deviation of the ^{15}O: ^{11}C – ratio deviates from its plateau value in the measured values in the earlier data points for more than 0.1.

6.1.2 Dose

In this analysis, the influence of the delivered dose on the estimated initial mean activity concentrations and its corresponding ^{15}O: ^{11}C -ratio is investigated. Data is obtained from the low dose (0.5GyE), mean dose (2GyE) and high dose (10GyE) PMMA experiments. Every experiment irradiated the mean target volume. In the analysis, the physical dose is used, which can be calculated by dividing the radiobiological dose by the 1.1 relative biological effectiveness of protons. A regression is performed of the estimated AC0 on the dose with ordinary least squares using Excel. The R^2-values are plotted to determine which fraction of the variance in AC0 can be explained by the dose.

6.1.3 Target Volume

In this analysis, the ^{15}O:^{11}C-ratio is compared for the experiments, where a small, medium and large target volume is irradiated, of 16, 34 and 298 mL, respectively. The centre of all target volumes is positioned at the same distance of the beam entrance. The minimal and mean target volume were created in the same treatment plan. The maximal target volume is created in a different treatment plan.

6.1.4 Tissue composition

In this analysis, the ^{15}O:^{11}C -ratio results of the Vmean@Dmean experiments are compared. These include the PMMA experiment and the three TMMs, i.e. muscle, cortical bone and Adipose tissue. Since the TMM slabs were only 1 cm thick, it was not possible to draw a spherical VOI of 30 mm diameter. Therefore, the VOI is deformed to maintain the total volume of 14 mL. In each tissue mimicking material, a cylindrical VOI is drawn of 42 mm diameter at the radial cylindrical side and 10 mm diameter parallel to the beam, with a distance of 1 cm of the entrance of the beam. A distance of more than 3 cm is left behind from the furthest exit point of the beam. The results are thus based on one VOI, in contrast to an average of VOIs in the other materials. Therefore, it was not possible to define the variability of the TMM ^{15}O:^{11}C -values. To approach the uncertainty in the ^{15}O:^{11}C-ratio for the TMMs, the COV, determined by the Vmean@Dmean experiment is used, according eq. (12). This COV represents the variability within one experiment and is therefore considered smaller than between experiments.

This COV-value is used for the two research objective comparisons; comparing the hypothesised ^{15}O: ^{11}C-ratio with the estimated value and comparing the estimated values of the different materials. To determine the distinguishability between adipose and muscle tissue with the described method, the null hypotheses is tested whether the estimated ^{15}O:^{11}C-ratio for adipose tissue differ with a 5% significance level of the estimated muscle ^{15}O:^{11}C-ratio. Additionally, the estimated ^{15}O: ^{11}C-ratio of muscle is compared with the 5% significance level of the estimated adipose tissue ^{15}O: ^{11}C-ratio.

6.2 Results clinical parameters

6.2.1 Time delay

The resulting ^{15}O: ^{11}C-ratio for every minute time delay is visualised in Figure 20. An increase in ^{15}O: ^{11}C-standard deviation is visible for larger longer time delay. The mean ^{15}O: ^{11}C-ratio looks stable until a time delay of 608 seconds, 10 minutes. Table 17 shows the mean ^{15}O: ^{11}C-ratio and standard deviation values for this interval. The mean and its standard deviation for the 608 second time delay is 3.0±0.7. The ^{15}O: ^{11}C standard deviation threshold of 0.1 is passed after a time delay of 308 seconds, i.e. 5 minutes and the threshold of 1.0 ^{15}O: ^{11}C standard deviation after 608 seconds, i.e. 10 minutes.

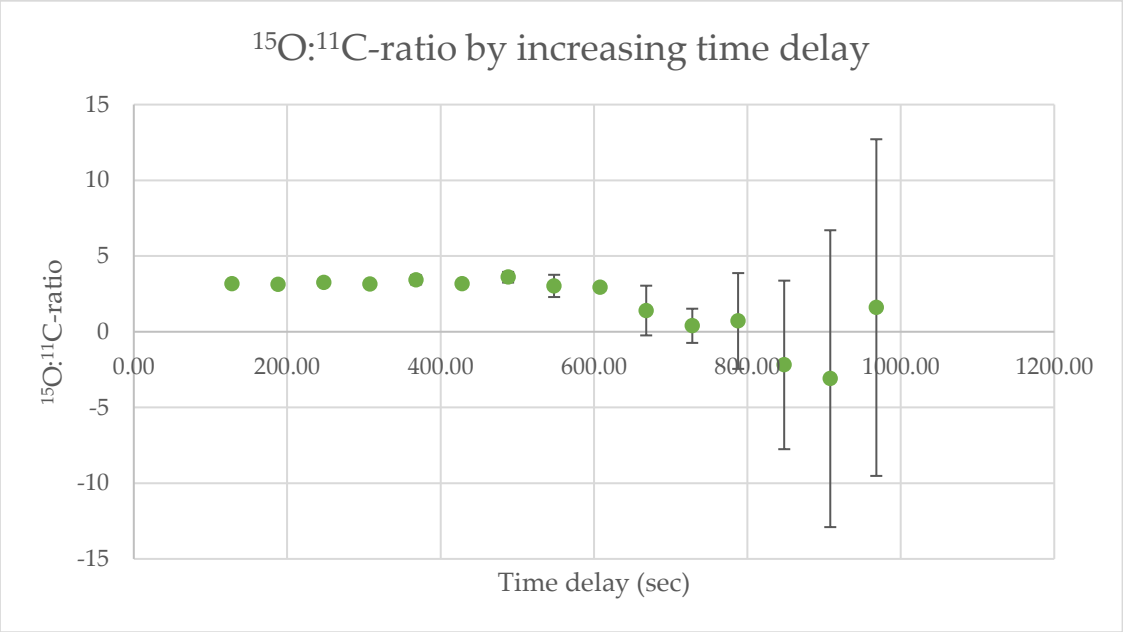

Figure 20; ^{15}O: ^{11}C–ratio for different time delays. Error bars indicate one standard deviation

Table 17; ^{15}O: ^{11}C – ratio for increasing time delay up to 10 minutes. Mean and standard deviation are calculated based on four not overlapping 30 mm diameter VOIs. SD: standard deviation.

Time delay (sec)	**Average ^{15}O: ^{11}C – ratio**	**Standard deviation**
128	3.16	0.05
188	3.13	0.09
248	3.25	0.02
308	**3.15**	**0.04**
368	**3.43**	**0.30**
428	3.17	0.14
548	3.60	0.35
608	3.03	0.73

6.2.2 Dose

Figure 21 shows a linear correlation for all radionuclides between physical dose and estimated initial mean activity concentration. The ^{15}O: ^{11}C-ratio is slightly decreasing in increasing dose with a decrease in variability, see Figure 22.

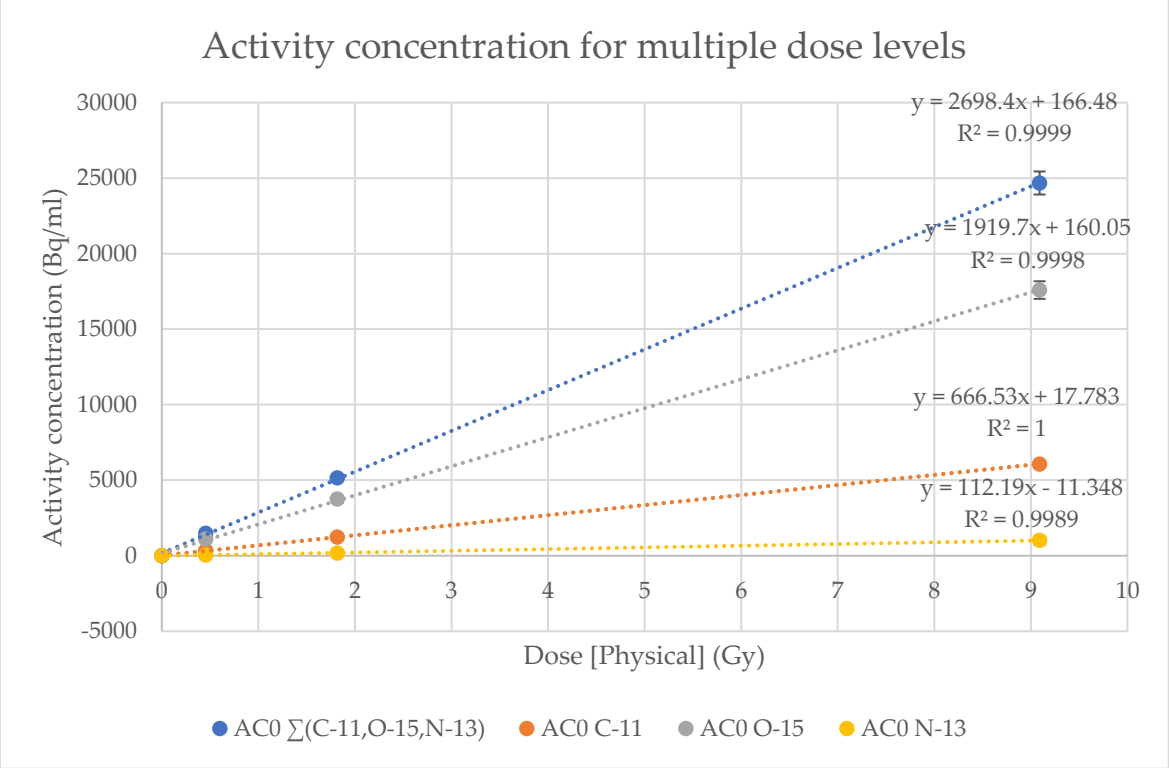

Figure 21; Estimated initial activity concentration for three different dose levels. AC0: mean activity concentration at t=0, end of proton irradiation.

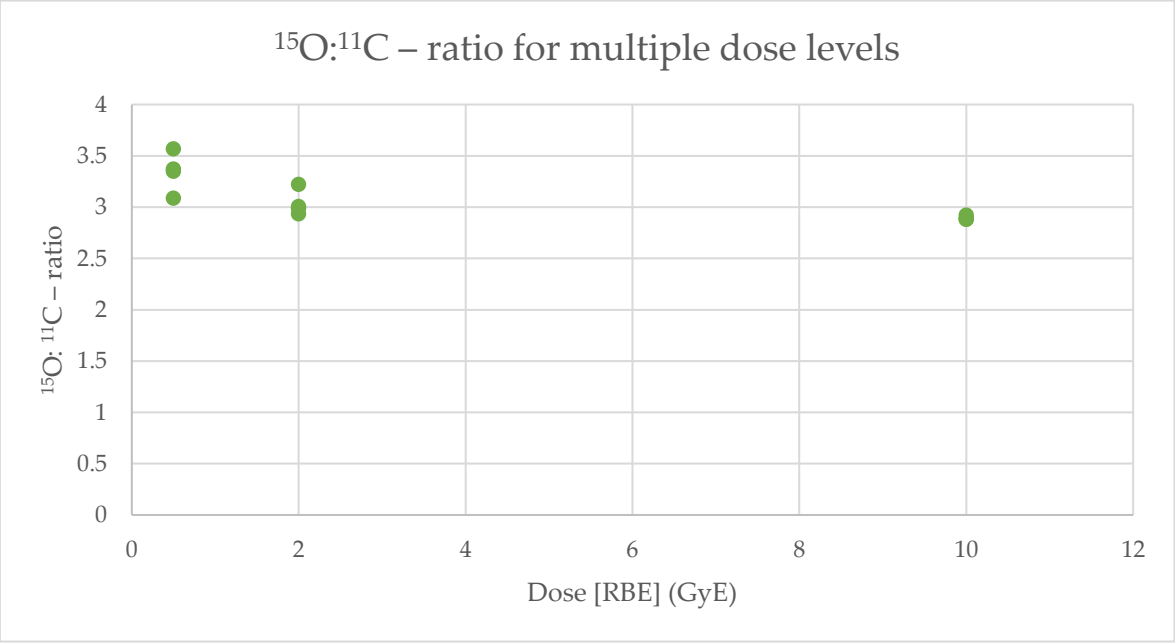

Figure 22; ^{15}O: ^{11}C – ratio for multiple dose levels. RBE: Relative biological effective

6.2.3 Target volume

The ^{15}O: ^{11}C – ratio, as visualised in Figure 23, for the maximal target volume is larger compared with the minimal and mean target volume ^{15}O: ^{11}C – ratio. In addition to the higher mean ^{15}O:^{11}C-ratio for higher target volume, the variation in ^{15}O:^{11}C -ratio is also increased for the larger target volume.

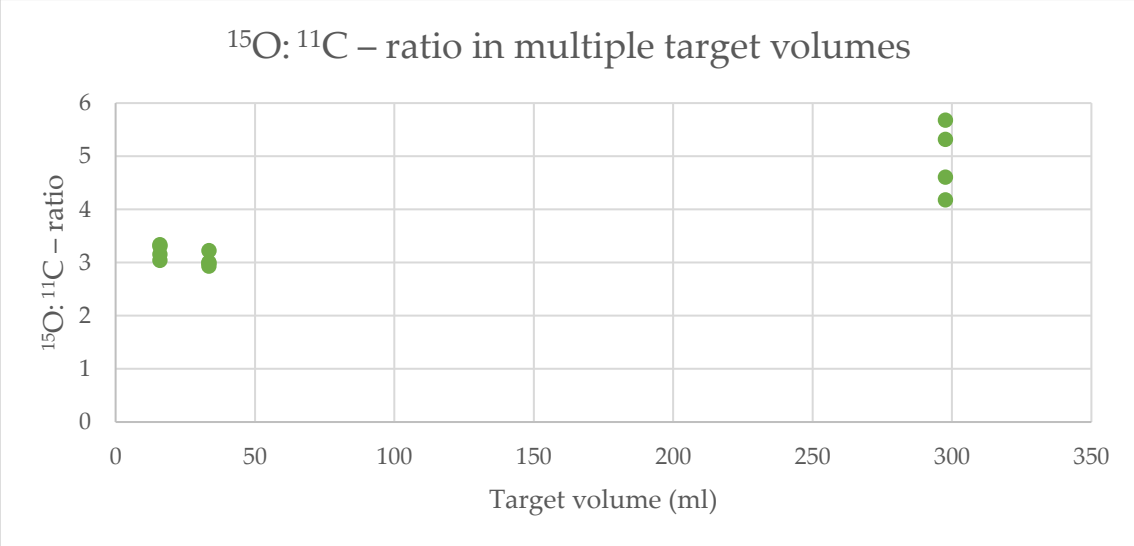

Figure 23; ^{15}O: ^{11}C – ratio in three different target volumes, Vmin, Vmean and Vmax, all irradiated with 2 GyE planned dose. Four VOIs are analysed per target volume.

6.2.4 Tissue composition

Table 18; All mean dose, mean volume experiments. Activation signal after irradiation of PMA three different tissue mimicking materials and the sum of these with their (±) one times standard deviation. This standard deviation only states the uncertainty of the model prediction. The hypothesised ^{15}O: ^{11}C – ratio is defined by eq. (2) and the estimated is from the model. CI is defined from SD. SD is calculated from the COV, determined in the Vmean@Dmean experiment, described in the first row. CI: 95% confidence interval. AC0: estimated initial mean activity concentration at t=0, at end of proton irradiation. SD: standard deviation COV: coefficient of variation

	Material	**Hypothesised ^{15}O: ^{11}C**	**Estimated ^{15}O: ^{11}C**	**CI estimated ^{15}O:^{11}C**	**AC0 ∑(^{11}C, ^{15}O, ^{13}N) (kBq/mL)**
TMM	PMMA	2.9	3.0 ±0.1	(2.82, 3.25)	5.2 ±0.2
	Muscle	2.0	1.9	(1.75, 2.01)	3.41 3.4 ±0.03
	Cortical Bone	9.7	7.1	(6.57, 7.57)	8.14 ±0.05
	Adipose Tissue	1.5	1.6	(1.48, 1.70)	2.68 ±0.05

The activation results of the irradiated phantoms are presented in Table **18**. The ^{15}O: ^{11}C-ratios range from 1.6 (adipose tissue) to 7.07 (cortical bone). The soft tissues muscle and adipose are more similar in hypothesised versus estimated ^{15}O: ^{11}C-ratio than the bone tissue. The differences between the hypothesises and the estimated value is 0.1 for the muscle and adipose tissue, 1.1 for PMMA and 2.6 for cortical bone.

6.3 Discussion clinical parameters

6.3.1 Time delay

aPET with 2GyE dose is feasible with 5 minute time delay with a maximal standard deviation of 0.1 in the ^{15}O: ^{11}C– ratio. In case of 10 minute time delay, the standard deviation in ^{15}O: ^{11}C-ratio is below 1.0. However, this time delay assumes all dose is delivery at once, at end of the treatment plan. Although in our experiments the maximal irradiation duration was only 40 seconds, clinical treatment plans in HNSCC can last up to 10 minutes. In pencil beam scanning, the target volume is irradiated spot by spot. In the first irradiated volumes, a larger time delay is present than in the later irradiated volumes, resulting in a lower amount of signal and increased complexity in the decoupling process, when the VOI encompasses different irradiated volumes at once. Moreover, deterioration of the signal, due to perfusion of the isotopes further decreases the quality of aPET. Earlier mentioned studies of Horst et al. [37] and España et al. [38], decoupled the measured activity concentrations in the contribution of the different nuclear reactions with a 15-minute time delay. The differences in results are probably thanks to the mono energetic beam as delivered in their experiments, in contrast with the contaminated time activity signal, retrieved from multi energy layer treatment plan irradiation in our experiments.

6.3.2 Dose

According to expectation, is an increase in delivered dose related to a higher AC0 (Figure 21)) and a more precise ^{15}O: ^{11}C-ratio (Figure 22). Although only four data points are available, indicates the high R^2 that the variation in AC0 is explained by the differences in dose. A linear correlation between the amount of delivered dose and the generated AC0 is present, indicating no change in energy layers in case of increased dose.

The decrease of 0.4 in average ^{15}O: ^{11}C–ratio between the 0.5 GyE experiment and the 10 GyE experiment cannot be explained by this higher proton fluence and/or longer irradiation time and might be considered within the uncertainty level, caused by the differences in treatment plans.

6.3.3 Target volume

The Vmin experiment does not show to be influenced by its small target volume, 15.9 mL, since its AC0-values correspond well with the Vmean target volume. The activated volume of 66.4 mL is more than four times the volume of the 14.3 mL VOI-size. Partial volume effects of the scanner are therefore not considered limiting in the amount of activation and the resulting ^{15}O: ^{11}C –ratio.

Figure 24; Activity concentrations in three different target volumes, Vmin, Vmean and Vmax. Irradiated with mean dose, 2Gy. AC0: mean activity concentration at t=0, at end of proton irradiation. Error bars indicate one standard deviation.

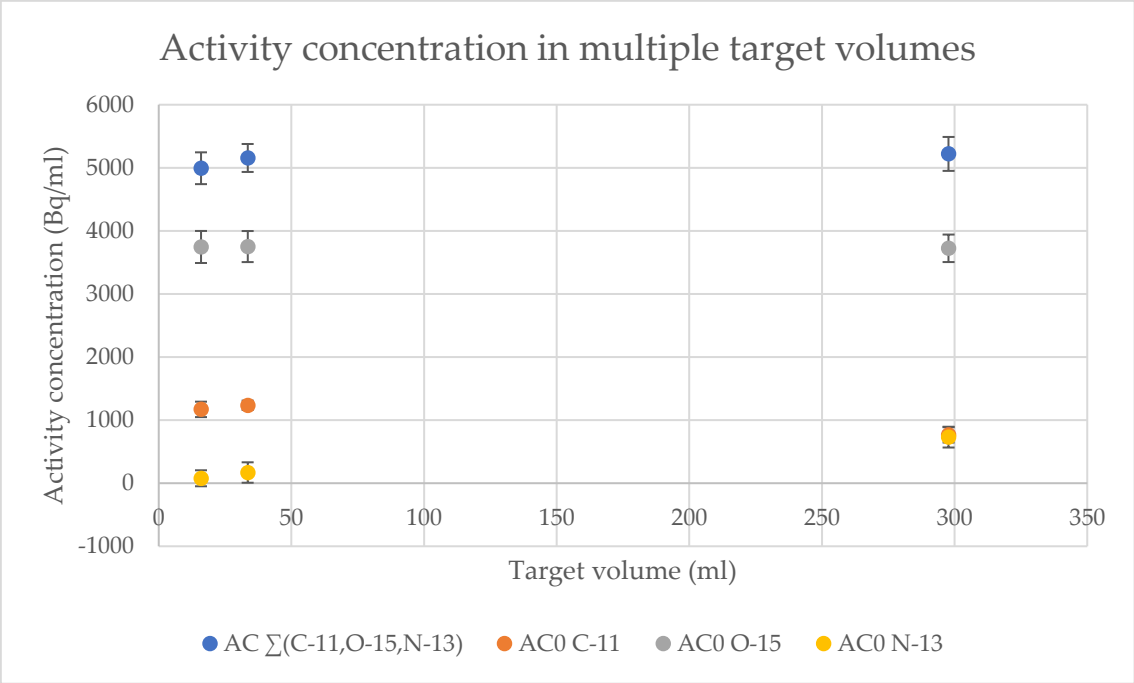

The increased ^{15}O: ^{11}C -ratio and variation of the Vmax experiment, compared to the Vmin and Vmean experiment is not according to expectation. When analysing the AC0-results, see Figure 24, the ^{15}O: ^{11}C -ratio decrease in the Vmax target volume is caused by a smaller contribution to ^{11}C, compared to the Vmin and Vmean target volume. This C-11 contribution looks to be designated to N-13 decay in the model, which has a larger half-life and thus a smaller decay constant. When analysing the TAC of the Vmax analysis, a reduced amount of measured activity in the time interval between 900 and 1440 seconds is noticeable, compared to expectation, see Figure 25. This effect, which cannot be physically explained by the decay of the radionuclides is only visible in the Vmax experiment and not in the Vmin and Vmean, experiment or in one of the other experiment analysis. Therefore, this effect is considered a reconstruction or measurement error.

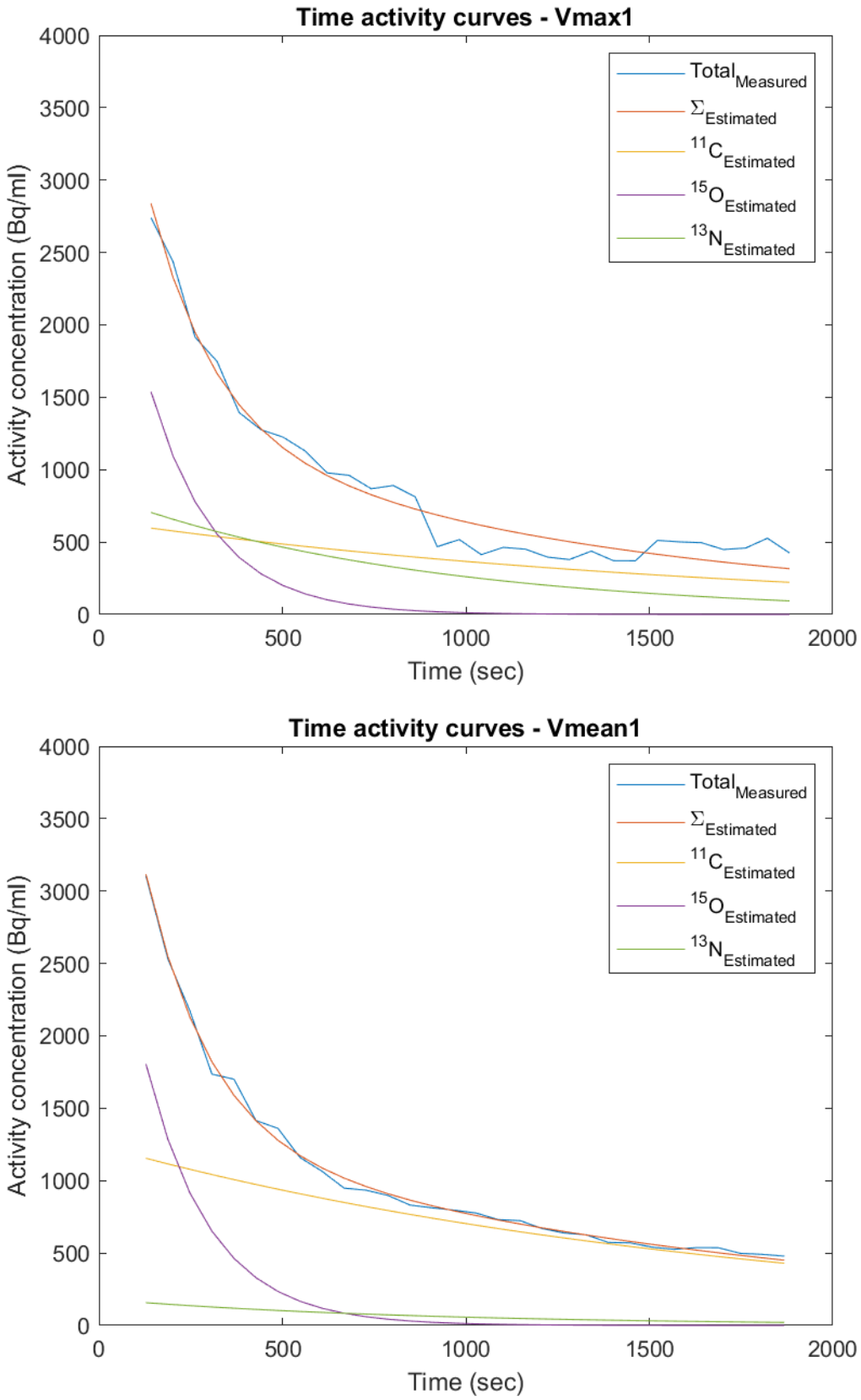

Figure 25; Measured and decopuled time-activity curve for the Vmax@Dmean experiment (upper) and the Vmean@Dmean experiment (bottom). The remarkable decreased amount of activity concentration between 900 and 1400 seconds is found in the time-acitivity curve of all four VOIs.

Measurement errors can be caused by the additional sources of activity, which may increase dead time. Background activity is generated by ^{176}Lu decay from the Lutetium oxyorthosilicate based detectors. A random count rate, caused by this ^{176}Lu decay of 500 to 1000 counts per second is reported, resulting in a factor 100 less true counts. [62] In radiopharmaceutical PET-scanning, this effect is neglectable. In the low count dynamic acquisitions, performed in this thesis, this may be a contributing factor. Other potential sources of external activity are contamination of the PMMA–material with other nuclides that become activated for positron decay. These factors are, however, unlikely to affect the data, since these effects would be present in all timeframes, while the observed effect only occurs between 900 and 1440 seconds and is thus time dependent. Explaining the time dependency, a change in the experimental set-up is expected. For example, moving a different radionuclide near the PET-scanner or moving the phantom at the beginning (900 sec) and the end (1440) sec of this time frame. Moreover, shielding of the detectors in this time interval may also cause this effect. As far as known, no changes in the experimental setup have occurred during the acquisition of this experiment.

The error might also be generated in the reconstruction phase. To find out whether the effect is caused by the iterative reconstruction process, the OSEM reconstructed data are recommended to be compared with FBP reconstructed data. To test the effect of the attenuation and / or scatter correction, reconstruction without attenuation and scatter correction should be performed.

When the error is not corrected for by altered reconstruction, it is recommended to repeat the measurement to check for measurement specific errors.

Besides the time dependent measurement error, might it be possible that another contribution of radionuclides is generated in the Vmax experiment. Although the treatment plans are optimised for the same criteria (Maximum dose, D98 and D99 ring) as described in section

Treatment plan, some differences in the treatment plans have occurred. Different parameters for spot size, dose rate and energy range are observed for the Vmin and Vmean treatment plan, compared with the Vmax treatment plan. The Vmax experiment shows a smaller spot spacing and an increased dose rate, both expecting to result in an increased total amount of activation, which cannot be found back in Figure 24.

The energy range of the beams also varies between the Vmin and Vmean and Vmax experiment. This is according to expectation, due to the different geometry of the target volume. Vmax is a cylinder in radial direction of the proton beam. The Vmin experiment is a small cylinder in parallel beam direction and the Vmean a sphere. The radius of the Vmax volume, the distance in beam direction, is larger than the distance in beam direction of the other target volumes, Vmin and Vmean. Since a larger beam depth is caused by a higher proton beam energy, a larger target volume in beam direction results in an increased energy range. This increased energy range, but in lower energy layers assumes more activation production, which is also not detectable in the results. The ^{15}O:^{11}C -ratio tends to become smaller in lower energies. This effect is, however, considered too small to explain the results found.

6.3.4 Tissue composition

The estimated ^{15}O:^{11}C -ratio seems to correspond well with the hypothesised ^{15}O:^{11}C -ratio in the soft tissues, adipose fat and muscle, with a difference of only 0.1 between hypothesised and estimated ^{15}O:^{11}C -ratio, see
Table **18**. The larger estimated ^{15}O:^{11}C -ratio reflects the higher contribution of 15O in the cortical bone mimicking tissue. However, the hypothesised ^{15}O:^{11}C -ratio was 2.6 higher than the estimated value. Two explanations can be given for this disagreement.

First, the large contribution of ^{40}Ca in the tissue (26.48 mass weight) influences the ^{15}O:^{11}C -ratio, see **Table 6**. ^{40}Ca can fragment in the following positron emitting radionuclides after proton irradiation: ^{38}K, ^{30}P, ^{15}O, ^{13}N, ^{11}C. ^{38}K, the main contributor, has a half-life of 7.636 min, approaching the half-life of ^{13}N (9.965 min). ^{30}P decays with a half-life of 2.498 min, quite similar to ^{15}O (2.037 min). [63] In the EXFOR database, only data from the cross section $^{40}Ca(p,2pn)^{38}K$ could be found, see Figure 26, with an approximate cross section of 0.04 b for 100 MeV incident energy. This nuclear reaction is expected to play a large role in the produced amount of activity. It depends on the model estimation, whether this observed activity is designated to ^{15}O or ^{13}N, but the reduced amount of ^{15}O estimated presumes the contribution towards ^{13}N. The other nuclear reactions, generating positron emitters will also influence the produced activity. Cross section data are however necessary to interpret the influence of these fragmentated radionuclides.

Addition of ^{38}K and / or ^{30}P in the parameter estimation of non-soft tissues might result in a more accurate AC0 estimation and therefore, ^{15}O:^{11}C -ratio. To test this, these two radionuclides should be independently added in the described model and tested for the model criteria as defined in model selection.

Based on the COV-derived confidence interval for the measurements, the hypothesised ^{15}O:^{11}C -ratio is within the estimated confidence interval for PMMA and the soft tissues, which indicates that this method is not rejected for further elemental tissue decomposition feasibility. For cortical bone, the hypothesised ^{15}O:^{11}C -ratio is out

of the confidence interval of the estimated ^{15}O:^{11}C -ratio, indicating that this model is rejected for aPET tissue decomposition with this hypothesis. Therefore, in non soft tissue components, the model needs to be adjusted before further feasibility studies can be performed. This hypothesises is an approximation, based on the median energy of the treatment plan.

Under the defined model and the assumption that the ^{15}O:^{11}C variability between experiments in different materials is similar with the ^{15}O:^{11}C variability within the PMMA experiment, aPET might be able in distinguishing adipose fat and muscle mimicking slabs with the characteristics as described in **Table 6**, when applying clinical treatment plans, optimised for similar dose and target volume.

The tissue mimicking materials are similar in density and electron density to the tissues they are mimicking. The ^{12}C, ^{16}O and ^{14}N mass percentages correspond within 15% difference, except for the mass percentage ^{12}C and ^{16}O in muscle mimicking material. These differ more than 50 percentage point from the real tissue values. The ^{15}O:^{11}C -ratio of muscle tissue is therefore expected to be much higher than measured and estimated in these phantoms, which would improve the distinguishability of the investigated materials using aPET.

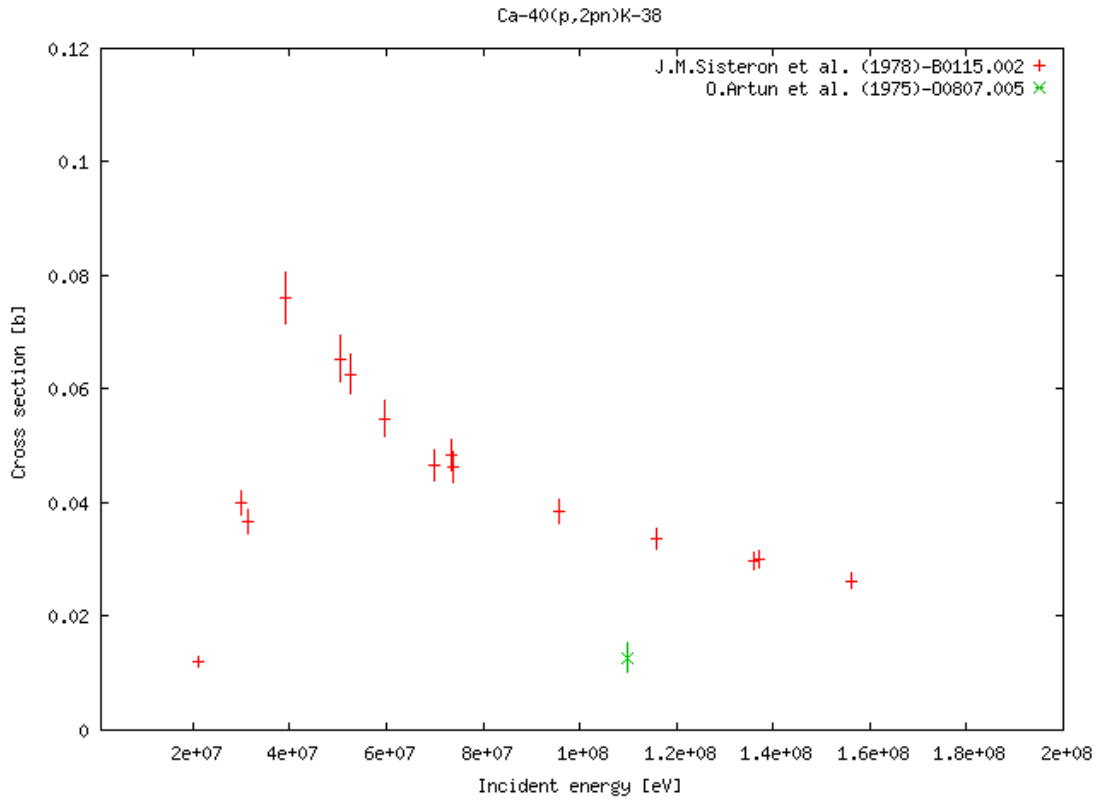

Figure 26; Cross sections of Calcium proton irradiation. Retrieved from [1]

CHAPTER 7

Clinical implementation

7.1 Translation towards clinical practice

7.1.1 Elemental tissue decomposition

Within the described method of aPET, spatial and temporal differences in radionuclide production can be defined. Determination of the actual element composition of the irradiated target volume can be done by simultaneously irradiating a phantom consisting of multiple components. Every component contains one activated element (^{12}C only part and a ^{16}O only part) and one component contains both nuclides (^{12}C and ^{16}O). This is described in the publications of Cho et al. [44] and Kraan et al. [28]. This experimental elemental decomposition can, however, not be performed in clinical irradiation. Elemental tissue composition can also be perceived by Monte Carlo simulation, based on experimental measured cross sections. Due to the high uncertainty in cross sectional data, Monte Carlo simulated activation data cannot be considered ground truth.

To validate aPET activity distribution results, the measured activity distribution is compared with the Monte Carlo simulated activity distribution.

In the method described in this thesis, the relative amount of ^{16}O can be compared within similar treatment plans. Performing aPET within the irradiated tissue of one fraction can provide spatial information about the relative amount of ^{16}O in the tissue. The minimal required VOI-volume of 14 mL is, however, large for identification of different oxygenation levels. Prerequisite is the use of the same treatment plan and no substantial anatomic changes during treatment.

7.1.2 Radiation induced biological effects

Analysing the relative contribution of ^{16}O with aPET after different fractions during the radiation treatment and thus with the same treatment plan can provide information about radiation induced tumour effects, such as necrosis, inflammation, oedema and hypoxia. [64]

Since tumour hypoxia reduces the effectiveness of the radiation treatment, it is desired to detect decreased oxygen levels in the tissue during radiation treatment. [25] By early detection of hypoxia, treatment planning adaption might be possible.

McKeown [65] reviewed the degree of oxygen (O_2) level reduction in several tumour sites and reported a median oxygen decrease of 4.6% in 592 analysed tumours. This decrease from 5.9 to 1.3% is found by Vaupel et al. [66], acquired with the minimal invasive Eppendorf pO2 histography. The largest contributor of the element ^{16}O in tissues is water (H_2O). The presence of water in tissue differs, just as the amount of oxygen, for healthy tissue compared to tumorous tissue. Barroso et al. found a decrease in water concentration over about 5 mm tumour border from 76 ± 8% (tumour) to 54% ± 24% (healthy tissue) in 20 oral cavity squamous cell carcinomas. [67]

Multiple *in vivo* techniques are proposed for hypoxia analysis, as clearly outlined in the review of Colliez et al. [68] These methods include invasive methods such as polarographic electrodes, which are not able to map the hypoxia of the whole tumour as required for dose painting purpose. Hypoxia can also be defined by PET-imaging, which administration of a hypoxia radiopharmaceutical, such as [18F]-fluoromisonidazole (FMISO) (first generation), [18F]flortanidazole (HX4) (second generation) and [18F]-fluoroazomycinarabinoside (FAZA) (third generation hypoxia radiopharmaceuticals). [69]
Activation PET is advantageous for its non-invasiveness and because it does not require the administration of radiopharmaceuticals, compared to a conventional PET-scan or a diagnostic quality CT-scan. When the treatment planning CT, which is of diagnostic quality, can be used for attenuation correction, the patient is not exposed to any additional, although limited, radiation dose of an additional CT-scan. Matching of this CT-scan with the PET-acquisition is, however, technically complicated, since spatial misalignment is inherently present and should be mitigated. More information about methods to achieve this alignment, can be found in paragraph 'Patient alignment' in **APPENDIX B.**

Furthermore, the relatively long acquisition time of the offline PET-acquisition (30 minutes) and the logistic challenges limit the application of activation PET.

Since oxygen differences between tumour and healthy tissue are around 4.6% and water differences around 22% with a tumour water composition of 76% and aPET cannot determine the molecule encompassing the ^{16}O element, the decrease in oxygen levels is considered not differentiable between the water concentration range in the tumour.

An alternative possible non-invasive method for determination of tumour hypoxia is MRI-sequences, e.g. T2*MRI, although this technique requires additional validation. [70]

7.1.3 Perfusion effect

In clinical application, inevitable biological wash out will occur, decreasing the amount of radionuclide detected and therefore, the quality of the aPET procedure. The amount of washout depends on the perfusion of the tissue. Bone and adipose tissue show smaller biological decay constants than better perfused muscle and brain tissue. [47] Tissue can be divided in fast, medium and slow components, dependent on their biological decay constants. Fast components are caused by fast blood flow, medium components by microcirculation and slow components by trapping of the radionuclides in molecules. The washout effects also differ per radionuclides, for example by the size of the radionuclide. [71] Models to correct for the biological wash out are described by Ammar et al. [72], based on proton irradiation of mice.

7.1.4 Tissue characteristics

Human tissue has a much higher contribution of ^{16}O (**Table 1**), compared to the investigated phantoms (**Table 6**), resulting in higher ^{15}O:^{11}C-ratios, when irradiating and

analysing according our experiment. In clinical setting, the tumour is more heterogeneous than the target volumes in the measured phantoms. Therefore, averaging of multiple VOIs is not possible. Heterogeneity within one VOI is also possible, which complicates the aPET decomposition. Estimating the parameters from a signal composed from multiple types of tissues will provide a different combined ^{15}O:^{11}C–ratio than the two tissue specific ^{15}O:^{11}C-ratios. Moreover, the elemental composition of different tissues vary strongly between human.

7.1.5 Treatment plan delivery

HNSCC treatment plans are delivered by four beams, subsequently irradiating the target volume from different angles. The activation of re-irradiated volume, with a different proton energy, disturbs the original decay process, which is required for decomposition and complicates estimation of the parameters.

Since the irradiated area is mostly not located directly on the surface, the beam travels through other types of tissue, before irradiation and the type of tissue in the beam. In the spatial distribution analysis in this thesis, the amount of activation did not seem to be spatial dependent. This spatial dependency will, however, occur in case of different densities and element compositions of the irradiated volume. Therefore, positioning of the target volume needs to be done accurately. Although the treatment plan is optimised on a certain delivered dose in the treatment plan, the treatment plan characteristics like energy level and spot spacing may differ from our measurements, when the beam has to travel through other tissues before reaching the target volume.

7.1.6 Parametric imaging

Since tissue decomposition for a certain volume, in clinical HNSCC irradiation, requires one ^{15}O:^{11}C-value, without the option to average over multiple VOIs, the variation over the ^{15}O:^{11}C-ratio needs to be minimal. The standard deviation of 0.07 is obtained in a VOI-size of 14 mL. This volume is considered too large for parametric imaging purpose, as well as for dose painting application.

7.2 Clinical implementation

The primary aim of proton therapy is and should always be accurate dose delivery and the application of aPET must be a secondary aim within the defined clinical treatment plans. In current clinical HNSCC irradiation setting, aPET quality is too low for clinical feasibility. This quality may increase by decreased time delay, decreased treatment duration or increase in the delivered dose. As long as the whole VOI is positioned within the target volume and 1.5 cm of the border, increase of the target volume would not influence aPET quality, assuming constant proton beam energy.

To improve the resolution limitations in the aPET tissue decomposition technique, PSF-modelling might help. Therefore, an analysis is advised to study the occurrence of Gibbs artefacts and positron range corrections. The effect of Gibbs artefacts can be studied by drawing line activation profiles over the radial and longitudinal direction of target volumes of different sizes. These effects mainly occur by small target volumes.

Decreased time delay is achieved by measuring activation online, i.e. during irradiation. The amount of signal that can be detected is higher in in-beam PET-acquisition, because there is no delay between irradiation and PET-acquisition. Therefore, the detection of short decaying radionuclides, for example ^{10}C, with a half-life of 19 seconds would be possible with online PET. [28] The expected contribution of ^{10}C is expected to be around half of the ^{11}C contribution. [61] For in-beam detection, a PET-detector ring needs to be placed in the treatment gantry. The geometrical interference of the PET-detector ring and the pencil beam nozzle hinders beam delivery and asks for compromises in PET-acquisition quality. The addition of a radionuclide, in this case ^{10}C, in the decomposition model might decrease its effectiveness. Therefore, the analysis of the model, as described in section b) Model should be repeated for these radionuclides.

Reduction of irradiation duration per fraction is desirable for decreased risk of treatment uncertainties, such as patient motion and results in increased aPET quality. Moreover, it has a beneficial effect on patient comfort and treatment costs. Shortened delivery time can be achieved by reduction of the number of energy layers. Van de Water et al. showed up to 45% reduction of the number of energy layers, resulting in a time reduction between 25 and 38% in three oropharyngeal cancers. [73]

The optimal amount of total delivered dose and whole treatment duration is being investigated, resulting in altered treatment plans. The MARCH meta-analysis of Bourhis et al. [74], updated by Lacas et al. [75], showed improved overall survival for the hyperfractionated radiotherapy arm with a hazard ratio of 0.83 (0.74-0.92) over a conventional radiotherapy scheme (66-70 GyE in 2 GyE fractions, 5 fractions a week) in HNSCC patients. Hypofractionating, delivery of a larger dose per fraction (up to 8 GyE per fraction), in less fractions is currently mainly applied in treatment with palliative intent. Thanks to its benefits in patient comfort, cost-effectiveness and increased radiobiological effectiveness, fractionated proton therapy in curative intent is also beneficial, especially in case of stereotactic body proton therapy. [76] The clinical feasibility of stereotactic body proton therapy is up till now studied in non-small cell lung cancer [77] and pancreatic cancer [78]. Different treatment schedules influence the quality of aPET. Higher dose deposit per fraction increases aPET quality, especially by minimal increase of delivery time, resulting in increased dose rate (monitor units per fraction).

Extremely high dose rates (< 40 Gy/s) are achieved in the application of "FLASH" proton radiation therapy. FLASH-proton therapy is promising in minimizing healthy tissue toxicity, while maintaining tumour control probability. However, the integration of FLASH-irradiation in conventional proton therapy treatment planning and pencil beam scanning gantries is difficult to integrate and not applicable yet. The most optimal spatial, temporal and dosimetric parameters still need to be defined. [79] In the treatment planning study of Van de Water et al. in four HNC patients, achievement of the high dose rates only seemed possible with hypofractionation and adapted treatment planning methods (arc-shoot-through planning). This adapted treatment planning results in increased integral dose with the risk of higher healthy tissue toxicity. [80] With the extremely low dose delivery time (milliseconds), compared with the high amount of dose delivered per fraction (~2-18 GyE), creates the future application of FLASH-proton therapy the ideal conditions for aPET elemental tissue decomposition. [79]

7.3 Limitations

Several limitations can be addressed to the experimental setup and the assumptions in this thesis.

7.3.1 Hypotheses definition

Although the cross section for the $^{16}O(p,3p3n)^{11}C$ nuclear reaction is approximately 5 times smaller than the main $^{16}O(p,pn)^{15}O$ reaction, this ^{11}C generating reaction cannot be neglected in tissues high in ^{16}O weight percentage, for example bone tissue. Adding these cross sections on the hypothesised ^{15}O:^{11}C–ratio leads to a more complex, but more representative hypothesis. For setting a more accurate hypothesis regarding the ^{15}O:^{11}C-ratio, simulation of the multiple energy layers should be performed.

7.3.2 Model selection

The proposed model seems to facilitate aPET tissue decomposition in soft tissues. There are, however, some limitations.

First, the three nuclide model is chosen, since the AIC-value did not support usage of the two nuclide model for the 60 second time frames. However, this model shows a three times larger standard deviation than the two nuclide model. This large standard deviation is not desired, since it requires a large VOI. This When applying a model, resulting in a lower ^{15}O:^{11}C-ratio standard deviation, a smaller VOI-size can be used, which makes spatial elemental tissue decomposition more feasible.

Second, NLS violates the non-negativity constraint that counting data has. This non-negativity constraint occurs for small $A(t)$ with large variation and might cause a bias in $\widehat{\boldsymbol{\beta}}$. In case of larger t, where $A(t)$ is close to zero, the assumption of a normal distribution might be violated, resulting in a bias. Studying and adjusting the probability density function of $A(t)$, for example by repetitive measurements, can improve the model accuracy. Due to logistic limitations, like costs of the experiments, limited availability of employees and reduction of radiation exposure, the experiments could not be repeated in this thesis.

The selection of the model is based on data of two experiments. To validate the model, application of the model on another dataset, including more experiments and different phantoms, is required.

7.3.3 Analysis

The spherical shape of the used target volume, influences the AC0 measurements in depth. The FWHM is influenced by decreased activation near the edges of the spherical volume. Therefore, the large FWHM mentioned is not only physically caused by the limitations of the beam and the PET, but also by the design of the treatment plan. Moreover, the 25 mm width of the longitudinal activity profile is influenced by the spherical shape of the target volume. For the purpose of analysing the activity profile, irradiation of a flat–shaped target volume perpendicular on the beam-axis, for example a cuboid, would be more exact.

7.3.4 Interpretation

To approximate the variability of the TMM ^{15}O:^{11}C -ratio, the variance within the PMMA experiment is used. However, a variability between experiments is always present. Additionally, although both experiments irradiated a similar volume (33.5mL) with a similar dose (2GyE), the treatment plans are different in number of energy layers and monitor units, see **Table 10**. The mean value used in the TMMs for standard deviation calculation using the COV is based on only one observation.

Variability calculation of the noncentral correlated ratio of the two AC0-ratios for C11 and O15 can be performed by the described method of Hayya et al. [81] However, this method only encompasses the uncertainty in the parameter estimation.

Therefore, the most robust method to determine the distribution of the ^{15}O:^{11}C -ratio is by repeating measurements.

7.4 Conclusion

aPET is under current clinical circumstances not feasible for determination of the relative ^{16}O amount in tissue. The minimum time delay in offline PET makes application of aPET impossible in current treatment delivery of around 10 minutes, especially considered the presence of biological wash-out in living tissue. The minimal VOI-size of 14 mL complicates spatial analysis of the relative ^{16}O amount in the target volume.

Upcoming proton therapy techniques, such as in-beam detection, hypofractionation and FLASH-irradiation may lead to higher aPET quality, which may overcome the time delay, creating options for future aPET application.

REFERENCES

1. (JCPRG), H.U.N.R.D.C., *Experimental Nuclear Reaction Database (EXFOR)* B. Pritychenko, Editor. 2019, National Nuclear Data Center (NNDC).
2. Vriens, D. and M. Van Vulpen, *Protonentherapie en multimodale beeldvorming.* TvNG, 2019. **2019**(04): p. 2316-2325.
3. Ferlay, J., et al., *Estimating the global cancer incidence and mortality in 2018: GLOBOCAN sources and methods.* Int J Cancer, 2019. **144**(8): p. 1941-1953.
4. Vigneswaran, N. and M.D. Williams, *Epidemiologic trends in head and neck cancer and aids in diagnosis.* Oral Maxillofac Surg Clin North Am, 2014. **26**(2): p. 123-41.
5. Lubin, J.H., et al., *Total exposure and exposure rate effects for alcohol and smoking and risk of head and neck cancer: a pooled analysis of case-control studies.* Am J Epidemiol, 2009. **170**(8): p. 937-47.
6. Stewart, B.W. and C.P. Wild, *World Cancer Report 2014*, I.A.f.R.o. Cancer, Editor. 2014, World Health Organisation: Lyon.
7. Marur, S. and A.A. Forastiere, *Head and Neck Squamous Cell Carcinoma: Update on Epidemiology, Diagnosis, and Treatment.* Mayo Clin Proc, 2016. **91**(3): p. 386-96.
8. Jolly, S., et al., *Postoperative radiation therapy in the management of head and neck cancer.* UpToDate, 2019.
9. De Felice, F., et al., *Radiotherapy Controversies and Prospective in Head and Neck Cancer: A Literature-Based Critical Review.* Neoplasia, 2018. **20**(3): p. 227-232.
10. Rambeau, A., et al., *Impact of locoregional irradiation in patients with upfront metastatic head and neck squamous cell carcinoma.* Oral Oncol, 2019. **93**: p. 46-51.
11. De Ruysscher, D., et al., *Radiotherapy toxicity.* Nat Rev Dis Primers, 2019. **5**(1): p. 13.
12. (LPPT);, L.P.P. and L.P.R.H.-h. (LPRHHT), *Landelijk Indicatieprotocol Protonentherapie Hoofd-hals tumoren*. 2019.
13. Mendenhall, W.M., et al., *Radiation Oncology for Head and Neck Cancer: Current Standards and Future Changes.* Oral Maxillofac Surg Clin North Am, 2019. **31**(1): p. 31-38.
14. van der Laan, B.F., et al., *Radiation-induced tumours of the head and neck.* J Laryngol Otol, 1995. **109**(4): p. 346-9.
15. Kim, J.K., et al., *Proton Therapy for Head and Neck Cancer.* Current Treatment Options in Oncology, 2018. **19**(6).
16. Newhauser, W.D. and R. Zhang, *The physics of proton therapy.* Phys Med Biol, 2015. **60**(8): p. R155-209.
17. Yoon, M., et al., *Radiation-induced cancers from modern radiotherapy techniques: intensity-modulated radiotherapy versus proton therapy.* Int J Radiat Oncol Biol Phys, 2010. **77**(5): p. 1477-85.
18. Wang, L., et al., *Proton versus photon radiation-induced cell death in head and neck cancer cells.* Head Neck, 2019. **41**(1): p. 46-55.
19. Liao, L., G.J. Lim, and X. Zhang, *A Molecular Dynamics Approach for Optimizing Beam Intensities in IMPT Treatment Planning.* Journal of Applied Mathematics and Physics, 2019. **07**(09): p. 18.
20. Ligtenberg, G., P.C. Staal, and S. Kleijnen, *Protonentherapie*, W.a.S. Ministry of Health, Editor. 2009, College voor zorgverzekeringen: Diemen. p. 1-25.
21. Ligtenberg, G. and P.C. Staal, *Protonentherapie bij model-based indicaties (hoofdhalstumoren, mammacarcinoom, longcarcinoom en prostaatcarcinoom) en bij overige indicaties*, W.a.S. Ministry of Health, Editor. 2011, College voor zorgverzekeringen: Diemen. p. 1-63.

22. Parodi, K., T. Bortfeld, and T. Haberer, *Comparison between in-beam and offline positron emission tomography imaging of proton and carbon ion therapeutic irradiation at synchrotron- and cyclotron-based facilities.* Int J Radiat Oncol Biol Phys, 2008. **71**(3): p. 945-56.
23. Frey, K., et al., *TPS(PET)-A TPS-based approach for in vivo dose verification with PET in proton therapy.* Phys Med Biol, 2014. **59**(1): p. 1-21.
24. Zhang, J., et al., *Evaluation of Proton Therapy Accuracy Using a PMMA Phantom and PET Prediction Module.* Front Oncol, 2018. **8**: p. 523.
25. Gray, L.H., et al., *The concentration of oxygen dissolved in tissues at the time of irradiation as a factor in radiotherapy.* Br J Radiol, 1953. **26**(312): p. 638-48.
26. Miyatake, A., et al., *Measurement and verification of positron emitter nuclei generated at each treatment site by target nuclear fragment reactions in proton therapy.* Med Phys, 2010. **37**(8): p. 4445-55.
27. Cho, J., et al., *Feasibility study of using fall-off gradients of early and late PET scans for proton range verification.* Med Phys, 2017. **44**(5): p. 1734-1746.
28. Kraan, A.C., et al., *Analysis of in-beam PET time-profiles in proton therapy.* Journal of Instrumentation, 2019. **14**(02): p. C02001-C02001.
29. Grimes, D.R., D.R. Warren, and M. Partridge, *An approximate analytical solution of the Bethe equation for charged particles in the radiotherapeutic energy range.* Sci Rep, 2017. **7**(1): p. 9781.
30. Paganetti, H., *Proton Therapy Phyiscs*. 2012.
31. Parodi, K., et al., *Clinical CT-based calculations of dose and positron emitter distributions in proton therapy using the FLUKA Monte Carlo code.* Physics in medicine and biology, 2007. **52**(12): p. 3369-3387.
32. ICRU, *Report 44: Tissue Substitutes in Radiation Dosimetry and Measurement*, A. Alissy, et al., Editors. 1988: Maryland.
33. White, D.R., *Tissue substitutes in experimental radiation physics.* Med Phys, 1978. **5**(6): p. 467-79.
34. Mann-Krzisnik, D., F. Verhaegen, and S.A. Enger, *The influence of tissue composition uncertainty on dose distributions in brachytherapy.* Radiother Oncol, 2018. **126**(3): p. 394-410.
35. Pawlikowski, M., *Biomineralogical Studies of Oral Squamous Cell Carcinoma.* Archives of Community and Family Medicine, 2019. **2**(1): p. 19-33.
36. Maughan, R.L., et al., *The elemental composition of tumors: kerma data for neutrons.* Med Phys, 1997. **24**(8): p. 1241-4.
37. Horst, F., et al., *Measurement of PET isotope production cross sections for protons and carbon ions on carbon and oxygen targets for applications in particle therapy range verification.* Phys Med Biol, 2019. **64**(20): p. 205012.
38. Espana, S., et al., *The reliability of proton-nuclear interaction cross-section data to predict proton-induced PET images in proton therapy.* Phys Med Biol, 2011. **56**(9): p. 2687-98.
39. Conti, M. and L. Eriksson, *Physics of pure and non-pure positron emitters for PET: a review and a discussion.* EJNMMI Phys, 2016. **3**(1): p. 8.
40. Jodal, L., C. Le Loirec, and C. Champion, *Positron range in PET imaging: non-conventional isotopes.* Phys Med Biol, 2014. **59**(23): p. 7419-34.
41. Hoogenboom, B., *Radioisotope list Biograph*. 2019, Siemens Healthcare Nederland. p. 1.
42. Parodi, K., et al., *PET/CT imaging for treatment verification after proton therapy: a study with plastic phantoms and metallic implants.* Med Phys, 2007. **34**(2): p. 419-35.

43. Van Slambrouck, K., et al., *Bias reduction for low-statistics PET: maximum likelihood reconstruction with a modified Poisson distribution.* IEEE Trans Med Imaging, 2015. **34**(1): p. 126-36.
44. Cho, J., et al., *Determination of elemental tissue composition following proton treatment using positron emission tomography.* Phys Med Biol, 2013. **58**(11): p. 3815-35.
45. Grogg, K., et al., *Mapping (15)O production rate for proton therapy verification.* Int J Radiat Oncol Biol Phys, 2015. **92**(2): p. 453-9.
46. Nishio, T., et al., *Distributions of beta+ decayed nuclei generated in the CH2 and H2O targets by the target nuclear fragment reaction using therapeutic MONO and SOBP proton beam.* Med Phys, 2005. **32**(4): p. 1070-82.
47. Parodi, K., et al., *Patient study of in vivo verification of beam delivery and range, using positron emission tomography and computed tomography imaging after proton therapy.* Int J Radiat Oncol Biol Phys, 2007. **68**(3): p. 920-34.
48. Rui, E.M., et al., *Effect of Proton Irradiation on Mechanical Properties of Low-Density Polyethylene/Multiwalled Carbon Nanotubes Composites.* Polymer Composites, 2015. **36**(2): p. 278-286.
49. Sam, S.T., et al., *Recent Advances in Polyolefins/Natural Polymer Blends Used for Packaging Application.* Polymer-Plastics Technology and Engineering, 2014. **53**(6): p. 631-644.
50. Ali, U., K.J.B. Abd Karim, and N.A. Buang, *A Review of the Properties and Applications of Poly (Methyl Methacrylate) (PMMA).* Polymer Reviews, 2015. **55**(4): p. 678-705.
51. Choi, J. and J.O. Kang, *Basics of particle therapy II: relative biological effectiveness.* Radiat Oncol J, 2012. **30**(1): p. 1-13.
52. Farncombe, T. and K. Iniewski, *Medical Imaging: Technology and Applications*. 2017: CRC Press, Inc.
53. Magreñán, Á.A. and I.K. Argyros, *Chapter 5 - Gauss–Newton method*, in *A Contemporary Study of Iterative Methods*, Á.A. Magreñán and I.K. Argyros, Editors. 2018, Academic Press. p. 61-67.
54. Banks, H.T. and M.L. Loyner, *AIC under the framework of least squares estimation.* Appl. Math. Lett., 2017. **74**: p. 33-45.
55. Burnham, K.P. and D.R. Anderson, *Multimodel Inference.* Sociological Methods & Research, 2016. **33**(2): p. 261-304.
56. Cherry, S.R., J.A. Sorenson, and M.E. Phelps, *Physics in Nuclear Medicine*. 2012: Elsevier Saunders.
57. Bruyant, P.P., J. Sau, and J. Mallet, *Streak Artifact Reduction in Filtered Backprojection Using a Level Line–Based Interpolation Method.* Journal of Nuclear Medicine, 2000. **41**: p. 1913-1919.
58. Oen, S.K., et al., *Image quality and detectability in Siemens Biograph PET/MRI and PET/CT systems-a phantom study.* EJNMMI Phys, 2019. **6**(1): p. 16.
59. Rahmim, A., J. Qi, and V. Sossi, *Resolution modeling in PET imaging: theory, practice, benefits, and pitfalls.* Med Phys, 2013. **40**(6): p. 064301.
60. Chuong, M., et al., *Pencil beam scanning versus passively scattered proton therapy for unresectable pancreatic cancer.* J Gastrointest Oncol, 2018. **9**(4): p. 687-693.
61. Cambraia Lopes, P., et al., *First in situ TOF-PET study using digital photon counters for proton range verification.* Phys Med Biol, 2016. **61**(16): p. 6203-30.
62. Conti, M., et al., *Characterization of (176)Lu background in LSO-based PET scanners.* Phys Med Biol, 2017. **62**(9): p. 3700-3711.
63. Nishio, T. and A. Nishio-Miyatake, *Visualization of Dose Distributions for Proton*, in *Image-Based Computer-Assisted Radiation Therapy*. 2017. p. 319-354.

64. Glastonbury, C.M., E.E. Parker, and J.K. Hoang, *The postradiation neck: evaluating response to treatment and recognizing complications.* AJR Am J Roentgenol, 2010. **195**(2): p. W164-71.
65. McKeown, S.R., *Defining normoxia, physoxia and hypoxia in tumours-implications for treatment response.* Br J Radiol, 2014. **87**(1035): p. 1-12.
66. Vaupel, P., M. Hockel, and A. Mayer, *Detection and characterization of tumor hypoxia using pO2 histography.* Antioxid Redox Signal, 2007. **9**(8): p. 1221-35.
67. Barroso, E.M., et al., *Water Concentration Analysis by Raman Spectroscopy to Determine the Location of the Tumor Border in Oral Cancer Surgery.* Cancer Res, 2016. **76**(20): p. 5945-5953.
68. Colliez, F., B. Gallez, and B.F. Jordan, *Assessing Tumor Oxygenation for Predicting Outcome in Radiation Oncology: A Review of Studies Correlating Tumor Hypoxic Status and Outcome in the Preclinical and Clinical Settings.* Front Oncol, 2017. **7**: p. 10.
69. Peeters, S.G., et al., *A comparative study of the hypoxia PET tracers [(1)(8)F]HX4, [(1)(8)F]FAZA, and [(1)(8)F]FMISO in a preclinical tumor model.* Int J Radiat Oncol Biol Phys, 2015. **91**(2): p. 351-9.
70. Wiedenmann, N., et al., *Effect of radiochemotherapy on T2* MRI in HNSCC and its relation to FMISO PET derived hypoxia and FDG PET.* Radiat Oncol, 2018. **13**(1): p. 159.
71. Toramatsu, C., et al., *Washout effect in rabbit brain: in-beam PET measurements using 10C, 11C and 15O ion beams.* Biomedical Physics & Engineering Express, 2018. **4**(3).
72. Ammar, C., et al., *Comparing the biological washout of beta+-activity induced in mice brain after 12C-ion and proton irradiation.* Phys Med Biol, 2014. **59**(23): p. 7229-44.
73. van de Water, S., et al., *Shortening delivery times of intensity modulated proton therapy by reducing proton energy layers during treatment plan optimization.* Int J Radiat Oncol Biol Phys, 2015. **92**(2): p. 460-8.
74. Bourhis, J., et al., *Clinical translation of FLASH radiotherapy: Why and how?* Radiother Oncol, 2019. **139**: p. 11-17.
75. Lacas, B., et al., *Role of radiotherapy fractionation in head and neck cancers (MARCH): an updated meta-analysis.* The Lancet Oncology, 2017. **18**(9): p. 1221-1237.
76. Grewal, A.S., J. Jones, and A. Lin, *Palliative Radiation Therapy for Head and Neck Cancers.* Int J Radiat Oncol Biol Phys, 2019. **105**(2): p. 254-266.
77. Nantavithya, C., et al., *Phase 2 Study of Stereotactic Body Radiation Therapy and Stereotactic Body Proton Therapy for High-Risk, Medically Inoperable, Early-Stage Non-Small Cell Lung Cancer.* International Journal of Radiation Oncology*Biology*Physics, 2018. **101**(3): p. 558-563.
78. Sio, T.T., et al., *Spot-scanned pancreatic stereotactic body proton therapy: A dosimetric feasibility and robustness study.* Phys Med, 2016. **32**(2): p. 331-42.
79. van Marlen, P., et al., *Bringing FLASH to the Clinic: Treatment Planning Considerations for Ultrahigh Dose-Rate Proton Beams.* Int J Radiat Oncol Biol Phys, 2020. **106**(3): p. 621-629.
80. van de Water, S., et al., *Towards FLASH proton therapy: the impact of treatment planning and machine characteristics on achievable dose rates.* Acta Oncol, 2019. **58**(10): p. 1463-1469.
81. Hayya, J., D. Armstrong, and N. Gressis, *A Note on the Ratio of Two Normally Distributed Variables.* Management Science, 1975. **21**(11): p. 1338-1341.

DANKWOORD

Afgelopen jaar is een ontzettend leerzame en inspirerend periode voor mij geweest. Ik had het geluk kennis en ervaring te mogen verkrijgen vanuit drie vooraanstaande instituten en ik ben ontzettend dankbaar voor alle mensen die dit hebben mogelijk gemaakt.

In het LUMC heb ik vanaf moment één een ontzettend fijne werksfeer ervaren. Dennis, Lioe-Fee, Floris, jullie waren de beste begeleiders die ik mij kon wensen. Jullie onuitputtelijke positiviteit en ambitie hebben mij meer dan ooit gemotiveerd het beste uit mezelf te halen. Dennis, jouw passie en energie voor het vak zijn ontzettend aanstekelijk. Dankjewel voor het delen van je visie en voor de tijd die je hebt genomen om mij in het onderwerp te introduceren en waar nodig samen naar de data te kijken. Floris, dankjewel dat ik altijd bij je binnen kon lopen voor een (initieel) korte vraag, waarbij jouw wetenschappelijke visie en ervaring telkens weer ontzettend waardevol bleken. Lioe-Fee, jouw positieve visie, betrokkenheid en vele connecties vind ik bewonderenswaardig!

Daarnaast is mijn tijd in het LUMC ook gekenmerkt door de cornerboys, research gruppa en vsco girls. Wat heb ik met jullie gelachen. Geweldig hoe collega's zo'n fijne werksfeer kunnen geven. Ik vind het jammer dat ik niet overal bij heb kunnen zijn.

Vanuit de Universiteit Twente wil ik graag Prof. Slump bedanken. Jij hebt me geleerd data te voorspellen en te interpreteren. Ik vind het heel bijzonder hoe jij, ondanks de technische diepgang, altijd de klinische relevantie weet in te zien. Paul, door jou procesbegeleiding in de afgelopen twee stagejaren heb ik ontzettend veel geleerd over mijzelf. Ik voelde me altijd begrepen en serieus genomen. Dankjewel daarvoor. Daarnaast vind ik het mooi hoe jij heel goed voor ogen hebt welke competenties een Technisch Geneeskundige moet bezitten.
Tim Boers, fijn dat jij als extern lid wilt bijdragen aan deze thesis.

Ik ben ook ontzettend dankbaar dat ik de kans kreeg in het HollandPTC mijn weg te vinden. Ik vind het ontzettend gaaf om te zien hoe dit poliklinische centrum voor protonentherapie sinds anderhalf jaar draaiende is. Iedereen zet zijn schouders onder de patiëntenzorg en de uitvoering van wetenschappelijk onderzoek. Dankjewel Pieternel in het bijzonder voor het meedenken over mijn onderzoek en het praktisch uitvoerbaar maken van mijn experimenten. Ik waardeer het dat jij, zelfs na je afscheid bij het HollandPTC, nog plaats wilde nemen in mijn afstudeercommissie. Franciska, zonder jou was dat fantoom nooit bestraald geweest, dankjewel!

Charlotte, Charlotte and Marta, thank you for introducing me in the HollandPTC. You made me feel comfortable in the research office. Charlotte van der Vos, thank you for your support during my internship with your experience as a Technical Physician.
Petra Trnkova and Marta Rovituso, thank you for making time for me to think along in the experimental setup and in the creation of a feasible treatment plan.

Alle artsen, MBB'ers, klinisch fysici en KFM'ers, die dagelijks zo hard werken om de patiënten de beste diagnostiek en therapie te kunnen bieden. Jullie zijn goud! Dankjulliewel dat jullie mij de basis binnen de nucleaire geneeskunde en de radiotherapie hebben laten leggen. Specifiek wil ik de MBB'ers van de nucleaire geneeskunde bedanken. Jullie hebben mij laten inzien dat niet alles altijd verloopt zoals in de boeken. Daarnaast, Stefan Hutschemaekers en Martin de Jong, dankjulliewel voor het meedenken en faciliteren van de mogelijkheden binnen mijn klinische ontwikkeling.

Lieve vrienden, zonder jullie heeft het leven geen zin. We gaan de aankomende tijd oneindig veel videobellen. Lieve familie, jullie hebben mij geleerd wat hard werken is. Allerliefste Roos, jij bent zo sterk! Zonnige tijden komen eraan. Jan Jakob, Dankjewel voor alle intelligentie die je met mij deelt en alle vrijheid en ondersteuning die je mij biedt. Jij bent er voor me, en dat vind ik heel bijzonder.

Hanneke – 5 april 2020

APPENDIX A

Verantwoording

Volledige verantwoording op aanvraag

Deze verantwoording is mijn laatste reflectie wat betreft mijn ontwikkeling tot afgestudeerd Technisch Geneeskundige. Ik heb mij ontwikkeld binnen het domein van de *beroepsbeoefenaar* door alle hierboven beschreven theoretische kennis en praktische vaardigheden, op zowel onderzoek als klinisch gebied. Ik heb laten zien in staat te zijn binnen korte tijd de hoofdlijnen van beide betrokken disciplines, de nucleaire geneeskunde en de radiotherapie te doorgronden. Op *organisatorisch* vlak ben ik sterk verbeterd in het proactief organiseren van mijn experimenten en onderzoek en in het nastreven van mijn wensen en leerdoelen op klinisch gebied. Binnen de competentie *samenwerker* heb ik geleerd veel kennis en ervaring op te doen bij de specialisten en deze waar nodig bij elkaar te brengen voor het kortsluiten van belangrijke beslissingen. In het samenbrengen van mensen en het overdragen van kennis aan collega's en patiënten is *communicatie* erg belangrijk. Een domein waarin ontwikkeling ook nooit zal stoppen. Daarnaast heb ik mij gedurende deze twee jaar ontzettend verbeterd in mijn *academische vaardigheden*, van het opzetten van experimenten, het stellen van hypotheses, maar ook de uitgebreide toetsing van deze hypotheses met de resultaten uit de experimenten en resultaten uit de literatuur.

Samengevat kan ik stellen dat ik ontzettend veel geleerd heb in mijn ontwikkeling naar Technisch Geneeskundige, waarvan dit verslag een korte samenvatting is. Ik ben me er van bewust dat ik mij mijn hele leven zal ontwikkelen in de omschreven en in nieuwe leerdoelen, maar ik kan stellen dat ik de handvatten heb om dit actief te doen.

Ik zal hier mee van start gaan binnen mijn aankomende PhD in het VUmc waarin ik PET-imaging ga inzetten ten behoeve van immunotherapie tracer ontwikkeling. Ik ben er klaar voor!

APPENDIX B

Use of [18F]FDG PET/CT for Target Volume Definition in Radiotherapy

Full version can be found in the book "Image-Guided High-Precision Radiotherapy 'Springer Nature 2020

Abstract

Addition of spatial biological information, provided by 2-[^{18}F]fluoro-2-deoxy-D-glucose positron emission tomography/computed tomography ([^{18}F]FDG PET/CT) imaging is recommended for target volume delineation in head-and-neck, lung, gynaecological, oesophageal cancer and lymphoma. Standardised patient preparation and acquisition and reconstruction of the PET-images are mandatory. Patient positioning and alignment should be performed using lasers and immobilising devices, and images are preferable acquired in radiotherapy position. Correction for respiratory motion should be considered and performed by motion-encompassing, controlled breathing, respiratory gating or data driven gating. These motion-corrections should match the mitigation methods used for radiotherapy planning and treatment delivery. The success of PET-guided target volume delineation depends mainly on the performed segmentation technique, in which we distinguish manual, semi-automatic or automatic segmentation methods. Manual segmentation has the largest interobserver variability and automatic segmentation can be optimised by consensus algorithms. Despite promising results of automatic segmentation methods, none are currently applicable in all clinical settings. Therefore, results should always be verified by an expert. Despite feasibility and advantages observed in planning studies, the clinical level of evidence for [^{18}F]FDG PET/CT-guided treatment planning is still limited.

Keywords:
[^{18}F]FDG PET/CT, target volume delineation, GTV, treatment planning, patient alignment, motion correction, automatic segmentation, head-and-neck cancer, lung cancer, lymphoma.